INVESTIGATING LOOP CURRENT DEEP DYNAMICS AND SEPARATION EVENTS FROM A COUPLED OCEAN-ATMOSPHERE REGIONAL MODEL AND IN-SITU OBSERVATIONS

A Dissertation

by

XIAO GE

Submitted to the Graduate and Professional School of
Texas A&M University
in partial fulfillment of the requirements for the degree of

DOCTOR OF PHILOSOPHY

Chair of Committee,	Steven F. DiMarco
Committee Members,	Ping Chang
	Henry Potter
	Courtney Schumacher
Head of Department,	Shari Yvon-Lewis

December 2022

Major Subject: Oceanography

ABSTRACT

A 9-year nature run (free run) and two assimilative runs of R-CESM are used to reveal the mechanisms of Loop Current (LC) deep dynamics. The numerical outputs are compared to the in-situ observations. Our results indicate the R-CESM has the capability to capture the major features of Loop Current Eddies (LCEs) shedding events in both upper and lower layers, the thermal structure is biased (warmer upper layer, cooler lower layer) as most previous modeling studies. The assimilation of sea surface height (SSH) improves the simulation of upper-layer Loop Current System (LCS) dynamics, and the assimilation of sea surface temperature (SST) revises the bias induced by the assimilation of SSH. The Self-organizing Map (SOM) analysis of SSH and stream function at 27.5 kg/m^3 potential density layer under the LCS indicates the different stages of the LCEs shedding events in the upper and lower layers. The circulation features under the LCS display the precursor patterns of the LCEs shedding events identified by the SOM. The Principal Component Analysis (PCA) is applied to combine different variables from different locations as one metric via weighted parameters from the critical regions of the precursor patterns at the bottom of the LCS. The leading variables are the 8-16 days scale-averaged variance of kinetic energy as derived from wavelet transform. These 8-16 days variations, identified as the Mixed Rossby-Gravity (MRG) waves in this dissertation, are stimulated by the interaction between the penetrating LC and sharp topography. There are three critical regions for the propagating wave trains: the Mississippi Fan, the Yucatan Shelf, and the Florida Escapement. The wave trains determine five different scenarios: the East Yucatan Shelf Scenario (EYSS), the West Yucatan Shelf Scenario (WYSS), the West Florida Escarpment Scenario (WFES), the Mississippi Fan Scenario (MFS), and the Quiescent Scenario (QS). A west necking-down region associated with the LCEs separations is found below the LCS around 88.5 °W. The wave train scenarios passing through the west necking-down region from the Mississippi Fan and Yucatan Shelf are used to indicate the LCEs separations. The description of the lower-layer structure can improve the understanding of the LCS dynamics.

ACKNOWLEDGMENTS

I would like to acknowledge Professor Steven F. DiMarco for invaluable guidance and philosophy in all aspects. I would like to thank the members of my committee, Professor Ping Chang (TAMU), Professor Henry Potter (TAMU), and Professor Courtney Schumacher (TAMU), for being supportive of my work and for many valuable suggestions. I would like to thank Professor Qinyu Liu (OUC) for advising me to grab the opportunity to have this enjoyable graduate school experience at Texas A&M University. I would thank Dr. Yun Liu for supporting me with data sets and giving me critical ideas. I would also like to thank my colleagues and friends, Dr. Dan Fu, Dr. Xue Liu, Dr. Lixin Qu, Dr. Gaopeng Xu, Dr. Qiuying Zhang, Dr. Sakib Mahmud, Dr. Meng Lyu, and Xin Yang for their help and support.

CONTRIBUTORS AND FUNDING SOURCES

Contributors

This work was guided by a dissertation committee consisting of Professors Steven F. DiMarco (advisor), Ping Chang, and Henry Potter the Department of Oceanography, and Professor Courtney Schumacher of the Department of Atmospheric Sciences.

The numerical simulation outputs analyzed for sections 3 and 4 was provided by Dr. Yun Liu from iHesp (available at https://ihesp.github.io/archive/). The in-situ observations data analyzed for sections 3 and 4 was the Loop Current Dynamics Experiments 2009-2011 sponsored by the Environmental Studies Program of the US Department of the Interior's Bureau of Ocean Energy Management (BOEM) and led by Dr. Alexis Lugo-Fernández (available at https://data.gov/).

All other work conducted for the dissertation was completed by the student independently.

Funding Sources

Graduate study was supported by a scholarship from China Scholarship Council, and Department of Oceanography, Texas A&M University.

NOMENCLATURE

A/L	Atmosphere-land
A/O	Atmosphere-ocean
ADCP	Acoustic Doppler Current Profiler
AMSR-E	Advanced Microwave Scanning Radiometer on the Earth Observing System
AVHRR	Advanced Very High Resolution Radiometer
BMU	Best Matching Unit
C3S	Copernicus Climate Change Service
CESM	Community Earth System Model
CICESE	Centro de Investigación Científica y de Educación Superior de Ensenada
CIME	Common Infrastructure for Modeling the Earth
CL	Confidence Level
CLM	Community Land Model
DoF	Degree of Freedom
DUACS	Data Unification and Altimeter Combination System
EDoF	Effective Degrees of Freedom
EKE	Eddy Kinetic Energy
EOF	Empirical Orthogonal Function
EYSS	East Yucatan Shelf Scenario
FFT	Fast Fourier Transform
GCW	Gulf Common Water
GEM	Gravest Empirical Mode

GHRSST	Group for High Resolution Sea Surface Temperature
GoM	Gulf of Mexico
LC	Loop Current
LCE	Loop Current Eddy
LCS	Loop Current System
mab	meter above the bottom
MEaSUREs	Making Earth System Data Records for Use in Research Environment
MFS	Mississippi Fan Scenario
MRG	Mixed Rossby-Gravity
NCAR	National Center for Atmospheric Research
NOAA	National Oceanic and Atmospheric Administration
OI	Optimum Interpolation
OISST	Optimum Interpolation Sea Surface Temperature
PC	Principal Component
PCA	Principal Component Analysis
PIES	Pressure Inverted Echo Sounder
PV	Potential Vorticity
PSD	Power Spectral Density
QS	Quiescent Scenario
R-CESM	Regional Community Earth System Model
ROMS	Regional Ocean Modeling System
SAIC	Science Applications International Corporation
SLA	Sea Level Anomaly
SLAT	Sea Level Anomaly and Temperature
SOM	Self-organizing Map

SSH	Sea Surface Height
SSHT	Sea Surface Height and Temperature
SSHA	Sea Surface Height Anomaly
SST	Sea Surface Temperature
SUW	Caribbean Subtropical Underwater
SVD	Singular Value Decomposition
TAMU	Texas A&M University
TS	Temperature-salinity
TRW	Topographic Rossby Wave
WFES	West Florida Escarpment Scenario
WRF	Weather Research and Forecasting Model
WYSS	West Yucatan Slope Scenario

TABLE OF CONTENTS

Page

ABSTRACT ii

ACKNOWLEDGMENTS iii

CONTRIBUTORS AND FUNDING SOURCES iv

NOMENCLATURE v

TABLE OF CONTENTS viii

LIST OF FIGURES x

LIST OF TABLES xxiii

1. INTRODUCTION 1

    1.1 Motivation 1
    1.2 Background 1
        1.2.1 Gulf of Mexico Circulation System 1
        1.2.2 Loop Current Dynamics 3
    1.3 Hypotheses 5
    1.4 Objectives 6
        1.4.1 Organization 8

2. DATA AND METHODS 9

    2.1 Loop Current Dynamics Experiment 2009-2011 9
    2.2 Regional Community Earth System Model 10
        2.2.1 Free Run (Nature/NA) Description 12
        2.2.2 Assimilative Runs Description: SLAT and SLA 12
    2.3 Metric Definitions 15
        2.3.1 Lanczos Cosine Filter 16
        2.3.2 Vertical Structure 16
        2.3.3 Vector Correlation 19
        2.3.4 Stream Function 20
        2.3.5 Potential Vorticity 21
    2.4 Characteristics Analysis 21
        2.4.1 Empirical Orthogonal Function/Principal Component Analysis 21
        2.4.2 Self-organizing Map 22
        2.4.3 Variance-preserving Spectra 24

3. LOOP CURRENT SYSTEM IN NUMERICAL SIMULATIONS 25

3.1 Validation of the Free-run Simulation 25
3.2 Loop Current Evolution 36
3.2.1 Sea Surface Height Evolution 37
3.2.2 SLAT Simulation 41
3.2.3 SLA Simulation 44
3.2.4 Surface SOM Analysis 47
3.2.5 Deep Stream Function Evolution 47
3.2.6 Characteristics of Stream Function at Different Depths 53
3.3 Discussion 61

4. LOOP CURRENT INDICATOR METRIC 65

4.1 Improvements from Data Assimilation 65
4.1.1 Dynamical Structure 65
4.1.2 Thermal Structure 70
4.2 Wavelet Analysis 74
4.2.1 Observations 76
4.2.2 Numerical Simulations 80
4.3 Multi-variables Analysis 86
4.3.1 NA Simulation 86
4.3.2 SLAT Simulation 90
4.4 Indicator Metric 93
4.5 Mixed Rossby-Gravity Wave 95
4.5.1 Two Groups of Shedding Cases 96
4.5.2 Five Scenarios of MRG Waves 106
4.5.3 West Necking-down Region 114
4.6 Discussion 118

5. CONCLUSIONS AND FUTURE WORK 121

5.1 Conclusions 121
5.2 Future Work 123

REFERENCES 124

APPENDIX A. MOORING DETAILS OF LOOP CURRENT DYNAMICS EXPERIMENTS 2009-2011 133

LIST OF FIGURES

FIGURE Page

1.1 The circulation features of the upper layer (surface to ~1000 m), and lower layer (~1000 m to the seafloor) in the GoM. Modified from Furey et al. (2018). 2

2.1 The locations of the LC moorings (top panel), and the data acquisition intervals (bottom panel). Modified from Hamilton et al. (2015). 10

2.2 The schematic of the R-CESM component models and structure of surface flux calculation (left panel), and the R-CESM model domains for the GoM (right panel). Modified from Fu et al. (2021)..... 11

2.3 Processing flow chart of the R-CESM simulations in this research. The detailed methods are described in Sections 2.3 and 2.4, and related objectives are listed below the corresponding methods. 15

2.4 Time-averaged zonal z coordinate section of meridional velocity along 25 °N in NA (top panel), SLAT (middle panel) and SLA (bottom panel) simulations. The blue contours indicate the depths of the 9 selected potential density layers, the red contours are the isotherms, and the background colors are the meridional velocity. .. 18

3.1 The top panel shows the mean spatial distributions of SSH (colors) and velocity (vectors) in the second bottom layer of R-CESM. The depth of the second bottom layer in the 3200 m region is approximately 200 m above the bottom. The contours with yellow numbers show the depth of the second bottom layer in different regions. The thick blue contour indicates the 17 cm SSH, which is the mean location of the LC during the whole period. The thick orange contour marks out the region that has the highest standard deviation of SSH, which is the selected region for the SSHA index in the bottom panel. The bottom panel shows the regional averaged SSHA from the Making Earth System Data Records for Use in Research Environments (MEaSUREs) data (blue line) and R-CESM data (red line). The regions are selected by their corresponding standard deviations of SSHA (larger than 0.2 m for MEaSUREs, larger than 0.25 m for R-CESM). The orthogonal pink lines indicate the along-LC section and across-LC section in Figure 3.2. 26

3.2 The sections along the LC (top panel) and across the LC (bottom panel). The colors show the velocity across the sections (red is northward/eastward, blue is southward/westward). The orange contour shows the depth of the 6°C isotherm along the section, which indicates the depth of the thermocline and the bottom of the LC. The black contours present some isotherms in the unit of [°C]. 27

3.3 The histogram of the spatial averaged velocities at the locations of the SAIC moorings from SAIC observations (top panel) and R-CESM free-run outputs(bottom panel). Different colors indicate different depths. 28

3.4 The temperature-depth profile (left panel) and temperature-salinity (TS) profile (right panel) of free-run simulation interpolated at all the SAIC mooring locations. Each color represents a unique mooring station. 29

3.5 The temperature profile (left panel) and salinity profile (right panel) of all the SAIC moorings. The red color (bottom x-axis) presents the temperature or salinity data, and the blue color (top x-axis) presents the corresponding error defined as the temporally averaged standard deviation of every 12-hour interval. 30

3.6 The top panel is the time-averaged potential temperature profile (x-axis is the temperature, the right y-axis is the depth) at station A2 of observation (blue) and interpolated free-run simulation (orange). The top panel also presents the regression relationship between potential temperature from observation and interpolated free-run simulation at all depths and times (green). The red line is the 45° line to be compared with the yellow regression line. The bottom panel shows the histogram of the same temperature data as the top panel from observation (blue) and simulation (orange). 31

3.7 The top panel is the time-averaged potential temperature profile (x-axis is the temperature, the right y-axis is the depth) at station C2 of observation (blue) and interpolated free-run simulation (orange). The top panel also presents the regression relationship between potential temperature from observation and interpolated free-run simulation at all depths and times (green). The red line is the 45° line to be compared with the yellow regression line. The bottom panel shows the histogram of the same temperature data as the top panel from observation (blue) and simulation (orange). 32

3.8 The top panel is the time-averaged potential temperature profile (x-axis is the temperature, the right y-axis is the depth) at station N4 of observation (blue) and interpolated free-run simulation (orange). The top panel also presents the regression relationship between potential temperature from observation and interpolated free-run simulation at all depths and times (green). The red line is the 45° line to be compared with the yellow regression line. The bottom panel shows the histogram of the same temperature data as the top panel from observation (blue) and simulation (orange). 33

3.9 The top panel is the time-averaged potential temperature profile (x-axis is the temperature, the right y-axis is the depth) at station Y6 of observation (blue) and interpolated free-run simulation (orange). The top panel also presents the regression relationship between potential temperature from observation and interpolated free-run simulation at all depths and times (green). The red line is the 45° line to be compared with the yellow regression line. The bottom panel shows the histogram of the same temperature data as the top panel from observation (blue) and simulation (orange). 34

3.10 The top panel is the power spectra of velocity at multiple depths of CICEIE mooring station N4, and the bottom panel is the power spectra of velocity at interpolated depths of free-run R-CESM data at the same spatial spots. The depths are shown by the color bar, the vertical scatter plot presents the sampling distribution. 35

3.11 The spatial distributions of stream function in the second bottom (σ) layer of R-CESM on December 15th, 2018. The depth of the second bottom layer in the 3200 m region is approximately 200 m above the bottom. The orange vectors are velocity fields associated with the stream function. The thick red contour indicates the 17 cm SSH, which is the location of the LC on December 15th, 2018. 36

3.12 The sorted SSH regions are shown based on the spatially trained SOM of the free-run simulation. The shading color indicates different areas distinguished by the SSH time series at that grid point. The blue contour is the time-averaged 17 cm SSH line presenting the mean location of the LC. 38

3.13 The sixteen panels present the SOM-captured primary spatial patterns of the SSH in the free-run simulation. The frequency of occurrence is shown as the subtitles of each pattern. The shading color indicates the SSH reconstructed from the SOM weighted vectors. The blue contour is the time-averaged 17 cm SSH line presenting the mean location of the LC, which is same in each panel. 39

3.14 The colored dots show the grouped BMU of the SSH in the free-run simulation. The shading areas indicate all the LCEs shedding events from their first separation to their final separation, and the vertical blue lines present the reattachment occurring during each LCEs shedding event. The red line is the normalized SSHA index from the orange region in Figure 3.1, and the blue line shows the normalized accumulating SSHA index from the same region that has the maximum SSH standard deviation. 40

3.15 The colored dots show the grouped BMU of the SSH in the SLAT simulation. The shading areas indicate all the LCEs shedding events from their first separation to their final separation, and the vertical blue lines present the reattachment occurring during each LCEs shedding event. The red line is the normalized SSHA index from the orange region in Figure 3.1, and the blue line shows the normalized accumulating SSHA index from the same region that has the maximum SSH standard deviation. 41

3.16 Four panels present the four LCEs shedding events in the SLAT simulation, the colors is the time averaged SSH from the first separation to the final separation, the blue contours show the 17 cm SSH at the date of first separation, and the green contours indicate the 17 cm SSH at the date of final separation 42

3.17 The colored dots show the grouped BMU of the SSH in the SLA simulation. The shading areas indicate all the LCEs shedding events from their first separation to their final separation, and the vertical blue lines present the reattachment occurring during each LCEs shedding event. The red line is the normalized SSHA index from the orange region in Figure 3.1, and the blue line shows the normalized accumulating SSHA index from the same region that has the maximum SSH standard deviation. 44

3.18 Four panels present the four LCEs shedding events in the SLA simulation, the colors is the time averaged SSH from the first separation to the final separation, the blue contours show the 17 cm SSH at the date of first separation, and the green contours indicate the 17 cm SSH at the date of final separation 46

3.19 The sixteen panels present the SOM-captured primary spatial patterns of the stream function in the free-run simulation. The frequency of occurrence is shown as the subtitles of each pattern. The shading color indicates the stream function reconstructed from the SOM weighted vectors. The blue contour is the time-averaged 17 cm stream function line presenting the mean location of the LC. 48

3.20 The colored dots show the grouped BMU of the stream function in the free-run simulation. The shading areas indicate all the LCEs shedding events from their first separation to their final separation, and the vertical blue lines present the reattachment occurring during each LCEs shedding event. The red line is the normalized SSHA index from the orange region in Figure 3.1, and the blue line shows the normalized accumulating SSHA index from the same region that has the maximum SSH standard deviation. 50

3.21 The colored dots show the grouped BMU of the stream function in the SLAT simulation. The shading areas indicate all the LCEs shedding events from their first separation to their final separation, and the vertical blue lines present the reattachment occurring during each LCEs shedding event. The red line is the normalized SSHA index from the orange region in Figure 3.1, and the blue line shows the normalized accumulating SSHA index from the same region that has the maximum SSH standard deviation. 51

3.22 The colored dots show the grouped BMU of the stream function in the SLA simulation. The shading areas indicate all the LCEs shedding events from their first separation to their final separation, and the vertical blue lines present the reattachment occurring during each LCEs shedding event. The red line is the normalized SSHA index from the orange region in Figure 3.1, and the blue line shows the normalized accumulating SSHA index from the same region that has the maximum SSH standard deviation. 52

3.23 The contributions of the first five modes of EOF results at selected depths in SLAT (top panel) and SLA (bottom panel) simulations. The different colors present different depths, the four selected depths are 300 m (blue), 1000 m (orange), 1500 m (green), and 3000 m (red). 55

3.24 The four panels present four modes from four EOF analysis results of SLAT simulation at different depths shown in each title. These modes have the highest correlation coefficient between their PC time series and the SSHA index, their contributions are also shown in each title. For each panel, the top figures show the spatial pattern of the normalized stream function of each selected mode, the bottom figure presents the corresponding time series (blue line) and the SSHA index (red line). In the top figures, the blue contour is the time-averaged 17 cm SSH line indicating the mean location of the LC. The orange contour in the top figures circles the SSH large standard deviation region (> 27 cm), the averaged SSHA in this region is used as the SSHA index. The shading area in the bottom figures indicate all the LCEs shedding events from their first separation to their final separation, and the vertical blue lines present the reattachment occurring during each LCEs shedding event. The bottom labels show the correlation coefficients, EDoF, and corresponding 95% confidence level for each selected mode. 57

3.25 The four panels present four modes from four EOF analysis results of SLA simulation at different depths shown in each title. These modes have the highest correlation coefficient between their PC time series and the SSHA index, their contributions are also shown in each title. For each panel, the top figures show the spatial pattern of the normalized stream function of each selected mode, the bottom figure presents the corresponding time series (blue line) and the SSHA index (red line). In the top figures, the blue contour is the time-averaged 17 cm SSH line indicating the mean location of the LC. The orange contour in the top figures circles the SSH large standard deviation region (> 27 cm), the averaged SSHA in this region is used as the SSHA index. The shading area in the bottom figures indicate all the LCEs shedding events from their first separation to their final separation, and the vertical blue lines present the reattachment occurring during each LCEs shedding event. The bottom labels show the correlation coefficients, EDoF, and corresponding 95% confidence level for each selected mode. 59

3.26 The three panels are the σ-layer velocity anomaly profiles across station N4 of the SLAT simulation at noon on September 21st, 2010. The top panel is the meridional section, the middle panel is the zonal section, and the bottom panel is the cross-shore section. The green vertical line indicates the location of station N4, the red color is the positive velocity (eastward, northward, and northwestward), and the blue color is the negative velocity (westward, southward, and southeastward). 62

3.27 The three panels are the σ-layer velocity anomaly profiles across station N4 of the SLA simulation at noon on September 21st, 2010. The top panel is the meridional section, the middle panel is the zonal section, and the bottom panel is the cross-shore section. The green vertical line indicates the location of station N4, the red color is the positive velocity (eastward, northward, and northwestward), and the blue color is the negative velocity (westward, southward, and southeastward). 63

4.1 The three panels are the vector correlation coefficient r_{vc}^2 at all current meter locations for free-run simulation (left panel), SLAT simulation (middle panel), and SLA simulation (right panel). The green dots indicate the r_{vc}^2 (x-axis) of each sensor at different depths (y-axis). The red error bar is the corresponding error for each r_{vc}^2. The blue line is the fitted function of r_{vc}^2 varying on depth, and the purple shading is the corresponding error range. 66

4.2 The speed histogram (top panel), u velocity histogram (middle panel), and v velocity histogram (bottom panel) at 900 m depth of SAIC stations A2 (top three panels) and C2 (bottom three panels). The station information is in the subtitles. Each color represents a different dataset, blue is the mooring observation, orange is the NA simulation, green is the SLAT simulation, and red is the SLA simulation. . 67

4.3 The speed histogram (top panel), u velocity histogram (middle panel), and v velocity histogram (bottom panel) at 901 m and 848 m depth of CICESE stations N4 (top three panels) and Y6 (bottom three panels). The station information is in the subtitles. Each color represents a different dataset, blue is the mooring observation, orange is the NA simulation, green is the SLAT simulation, and red is the SLA simulation. 69

4.4 The temperature-depth profile (left panel) and temperature-salinity (TS) profile (right panel) of SLAT simulation interpolated at all the SAIC mooring locations. Each color represents a mooring station. 70

4.5 The temperature-depth profile (left panel) and temperature-salinity (TS) profile (right panel) of SLA simulation interpolated at all the SAIC mooring locations. Each color represents a mooring station. 71

4.6 The salinity histogram (top panel) and temperature histogram (bottom panel) above 1000 m of PIES stations 52 (top two panels) and 62 (bottom two panels). The station information is in the subtitles. Each color represents a different dataset, blue is the mooring observation, orange is the NA simulation, green is the SLAT simulation, and red is the SLA simulation. 72

4.7 The salinity histogram (top panel) and temperature histogram (bottom panel) above 1000 m of PIES stations 65 (top two panels) and 75 (bottom two panels). The station information is in the subtitles. Each color represents a different dataset, blue is the mooring observation, orange is the NA simulation, green is the SLAT simulation, and red is the SLA simulation. 73

4.8 The time averaged steam function at the 27.5 kg/m^3 σ_θ layer in the NA simulation, the five boxes indicate the five regional averaged regions, the black lines present the three sections in Figure 4.9. 74

4.9 The depth of 27.5 kg/m^3 σ_θ layer in the SLAT simulation, the left panel is the north zonal section in Figure 4.8, the middle panel is the south section in Figure 4.8, and the right panel is the meridional section along the LC in Figure 4.8..... 75

4.10 The wavelet analysis of $u + v$ at 900 m depth at station B1 in the period of days. The top panel shows the original input time series, the right panel in the middle is the wavelet transform, the left panel in the middle present the time-averaged power at different period, and the bottom panel is the temporal evolution of 8-16 days scale-averaged variance. The shadow region in the wavelet transform indicates the values below the 95% significant level. The dashed line in the bottom and right middle panels is the 95% significant level. The gray line in the right middle panel is the power via the fast Fourier transform. 77

4.11 The wavelet analysis of $u + v$ at 900 m depth at station C1 in the period of days. The top panel shows the original input time series, the right panel in the middle is the wavelet transform, the left panel in the middle present the time-averaged power at different period, and the bottom panel is the temporal evolution of 8-16 days scale-averaged variance. The shadow region in the wavelet transform indicates the values below the 95% significant level. The dashed line in the bottom and right middle panels is the 95% significant level. The gray line in the right middle panel is the power via the fast Fourier transform. 78

4.12 The wavelet analysis of $u + v$ at 901 m depth at station N4 in the period of days. The top panel shows the original input time series, the right panel in the middle is the wavelet transform, the left panel in the middle present the time-averaged power at different period, and the bottom panel is the temporal evolution of 8-16 days scale-averaged variance. The shadow region in the wavelet transform indicates the values below the 95% significant level. The dashed line in the bottom and right middle panels is the 95% significant level. The gray line in the right middle panel is the power via the fast Fourier transform. 79

4.13 The wavelet analysis of regional averaged $u + v$ at 27.5 kg/m^3 σ_θ layer of region 1 in the period of days. The left part is the free-run simulation, and the right part is the SLAT simulation. The top panel shows the original input time series, the right panel in the middle is the wavelet transform, the left panel in the middle present the time-averaged power at different period, and the bottom panel is the temporal evolution of 8-16 days scale-averaged variance. The shadow region in the wavelet transform indicates the values below the 95% significant level. The dashed line in the bottom and right middle panels is the 95% significant level. The gray line in the right middle panel is the power via the fast Fourier transform. 80

4.14 The wavelet analysis of regional averaged $u + v$ at 27.5 kg/m^3 σ_θ layer of region 2 in the period of days. The left part is the free-run simulation, and the right part is the SLAT simulation. The top panel shows the original input time series, the right panel in the middle is the wavelet transform, the left panel in the middle present the time-averaged power at different period, and the bottom panel is the temporal evolution of 8-16 days scale-averaged variance. The shadow region in the wavelet transform indicates the values below the 95% significant level. The dashed line in the bottom and right middle panels is the 95% significant level. The gray line in the right middle panel is the power via the fast Fourier transform. 81

4.15 The wavelet analysis of regional averaged $u + v$ at 27.5 kg/m^3 σ_θ layer of region 3 in the period of days. The left part is the free-run simulation, and the right part is the SLAT simulation. The top panel shows the original input time series, the right panel in the middle is the wavelet transform, the left panel in the middle present the time-averaged power at different period, and the bottom panel is the temporal evolution of 8-16 days scale-averaged variance. The shadow region in the wavelet transform indicates the values below the 95% significant level. The dashed line in the bottom and right middle panels is the 95% significant level. The gray line in the right middle panel is the power via the fast Fourier transform. 82

4.16 The wavelet analysis of regional averaged $u + v$ at 27.5 kg/m^3 σ_θ layer of region 4 in the period of days. The left part is the free-run simulation, and the right part is the SLAT simulation. The top panel shows the original input time series, the right panel in the middle is the wavelet transform, the left panel in the middle present the time-averaged power at different period, and the bottom panel is the temporal evolution of 8-16 days scale-averaged variance. The shadow region in the wavelet transform indicates the values below the 95% significant level. The dashed line in the bottom and right middle panels is the 95% significant level. The gray line in the right middle panel is the power via the fast Fourier transform. 83

4.17 The wavelet analysis of regional averaged $u + v$ at 27.5 kg/m^3 σ_θ layer of region 5 in the period of days. The left part is the free-run simulation, and the right part is the SLAT simulation. The top panel shows the original input time series, the right panel in the middle is the wavelet transform, the left panel in the middle present the time-averaged power at different period, and the bottom panel is the temporal evolution of 8-16 days scale-averaged variance. The shadow region in the wavelet transform indicates the values below the 95% significant level. The dashed line in the bottom and right middle panels is the 95% significant level. The gray line in the right middle panel is the power via the fast Fourier transform. 84

4.18 Two snapshots of the 8-16 days scale-averaged variance of $u + v$ distribution in the NA simulation, the time is on the title of each panel. In the upper panels, the streamline indicates the 8-16 band-pass filtered u and v velocity, the colors present the amplitude of the 8-16 days scale-averaged variance of $u + v$, and the blue contour is the simultaneous 17 cm SSH on the surface. The lower panels present the regional averaged 8-16 days scale-averaged variance time series of five regions, the vertical dashed line indicates the time of the snapshot. 85

4.19 The PCA analysis results of the fifteen variables in NA simulation. The top panel shows the contributions of the leading four modes. The middle panel presents the PC1 and PC2 coefficients of the fifteen variables and the projected time series in the PC1 and PC2 coordinate. The different colors in the middle panel indicate the different regions from 1 to 5, and the different markers are the different variables. UV stands for the 8-16 days scale-averaged variance of $u + v$, RV stands for the relative vorticity term, and RZ is the vertical density gradient term. The color map presents the temporal evolution of the projected time series. The bottom panel shows the PC1 and PC2 time series, and their colors are as same as the top panel. The red shadings are the LCEs shedding events, and the vertical blue lines indicate the time of reattachments. 88

4.20 The PCA analysis results of the fifteen variables in NA simulation. The top panel shows the contributions of the leading four modes. The middle panel presents the PC3 and PC4 coefficients of the fifteen variables and the projected time series in the PC3 and PC4 coordinate. The different colors in the middle panel indicate the different regions from 1 to 5, and the different markers are the different variables. UV stands for the 8-16 days scale-averaged variance of $u + v$, RV stands for the relative vorticity term, and RZ is the vertical density gradient term. The color map presents the temporal evolution of the projected time series. The bottom panel shows the PC3 and PC4 time series, and their colors are as same as the top panel. The red shadings are the LCEs shedding events, and the vertical blue lines indicate the time of reattachments. 89

4.21 The coefficients of PCA analysis results for the fifteen variables in NA simulation. The colors of the headers are as same as Figures 4.19 and 4.20 to show the order of modes and regions. The yellow shades indicate the coefficient parameter of the 8-16 days scale-averaged variance used in section 4.4. 90

4.22 The PCA analysis results of the fifteen variables in SLAT simulation. The top panel shows the contributions of the leading four modes. The middle panel presents the PC1 and PC2 coefficients of the fifteen variables and the projected time series in the PC1 and PC2 coordinate. The different colors in the middle panel indicate the different regions from 1 to 5, and the different markers are the different variables. UV stands for the 8-16 days scale-averaged variance of $u + v$, RV stands for the relative vorticity term, and RZ is the vertical density gradient term. The color map presents the temporal evolution of the projected time series. The bottom panel shows the PC1 and PC2 time series, and their colors are as same as the top panel. The red shadings are the LCEs shedding events, and the vertical blue lines indicate the time of reattachments. 91

4.23 The PCA analysis results of the fifteen variables in SLAT simulation. The top panel shows the contributions of the leading four modes. The middle panel presents the PC3 and PC4 coefficients of the fifteen variables and the projected time series in the PC3 and PC4 coordinate. The different colors in the middle panel indicate the different regions from 1 to 5, and the different markers are the different variables. UV stands for the 8-16 days scale-averaged variance of $u + v$, RV stands for the relative vorticity term, and RZ is the vertical density gradient term. The color map presents the temporal evolution of the projected time series. The bottom panel shows the PC3 and PC4 time series, and their colors are as same as the top panel. The red shadings are the LCEs shedding events, and the vertical blue lines indicate the time of reattachments. 92

4.24 The coefficients of PCA analysis results for the fifteen variables in SLAT simulation. The colors of the headers are as same as Figures 4.23 and 4.24 to show the order of modes and regions. The yellow shades indicate the coefficient parameter of the 8-16 days scale-averaged variance used in section 4.4. 93

4.25 The indicator metric of NA simulation (top panel) and SLAT simulation (bottom panel). The red shadings are the LCEs shedding events defined by the close of 17 cm SSH, and the blue vertical lines indicate the reattachments of LCEs. 94

4.26 The top panel shows the normalized relative vorticity calculated from the 8-16 days band-pass filtered velocities in the selected region of NA simulation on the 27.5 kg/m^3 σ_θ layer, the shading colors indicate the relative vorticity at the selected time shown in the title (2012-12-08). The colored contours present the relative vorticity three days before the chosen time (2012-12-05), and the purple contour shows the distribution of 17 cm SSH at the chosen time (2012-12-08). The bottom panel presents the corresponding spatial FFT of $u + iv$ at the chosen time (2012-12-08). 97

4.27 The temporal evolution of the velocity vertical profile at a chosen spot shown in the title (89.1°W, 26.2°N), the x-axis is time, and the y-axis is potential density layers. The top panel is the zonal velocity u, the middle panel is the meridional velocity v, and the bottom panel is the speed $\sqrt{u^2+v^2}$. 98

4.28 The top panel shows the normalized relative vorticity calculated from the 8-16 days band-pass filtered velocities in the selected region of NA simulation on the 27.5 kg/m^3 σ_θ layer, the shading colors indicate the relative vorticity at the selected time shown in the title (2016-10-05). The colored contours present the relative vorticity three days before the chosen time (2016-10-02), and the purple contour shows the distribution of 17 cm SSH at the chosen time (2016-10-05). The bottom panel presents the corresponding spatial FFT of $u+iv$ at the chosen time (2016-10-05). 100

4.29 The temporal evolution of the velocity vertical profile at a chosen spot shown in the title (89.1°W, 26.2°N), the x-axis is time, and the y-axis is potential density layers. The top panel is the zonal velocity u, the middle panel is the meridional velocity v, and the bottom panel is the speed $\sqrt{u^2+v^2}$. 101

4.30 The top panel shows the normalized relative vorticity calculated from the 8-16 days band-pass filtered velocities in the selected region of NA simulation on the 27.5 kg/m^3 σ_θ layer, the shading colors indicate the relative vorticity at the selected time shown in the title (2013-04-10). The colored contours present the relative vorticity three days before the chosen time (2013-04-07), and the purple contour shows the distribution of 17 cm SSH at the chosen time (2013-04-10). The bottom panel presents the corresponding spatial FFT of $u+iv$ at the chosen time (2013-04-10). 102

4.31 The temporal evolution of the velocity vertical profile at a chosen spot shown in the title (86°W, 25.4°N), the x-axis is time, and the y-axis is potential density layers. The top panel is the zonal velocity u, the middle panel is the meridional velocity v, and the bottom panel is the speed $\sqrt{u^2+v^2}$. 103

4.32 The top panel shows the normalized relative vorticity calculated from the 8-16 days band-pass filtered velocities in the selected region of NA simulation on the 27.5 kg/m^3 σ_θ layer, the shading colors indicate the relative vorticity at the selected time shown in the title (2013-07-20). The colored contours present the relative vorticity three days before the chosen time (2013-07-17), and the purple contour shows the distribution of 17 cm SSH at the chosen time (2013-07-20). The bottom panel presents the corresponding spatial FFT of $u+iv$ at the chosen time (2013-07-20). 104

4.33 The temporal evolution of the velocity vertical profile at a chosen spot shown in the title (89.1°W, 25.5°N), the x-axis is time, and the y-axis is potential density layers. The top panel is the zonal velocity u, the middle panel is the meridional velocity v, and the bottom panel is the speed $\sqrt{u^2+v^2}$. 105

4.34 The top panel shows the normalized relative vorticity calculated from the 8-16 days band-pass filtered velocities in the selected region of NA simulation on the 27.5 kg/m^3 σ_θ layer, the shading colors indicate the relative vorticity at the selected time shown in the title (2012-10-02). The colored contours present the relative vorticity three days before the chosen time (2012-09-29), and the purple contour shows the distribution of 17 cm SSH at the chosen time (2012-10-02). The bottom panel presents the corresponding spatial FFT of $u + iv$ at the chosen time (2012-10-02). 108

4.35 The top panel shows the normalized relative vorticity calculated from the 8-16 days band-pass filtered velocities in the selected region of NA simulation on the 27.5 kg/m^3 σ_θ layer, the shading colors indicate the relative vorticity at the selected time shown in the title (2012-12-02). The colored contours present the relative vorticity three days before the chosen time (2012-11-29), and the purple contour shows the distribution of 17 cm SSH at the chosen time (2012-12-02). The bottom panel presents the corresponding spatial FFT of $u + iv$ at the chosen time (2012-12-02). 109

4.36 The top panel shows the normalized relative vorticity calculated from the 8-16 days band-pass filtered velocities in the selected region of NA simulation on the 27.5 kg/m^3 σ_θ layer, the shading colors indicate the relative vorticity at the selected time shown in the title (2012-11-14). The colored contours present the relative vorticity three days before the chosen time (2012-11-11), and the purple contour shows the distribution of 17 cm SSH at the chosen time (2012-11-14). The bottom panel presents the corresponding spatial FFT of $u + iv$ at the chosen time (2012-11-14). 110

4.37 The top panel shows the normalized relative vorticity calculated from the 8-16 days band-pass filtered velocities in the selected region of NA simulation on the 27.5 kg/m^3 σ_θ layer, the shading colors indicate the relative vorticity at the selected time shown in the title (2011-10-31). The colored contours present the relative vorticity three days before the chosen time (2011-10-28), and the purple contour shows the distribution of 17 cm SSH at the chosen time (2011-10-31). The bottom panel presents the corresponding spatial FFT of $u + iv$ at the chosen time (2011-10-31). 111

4.38 The top six panels present the SOM-captured primary spatial patterns of the 8-16 days band-pass filtered normalized relative vorticity in the free-run simulation. The frequency of occurrence is shown as the subtitles of each pattern. The shading color indicates the 8-16 days band-pass filtered normalized relative vorticity reconstructed from the SOM weighted vectors. In the bottom panel, the colored dots show the BMU of the 8-16 days band-pass filtered normalized relative vorticity in the NA simulation. The shading areas indicate all the LCEs shedding events from their first separation to their final separation, and the vertical blue lines present the reattachment occurring during each LCEs shedding event. 113

4.39 The 8-16 days band kinetic energy at 27.5 kg/m^3 σ_θ layer, shown by the 8-16 cpd integrated variance-preserving spectra. The shading color indicates the $0.5 \times f \times (S_{uu} + S_{vv})$, f is the Coriolis parameter, and S_{uu}, S_{vv} are the PSD of u and v velocity. The gray contours present the 200 m, 1000 m, and 3000 m isobath. The black lines show the two profiles in Figure 4.40. The four yellow dots are the locations of the four spectra in Figure 4.41. The blue box is the Mississippi Fan wavelet region and the orange box is the Yucatan Shelf wavelet region for Figure 4.42. 114

4.40 The vertical structure of the contribution of 8-16 days band kinetic energy to the total kinetic energy at full frequencies along the two sections in Figure 4.39. The top panel is the zonal section, and the bottom panel is the meridional section. The shading colors display the percentage of the 8-16 days band kinetic energy to the total kinetic energy. 115

4.41 The variance-preserving spectra of kinetic energy at the four spots in Figure 4.39, their locations are indicated by their latitudes on each title. The spectra are calculated as $0.5 \times f \times (S_{uu} + S_{vv})$, f is the Coriolis parameter, and S_{uu}, S_{vv} are the PSD of u and v velocity. The shading color is the 95% confidence intervals. The two vertical lines presents the interval between 8-16 days band. 116

4.42 The wavelet analysis of regional averaged $u + v$ from NA simulation at 27.5 kg/m^3 σ_θ layer of region 1 (left) and region 2 (right) in Figure 4.39. The left part is the Mississippi Fan region, and the right part is the Yucatan Shelf region. The top panel shows the original input time series, the right panel in the middle is the wavelet transform, the left panel in the middle present the time-averaged power at different period in the unit of days, and the bottom panel is the temporal evolution of 8-16 days scale-averaged variance. The shadow region in the wavelet transform indicates the values below the 95$\%$ significant level. The dashed line in the bottom and right middle panels is the 95$\%$ significant level. The gray line in the right middle panel is the power via the fast Fourier transform. The shading red colors in the bottom panels are the LCEs shedding events defined by the 17 cm SSH. 117

4.43 Schematic diagram of the approximate pathway of MRG waves coming from three regions, arrow a is from the Mississippi Fan, arrow b is from the Yucatan Shelf, and arrow c is from Florida Escarpment. The black contours are the 200 m, 1000 m, and 3000 m isobaths, and the shading colors present the 9-year averaged SSH from the free-run simulation. The five chosen index regions are shown in the same color as Figure 4.8. 119

LIST OF TABLES

TABLE Page

2.1 Details of R-CESM runs used in this dissertation. 11

2.2 LCE shedding events of the free-run simulation, separation is defined by the separated 17 cm SSH contour, and short (< 1 day) reattachments and detachments are not counted in the table. The 12th LCE shedding event has two separated LCEs. The 1st one separated on 2015.10.17 and dissipated later. The 2nd LCE separated on 2015.10.21 and reattached to the LC on 2015.11.11, then it was merged by the LC to the next intrusion state. 13

2.3 LCE shedding events of the SLAT simulation, separation is defined by the separated 17 cm SSH contour, and short (< 1 day) reattachments and detachments are not counted in the table..... 14

2.4 LCE shedding events of the SLA simulation, separation is defined by the separated 17 cm SSH contour, and short (< 1 day) reattachments and detachments are not counted in the table..... 14

3.1 LCE shedding events of the SLAT simulation, separation is defined by the separated 17 cm SSH contour, and associated SSH SOM patterns are from the Figure 3.13..... 43

3.2 LCE shedding events of the SLA simulation, separation is defined by the separated 17 cm SSH contour, and associated SSH SOM patterns are from the Figure 3.13..... 45

3.3 LCE shedding events of the SLAT simulation, separation is defined by the separated 17 cm SSH contour, and associated stream function SOM patterns are from the Figure 3.19..... 52

3.4 LCE shedding events of the SLA simulation, separation is defined by the separated 17 cm SSH contour, and associated stream function SOM patterns are from the Figure 3.19..... 53

3.5 The selected EOF modes (shown in Figures 3.24 and 3.25) at different depths for SLAT and SLA simulations..... 54

4.1 Details of different scenarios of MRG Waves. The occurrence in the brackets is the case that leads to an LCE separation within 30 days after the dissipation of the wave trains. The percentage is the ratio between the occurrence that leads to the LCE separation and the total occurrence. 107

A.1 The detailed information of all moorings in Figure 2. The lower ADCP is downward when there are two ADCPs at a similar depth. All the other ADCPs are upward. The CICESE moorings also have temperature recorders at those depths. Notes: ADCP_75/300 is 75/300 kHz Acoustic Doppler Current Profiler, NCM is Nortek Aquadopp Current Meter, NR is Not Recovered, RCM-# is Recording (Doppler) Current Meter, TEMP is Temperature Recorders, T/S/P is Conductivity and Temperature Recorders, SCM is SeaGuard (Doppler type) Current Meter, S4 is InterOcean S4 Electromagnetic Current Meter. Adapted from Hamilton et al. (2015). 133

1. INTRODUCTION

1.1 Motivation

The Gulf of Mexico (GoM) is an important ocean system because of its abundant natural resources and large surrounding populations from three countries. To take advantage of these rich resources effectively, it is necessary to understand the circulation system of the GoM (Sturges and Lugo-Fernández, 2005). Advancing the understanding of the circulation in the GoM benefits all of the Gulf Coast economies and communities. The key to improving this is by filling the knowledge gaps in the understanding of the dynamics of the Loop Current System (LCS), especially the deep processes (> ~1000 m) of the Loop Current (LC) and its associated Loop Current Eddies (LCEs) (National Academies of Sciences et al., 2018).

Although aspects of this research are active and ongoing and have included numerous observational studies and numerical simulations, this dissertation uses data assimilation of multi-year observations of current velocity and hydrographic parameters (temperature, salinity, and pressure) in a coupled ocean-atmosphere numerical model. Additionally, this research investigates the dynamical processes associated with the detachment and reattachment events of LCEs to indicate their final separations, which has been largely omitted from previous investigations.

1.2 Background

1.2.1 Gulf of Mexico Circulation System

The LC is a strong current emanating from the Caribbean Sea and enters the GoM as the pre-Gulf Stream waters into the North Atlantic, which is a part of the western boundary current of the North Atlantic subtropical gyre (DiMarco et al., 2005; Schmitz Jr and McCartney, 1993). The LC flows into the GoM through the Yucatan Channel and outflows via the Straits of Florida at a mean net transport of ~27 Sv (Athié et al., 2020; Sheinbaum et al., 2016) and ~32 Sv (Baringer and Larsen, 2001; Volkov et al., 2020), respectively. The peak currents of the LC and LCEs are at ~1.9 m/s (Inoue et al., 2008). The LC could intrude to the far north (~28°N) with a large variance and

its eddy separation feature is hard to be predicted (Lugo-Fernández et al., 2016). The LCEs shed periodically with diameters from 200-400 km, impacting the circulation of the western GoM by drifting westward (Meunier et al., 2018; Vukovich and Maul, 1985). As the eddy shedding events' intervals are variable with 8-17 months from 47 cruises data between 1952 to 1976 (Behringer et al., 1977) and 9-11 months based on the altimetry sea surface height (SSH) records since 1992 (Hall and Leben, 2016), there were a series of experiments trying to understand this process better.

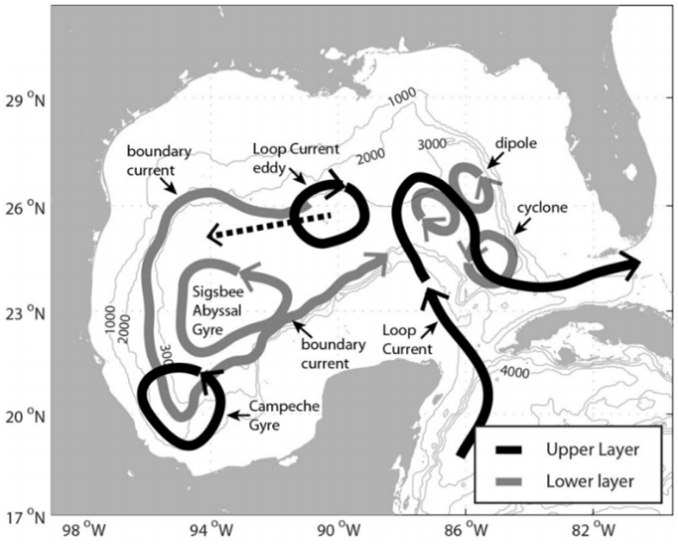

Figure 1.1: The circulation features of the upper layer (surface to ~1000 m), and lower layer (~1000 m to the seafloor) in the GoM. Modified from Furey et al. (2018).

Observations in the GoM indicate that the GoM is a highly stratified basin, which has a two-layer structure system for circulation in the deep-water regions of the GoM (Figure 1.1). The upper layer is stratified with strong vertical shears from the surface to about 800-1200 m depth, and the lower layer is weakly stratified with nearly depth-independent flows from the bottom of the upper layer to the seafloor (Hamilton, 1990, 2007, 2009; Hamilton et al., 2016; Jochens and DiMarco, 2008; Pérez-Brunius et al., 2013, 2018; Schaudt et al., 2001). The interface between the two layers is usually defined as the 6 °C isotherm depth, which has a mean depth of ~800 m and is coincident with the sill depth of the Florida Strait (Bunge et al., 2002; Hamilton et al., 2018).

The currents of the upper layer are dominated by the extension of LC and the LCEs directly. The lower layer currents show few relationships to the simultaneous variations of the currents in the upper layer (Hamilton and Lugo-Fernandez, 2001). It is suggested that the currents in the lower layer are the result of some lower-layer processes such as the Topographic Rossby Waves (TRWs), baroclinic instabilities induced by the LC, and deep eddies, which are generated by the fluctuations of the LC north intrusion (Donohue et al., 2016b; Furey et al., 2018; Hamilton, 2009). The near-bottom intensified flows along the boundaries are due to the propagation of TRWs, and these TRWs are mainly from the dissipation of deep eddies (Tenreiro et al., 2018).

Considering the conservation of mass, an important outflow of the deep circulation through the Yucatan Channel should balance the input volume of the LC intrusion (Mauli, 1977). This deep Yucatan outflow shows a relationship to the changes in the volume of the LC based on a simple conceptual box model (Bunge et al., 2002; Sheinbaum et al., 2016). For the deep circulation system, this outflow is from the western GoM, crosses the 90°W meridian, then southward through the Yucatan Channel back to the Caribbean Sea. This balances the input water masses from the LC shedding events (Chang and Oey, 2011). Therefore, the variations of the LC impact the circulation of the entire deep-water system of the GoM.

1.2.2 Loop Current Dynamics

In 2009, the LC Dynamics Experiment (2009-2011) provided two and a half years of observations with 30-50 km spatial and 12 hours temporal resolution capable of resolving the fundamental processes associated with the dynamics of the LC. The LC Dynamics Experiment focused on the intrusion of the LC in the eastern GoM to improve the understanding of the LC with a fine vertical structure (Hamilton et al., 2015; Lugo-Fernández, 2016). These results show the LC has large variations in all three directions, including the location, the velocity, and the depth (Donohue et al., 2016a; Lugo-Fernández et al., 2016; Sheinbaum et al., 2016). All these variations impact the circulation in the GoM directly or through the energetic large-scale eddies. The LCEs extract potential energy from the mean field of the LC, then store this potential energy in the sloping isopycnals of the LCEs, and finally convert this energy to eddy kinetic energy (EKE) (Donohue et al., 2016b).

The wind forcing over the Cayman basin intensifies and increases the Yucatan transport, which will lead to a larger LC penetration, and increase the Yucatan Current vorticity (Athié et al., 2020; Chang and Oey, 2012, 2013). When the LC enters the GoM, the LC frontal eddies are formed by baroclinic instabilities generated near the steep topography of Campeche Bank, which propagates along the periphery of the LC and contributes to the necking down process of the LC later (Rudnick et al., 2015; Walker et al., 2009). During the north intrusion of LC, the deep dipoles of eddies are generated through the potential vorticity (PV) conservation beneath the LC in the relatively flat deep Gulf (Furey et al., 2018; Hamilton et al., 2019). After a few months of the LC penetration, the separation of LCEs from the LC is triggered by the consequence of several mechanisms, including the deduction of the source of the LC from the Yucatan inflow, the necking down process helped by the LC frontal eddies formed by local and remote processes, and the deep eddies jointly intensified with the meanders of southward LC through the baroclinic instabilities with a 90° phase lead (Athié et al., 2012; Chang and Oey, 2012, 2013; Donohue et al., 2016b; Hamilton et al., 2019; Oey, 2008). The Yucatan inflow also shows an important effect on the eddy detachment events. As the inertia effect could lead the base eddy of the LC to grow forever and the beta effect could form a chain of westward-propagating eddies, the detachment threshold would be the competition between the westward wave speed and the eddy growth rate (Nof, 2005). Then, the decrease in Yucatan inflow generates a larger difference between westward-propagating speed and the growth rate by reducing the input. Thus, the LCEs were more likely to be separated when the transport of Yucatan inflow decreased (Athié et al., 2020). By June 2020, there were 34 LCEs separations from 1973 to 1999, and another 40 LCEs separations after 1999 on the record (Sturges and Leben, 2000).

During the westward drifting of LCEs, the TRWs along the north and northwest continental slopes are incited by the deep dipoles, and the deep cyclone intensifies the Sigsbee Abyssal Gyre (Furey et al., 2018; Hamilton, 1990, 2009; Oey and Lee, 2002). The Caribbean Subtropical Underwater (SUW) within the LCEs is transformed into the precursor of the Gulf Common Water (GCW) by diffusion of the high subsurface salinity to the surrounding waters in the western GoM (Sosa-Gutiérrez et al., 2020). Additional to the salinity, the heat in the LCEs is also released in the

central GoM, primarily toward the surrounding water masses (Meunier et al., 2020). The TRWs along the western slope of the Bay of Campeche are caused by the LCEs and the deep anticyclone. When they impinge on the western boundary, the deep boundary currents and the cross-shelf transport will be enhanced (Guerrero et al., 2020; Kolodziejczyk et al., 2011; Sutyrin et al., 2003). Simultaneously, the Yucatan outflow is intensified as there is an amount of water trapped in the LCEs from the Caribbean Sea entering the GoM (Bunge et al., 2002; Chang and Oey, 2011). As the LC contains more momentum and heat than the surrounding water (Vidal et al., 1992), the presence of LC and LCEs could also impact the atmosphere via enhancing the passing hurricanes (Brooks, 1983; Jaimes et al., 2016; Pallàs-Sanz et al., 2016; Spencer et al., 2016).

1.3 Hypotheses

As the temporal and spatial coverage and resolution of observations were improved in recent decades, most of the recent LCEs shedding events showed at least a one-time reattachment. The triggers of these reattachments are still a gap in this story. Thus, the underlying objective of this research is to understand the mechanisms of the reattachments of LCEs. When the LCEs separate from the LC and move westward into the GoM, the deep dipoles are generated by the conservation of PV under the LCEs like the intrusion of the LC (Cushman-Roisin et al., 1990; Welsh and Inoue, 2000). As the LCEs move westward, they squeeze the lower layer in front of them and generate a leading anticyclonic deep eddy. At the same time, the lower layer behind the westward LCEs is stretched, then the trailing cyclonic deep eddy is generated.

The entire LCEs shedding process has been separated into several states via the Self-organizing Map (SOM) analysis of the satellite dataset (Liu et al., 2016; Nickerson et al., 2022), containing most surface factors that could impact the LCS separation. Beyond the intrusion, separation, and retraction states of the LC, the Campeche Bank anchoring and West Florida Shelf anchoring states are identified to be a consequence of the topographic β effect. A detailed analysis of the relationship between surface and subsurface dynamics has not been fully developed. Therefore, using the SOM method to capture the significant temporal and spatial features of the LCS between the upper and lower layers, and establish the metric to inform the LCEs separations from the bottom of the

LCS to fill these gaps in the deeper layers is our primary objective.

Our primary hypothesis for the mechanism of LCEs separations is that the relatively high-frequency variance stimulated by the LC can increase the rating of instabilities as positive feedback, and trigger the detachments of LCEs when the energy of the high-frequency band exceeds the threshold. These high-frequency variations are already identified by the wavelet analysis of in-situ observations below the LC (Hamilton et al., 2016), but they are not being further discussed like the frequency band of the LCEs separations.

1.4 Objectives

To test our hypothesis of the LCEs reattachments, we need to investigate the evolution and behavior of the deep dipole of eddies beneath the LC and LCEs and the structure of surrounding isopycnals. This requires addressing three sub-objectives (with corresponding hypotheses in the order of progress):

Objective 1: Validate the model dynamics of the free-run R-CESM model, and characterize the LCS dynamics in numerical simulations.

Hypothesis 1: Self-organizing Map (SOM) and Empirical Orthogonal Function (EOF) describe the temporal and spatial evolution of deep-water GoM circulation features. The model dynamics of the R-CESM will be validated before extracting the dominant features via SOM and EOF. The upper-layer evolution will be shown by the characteristics of SSH, and the features of the lower layer will be described by the stream function. The potential density layers will be used to derive the lower-layer variables following the ocean dynamics. As the LCS is the most outstanding feature in the upper layer, the SSH patterns will show the different stages of the LCS. In the lower layer, we expect some spatial features related to certain upper-layer patterns.

Objective 2: Compare three numerical simulations to the in-situ observations to quantify the improvements in data assimilation of different schemes.

Hypothesis 2: The assimilation of surface observations should significantly improve the simulations of the LC by constraining the temporal and spatial evolution of ocean surface properties such as SSH and SST. Compared to the observations, the major differences in LCS intensity and

LCS structure of R-CESM simulations are the overestimated LC and underestimated lower layer, which could be improved by assimilating the observations to modify the simulations. The entire water column will be modified following the surface constraints through the model dynamical adjustment. The two assimilating schemes will show the differences in the vertical propagation of signals from the upper layer to the lower layer, as the impacted depths of data assimilation are set to different limitations. The improvement from data assimilation will also be shown by comparing different simulations and different assimilating schemes.

Objective 3: Define an indicator metric that relates the upper and lower layers to inform LCEs separation prediction.

Hypothesis 3: Principal Component Analysis (PCA) of deep-isopycnal variability indicates LCEs shedding events. Combining the temporal and spatial evolution of the different variables along the isopycnals below the LC is an ideal metric to establish the connection between the upper and lower layers, whose variability contains the features of both layers. This metric should include several regions which show the occurrence of LCEs detachments with varying locations. The leading variable will be the high-frequency variations stimulated by the LCEs shedding events. PV will also be included to represent the variations in rotation and structure.

The length scales of these deep eddies are about 50-120 km with a 30-50 km decorrelation scale (Donohue et al., 2006; Furey et al., 2018; Hamilton et al., 2019). Therefore, the in-situ data from the LC Dynamics Experiment (2009-2011) in the GoM does not have the capability to capture the details of deep eddies and related processes with a roughly 30 km resolution (roughly 50 km resolution without bottom moorings) (Hamilton et al., 2015). As numerical models and data simulations have been improved a lot in recent decades, they can output a continuous dataset covering the entire region with sufficient temporal and spatial resolutions (Hurrell et al., 2013; Kantha and Clayson, 2000; Karspeck et al., 2018). Numerical models' outputs could be an ideal dataset to characterize the mechanisms of LCEs reattachments. Compared to the observations in the lower layer, the simulations still show some unrealistic features, such as a relatively more stable bottom layer whose EKE is generally less than one-half of observations (Morey et al., 2020; Rosburg et al.,

2016). Thus, the ***final objective*** of our research is to compare and evaluate the regional numerical simulation by assimilating the observations from satellite products, and determine some critical areas whose variations can be used to predict the evolution of the LCS.

1.4.1 Organization

All the datasets and methods used in this research are shown in section 2. Section 3 presents the validation of R-CESM model dynamics and the extracted features of LCS at multiple layers for ***objective 1***. The comparison between observations and different numerical simulations is made before the further analysis of lower-layer variations in section 4. We will use the free-run R-CESM outputs and the better assimilative outputs to further analyze the LCS characteristics under the LC, then define a metric that connects the variations between upper and lower layers, which could indicate the likelihood of detachment or reattachment for ***objective 2&3*** in section 4. Section 5 is the conclusions and future works.

2. DATA AND METHODS

2.1 Loop Current Dynamics Experiment 2009-2011

This mapping array consists of 25 Pressure Inverted Echo Sounder (PIES), 9 Science Applications International Corporation (SAIC) tall moorings, and 7 SAIC short moorings. This array extends from 89°W to 85°W and 25°N to 27°N with approximately 30 km resolution (approximately 50 km resolution for PIES only) and lasts for roughly 2.5 years from April 2009 to November 2011. The PIES (purple diamonds in Figure 2.1) were deployed at the seafloor with a pressure sensor measuring the bottom pressure as a reference and an inverted echo sounder to measure the round-trip acoustic travel times via emitting 12 kHz sound pulses toward the ocean surface. The obtained round-trip travel-time data are used to reconstruct the profiles of the water column based on the Gravest Empirical Mode (GEM). The tall moorings (orange squares in Figure 2.1) consist of an upward-looking 75 kHz acoustic Doppler current profiler at 450 m depth, point current meters at 600 m, 900 m, 1300 m, 2000 m, and 100 m above the bottom, and temperature recorders at 75 m, 150 m, 250 m, 350 m, 525 m, 750 m, 1100 m, 1500 m depth. The short moorings (cyan squares in Figure 2.1) only have one current meter at 100 m above the bottom. There is also a Centro de Investigación Científica y de Educación Superior de Ensenada (CICESE) array consisting of 18 stations along three sections from June 2009 to June 2011 (purple and red squares in Figure 2.1). The detailed information of all the moorings is shown in Table A1 (Appendix A), and further information can be found in Hamilton et al. (2015).

Our research will use the CICESE array to constrain the intensity and depth of the LC and compare the model dynamics of deep layers with the mapping array in the Exclusive Economic Zone of the United States. The processed dataset we have is 72-hour low-pass filtered with a fourth-order Butterworth filter and subsampled at 12-hour intervals since the different sampling frequencies from the multiple sensors vary from minutes to hours (Hamilton et al., 2015).

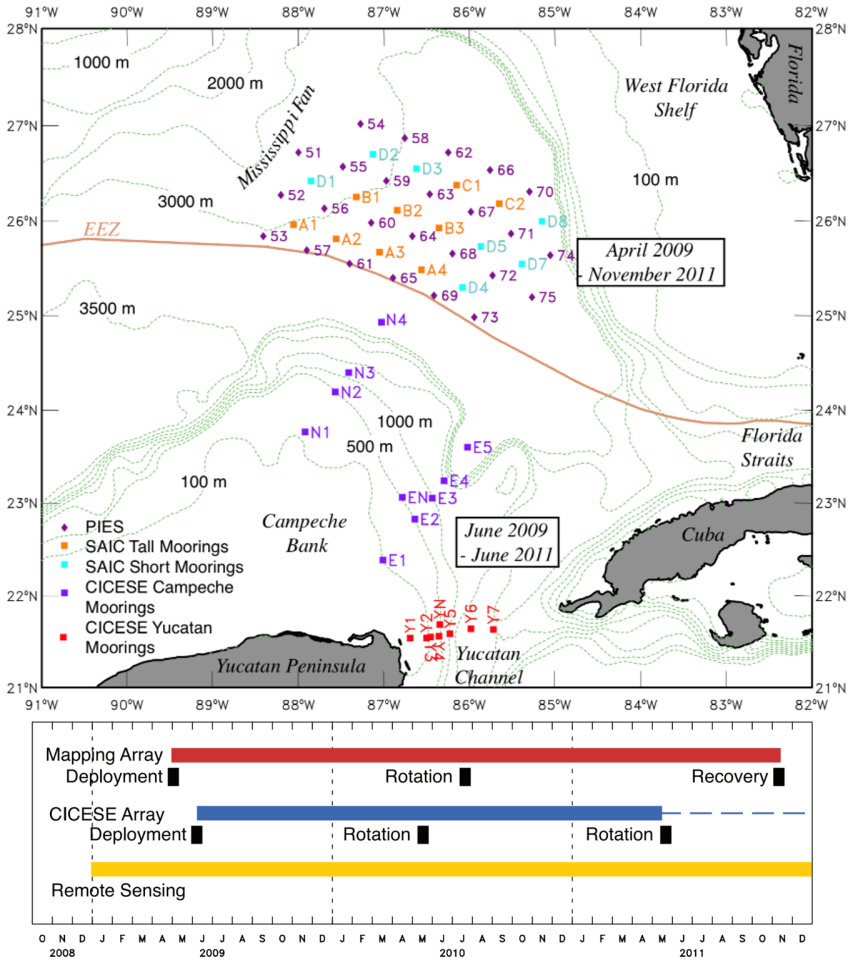

Figure 2.1: The locations of the LC moorings (top panel), and the data acquisition intervals (bottom panel). Modified from Hamilton et al. (2015).

2.2 Regional Community Earth System Model

The R-CESM is a fully coupled regional model (Fu et al., 2021) developed jointly by the National Center for Atmospheric Research (NCAR) and Texas A&M University (TAMU) based on the coupling framework and software infrastructure used by the Community Earth System Model (CESM) version 2.1 (Danabasoglu et al., 2020). The Weather Research and Forecasting (WRF) model (Skamarock, 2008) and the Regional Ocean Modeling System (ROMS) (Shchepetkin and McWilliams, 2005) are incorporated into the CESM as additional components. For the CESM flux scheme, the atmosphere-ocean (A/O) fluxes are computed by the Common Infrastructure for

Modeling the Earth (CIME) coupling framework and sent to WRF and ROMS (red arrows in the left panel of Figure 2.2). For the WRF flux scheme, A/O fluxes are directly computed by WRF and transmitted to ROMS via CIME (yellow arrows in the left panel of Figure 2.2). The Atmosphere-land (A/L) fluxes are computed by the Community Land Model (CLM) in CESM. The atmosphere state (green arrows in the left panel of Figure 2.2) includes temperature, humidity, wind components, surface radiative fluxes, and surface pressure. The ocean state (blue arrows in the left panel of Figure 2.2) includes SST and ocean surface current. The A/O and A/L fluxes include momentum, heat, and moisture fluxes, some additional variables for the boundary layer scheme of WRF, and some diagnostic variables. All the used simulations are shown in Table 2.1.

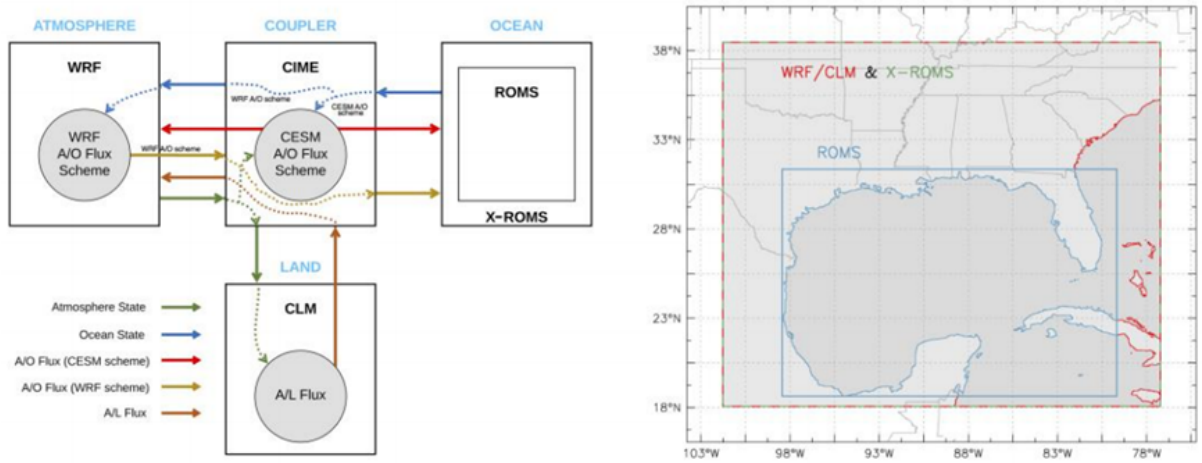

Figure 2.2: The schematic of the R-CESM component models and structure of surface flux calculation (left panel), and the R-CESM model domains for the GoM (right panel). Modified from Fu et al. (2021).

Table 2.1: Details of R-CESM runs used in this dissertation.

Simulation Name	Assimilated Dataset	Simulation Period
Free Run (Nature/NA)	None	Jan. 2010 - Dec. 2018 (3 hr)
SSH&T Run (SLAT)	SSHA and SST to 2000 m	Jan. 2010 - Dec. 2012 (3 hr)
SLA Run (SLA)	SSHA only to the bottom	Feb. 2010 - Nov. 2012 (6 hr)

2.2.1 Free Run (Nature/NA) Description

To test the capability of the R-CESM in the GoM, we currently start our analysis with a regional (right panel in Figure 2.2) 3 hourly state-of-the-art high-resolution (9 km WRF and 3 km ROMS with 50 σ layers) fully coupled simulation from January 2010 to December 2018 without the use of any nudging in the interior of the model domain. The comparison of the annual-mean R-CESM SST with 1/20° horizontal-resolution Group for High Resolution Sea Surface Temperature (GHRSST) product indicate that the R-CESM can simulate the mean distribution of SST in the GoM accurately with a difference less than 0.25°C in most of the GoM, a significant improvement from global high-resolution models with biases of 0.5°C - 1°C (Small et al., 2014). The comparison of the geostrophic EKE between the 1/4° horizontal-resolution daily Data Unification and Altimeter Combination System (DUACS) data and R-CESM shows similar magnitudes in the LC region. Thus, R-CESM can provide considerable support for our research. All the LCE shedding events are shown in Table 2.2.

2.2.2 Assimilative Runs Description: SLAT and SLA

Three satellite datasets are assimilated to make the R-CESM outputs more approach to the observations. The detailed procedure of data assimilation is also described in Fu et al. (2021). The first assimilative simulation is from January 2010 to December 2012 at the exact resolution as the free-run simulation. Since the satellite data is limited to the ocean surface, the impact of assimilation is constrained to the upper ~2000 m. The second assimilative simulation is 6 hourly outputs with the same spatial resolution from February 2010 to October 2011, assimilating only sea surface height anomaly (SSHA) data. The impact of assimilation is set to the whole water column in the second assimilative run. All the LCE shedding events of the sea surface height and temperature (SSHT) run and sea level anomaly (SLA) run are shown in Table 2.3 and Table 2.4.

The assimilated SSHA data is provided by the Copernicus Climate Change Service (C3S) from 1993 to the present. It is a 1/4° x 1/4° gridded daily dataset for the global ocean. This C3S dataset merges two satellites all time steps to achieve a homogeneous and stable sea surface height record,

Table 2.2: LCE shedding events of the free-run simulation, separation is defined by the separated 17 cm SSH contour, and short (< 1 day) reattachments and detachments are not counted in the table. The 12th LCE shedding event has two separated LCEs. The 1st one separated on 2015.10.17 and dissipated later. The 2nd LCE separated on 2015.10.21 and reattached to the LC on 2015.11.11, then it was merged by the LC to the next intrusion state.

LCE Order	Separation Start	Reattachment (Redetachment) Dates	Final Separation
1	2010.06.14	2010.06.19 (09.18); 2010.10.27	2010.11.14
2	2010.12.10	2010.12.12 (12.14); 2011.01.01 (02.26); 2011.03.06	2011.03.30
3	2011.07.06	2011.07.31 (08.06); 2011.08.08 (08.16); 2011.08.18	2011.08.23
4	2011.10.12	2011.11.15	2012.02.11
5	2012.07.31	2012.10.18	2012.10.21
6	2012.11.30	None	2012.11.30
7	2013.03.30	2013.04.14 (05.06); 2013.05.15 (07.19); 2013.07.24 (08.05); 2013.08.22	2013.09.02
8	2013.10.03	2013.10.13 (2014.01.05); 2014.01.11 (02.02); 2014.02.03 (04.01); 2014.04.11	2014.04.19
9	2014.07.08	2014.07.18	2014.07.28
10	2015.01.12	2015.03.19 (04.29); 2015.05.24	2015.05.27
11	2015.09.14	2015.10.14 (10.17 & 10.21); 2015.11.11	2015.10.21
12	2016.04.25	None	2016.04.25
13	2016.09.05	2016.09.13	2016.09.28
14	2017.06.09	None	2017.06.09
15	2017.09.01	2017.09.18 (09.20); 2017.10.06 (10.18); 2017.10.25	2017.10.29
16	2018.03.15	None	2018.03.15
17	2018.06.06	None	2018.06.06
18	2018.07.18	None	2018.07.18
19	2018.11.01	2018.11.05	2018.12.10

one satellite for long-term reference and stability, and the other time-variant satellite is used to improve accuracy.

The assimilated sea surface temperature (SST) data is the Optimum Interpolation Sea Surface Temperature (OISST) provided by National Oceanic and Atmospheric Administration (NOAA) based on the Advanced Very High Resolution Radiometer (AVHRR) and Advanced Microwave Scanning Radiometer on the Earth Observing System (AMSR-E). The AVHRR is from 1981 to the present, and the AMSR-E is from 2002 to 2011. Thus, OISST is based on both AVHRR and

AMSR-E from 2002 to 2011, and only from AVHRR after October 2011. This dataset is a 1/4° x 1/4° gridded daily dataset for the global ocean as well, combining different platforms, not only satellites but also ships and buoys.

Table 2.3: LCE shedding events of the SLAT simulation, separation is defined by the separated 17 cm SSH contour, and short (< 1 day) reattachments and detachments are not counted in the table.

LCE Order	Separation Start	Reattachment (Redetachment) Dates	Final Separation
1	2010.06.10	2010.06.25 (06.28); 2010.08.03 (08.15); 2010.09.06	2010.09.26
2	2011.07.24	2011.08.02	2011.08.04
3	2011.11.12	2011.11.14 (11.18); 2011.12.12	2011.12.21
4	2012.06.24	2012.08.02	2012.08.09

Table 2.4: LCE shedding events of the SLA simulation, separation is defined by the separated 17 cm SSH contour, and short (< 1 day) reattachments and detachments are not counted in the table.

LCE Order	Separation Start	Reattachment (Redetachment) Dates	Final Separation
1	2010.06.05	2010.07.11 (07.19); 2010.08.07 (08.12); 2010.09.04	2010.09.27
2	2011.07.28	None	2011.07.28
3	2011.11.19	2011.12.13 (12.21); 2012.01.11	2012.01.18
4	2012.06.24	2012.07.29	2012.08.13

2.3 Metric Definitions

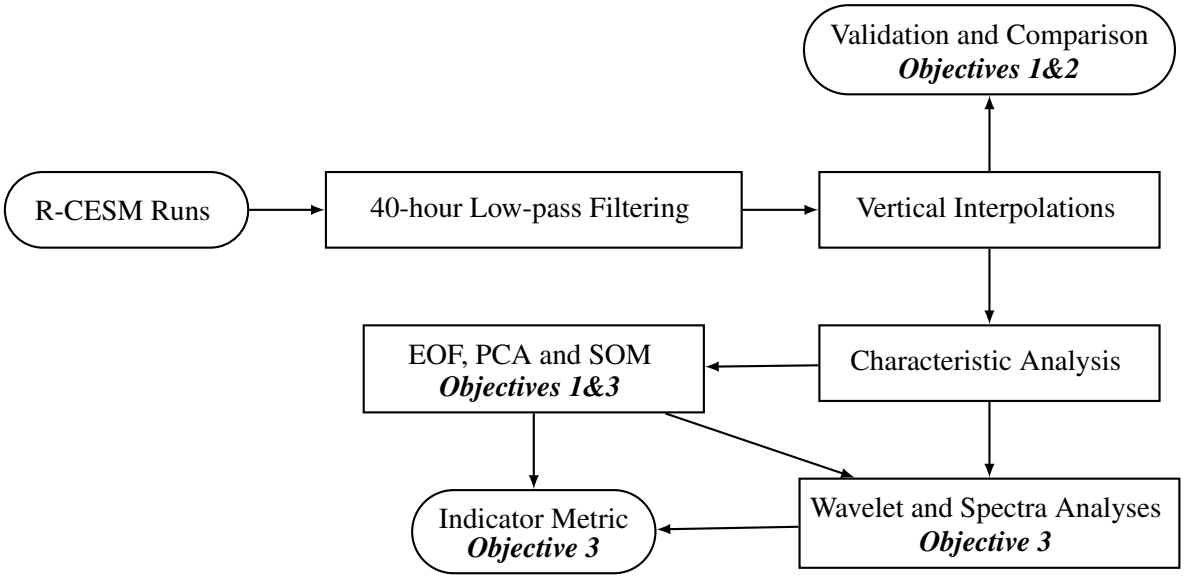

Figure 2.3: Processing flow chart of the R-CESM simulations in this research. The detailed methods are described in Sections 2.3 and 2.4, and related objectives are listed below the corresponding methods.

The processing of the three R-CESM simulations is shown in Figure 2.3. Firstly, all the used R-CESM outputs are 40-hour low-pass filtered, including horizontal velocities, temperature, salinity, and some derived quantities in this section. Secondly, the simulated variables are interpolated into two different vertical coordinate from the R-CESM σ coordinate. The vector correlation is used to compare the free-run simulation and the assimilative simulations. Then, we calculate the stream function and potential vorticity (PV) at different layers to identify the location and intensity of the lower-layer leading anticyclone and trailing cyclone. The LCE will be identified with the 17 cm SSH (Leben, 2005). Finally, the characteristic analyses in section 2.4 are applied to the stream function and PV at multiple layers to obtain the major features of the LCS at different depths.

2.3.1 Lanczos Cosine Filter

In this research, as the low-frequency (> 40 hours) variances of the LCS are our target and the temporal resolution of R-CESM is higher than our demands, we use a symmetric weighted Lanczos cosine filter to filter out the variances with periods larger than 0.6 cycles per day (Cho et al., 1998; Nowlin et al., 2005). The major processes related to the generation of LCEs were considered as 40 - 100 days (Donohue et al., 2016b; Hamilton et al., 2019). Therefore, this 40-hour low-pass filter will not impact the dominant procedure of the LCEs' separation and will keep some relative high-frequency variances (< 1 month) to be used for more detailed research.

The Lanczos cosine filter is constructed with the following equations 2.1 and 2.2 as the reconstruction kernel $L(t)$ and filter weighted function $F(t)$ (Duchon, 1979; Harris, 1978).

$$L(t) = \begin{cases} 1, & t = 0 \\ \dfrac{[1 + cos(\pi t/N)]sin(2\pi t f_c)}{4\pi t f_c}, & t \neq 0 \end{cases} \tag{2.1}$$

$$F(t) = L(t) / \int_{-N}^{N} L(t)dt \tag{2.2}$$

In the equations 2.1 and 2.2, N is the width of the filter in one direction, the total width of the window is $2N + 1$, t is the point of the filter from $-N$ to N, f_c is the cutting frequency which is 1/40 in our research. This filter will cut the power spectrum to 1/4 power and 1/2 amplitude at the selected cutting frequency. The used Python code is modified from the MATLAB code (Howard and DiMarco, 1998) based on the FORTRAN code of Steve Worley.

2.3.2 Vertical Structure

The R-CESM outputs are in σ coordinate, which means they have the same number of vertical grid points everywhere in the model domain. The thickness of the σ layers varies from different grid points due to the change of bathymetry (Chassignet et al., 2006). The simulations presented here are in 50 σ layers, squeezing in the upper part and stretching in the lower part (Fu et al., 2021). Therefore, we need to do the vertical interpolation to transfer the outputs into a z coordinate system

for some further research. To be more efficient, the selected depths for our research are only 8 z layers: 50 m, 300 m, 500 m, 1000 m, 1500 m, 2000 m, 3000 m, and 4000 m. As the upper part is more condensed, we keep 4 layers in the top 1000 m. The lower layers approaching the interface between the upper and lower layers are where we are interested, so 1500 m and 2000 m are selected. The 3000 m layer is close to the bottom in the eastern GoM deep region, and 4000 m is for the upstream region in the Caribbean Sea. Since the original vertical intervals of R-CESM outputs at the bottom layers are smaller than 500 m, we use the linear method for the vertical interpolation.

The R-CESM outputs are also interpolated into a potential density anomaly σ_θ coordinate on 9 selected isopycnals shown in Figure 2.4: 25 kg/m^3, 26 kg/m^3, 27.1 kg/m^3, 27.3 kg/m^3, 27.4 kg/m^3, 27.5 kg/m^3, 27.58 kg/m^3, 27.62 kg/m^3, and 27.64 kg/m^3. Figure 2.4 presets a time-averaged profile along 25 °N in SLAT and SLA simulations.

The 25 and 26 kg/m^3 layers are the top layers, from ~ 100 to 300 m in the LC area. The layer between 27.4 kg/m^3 and 27.5 kg/m^3 is approximately the 6 °C isotherm depth in SLAT simulation (4 °C isotherm depth in SLA simulation), ~ 800 to 1000 m at the bottom of the LC, which is identified as the interface between upper and lower layers. Layers from 27.58 to 27.64 kg/m^3 are selected to define the lower layers for PV calculation (27.60 and 27.62 kg/m^3 layers), which layer is between 1000 to 2000 m in depth, avoiding the primary features from the upper-layer LC. As the ocean dynamics follow the isopycnals, the calculation PV, and corresponding characteristics analyses are mainly based on the σ_θ coordinate.

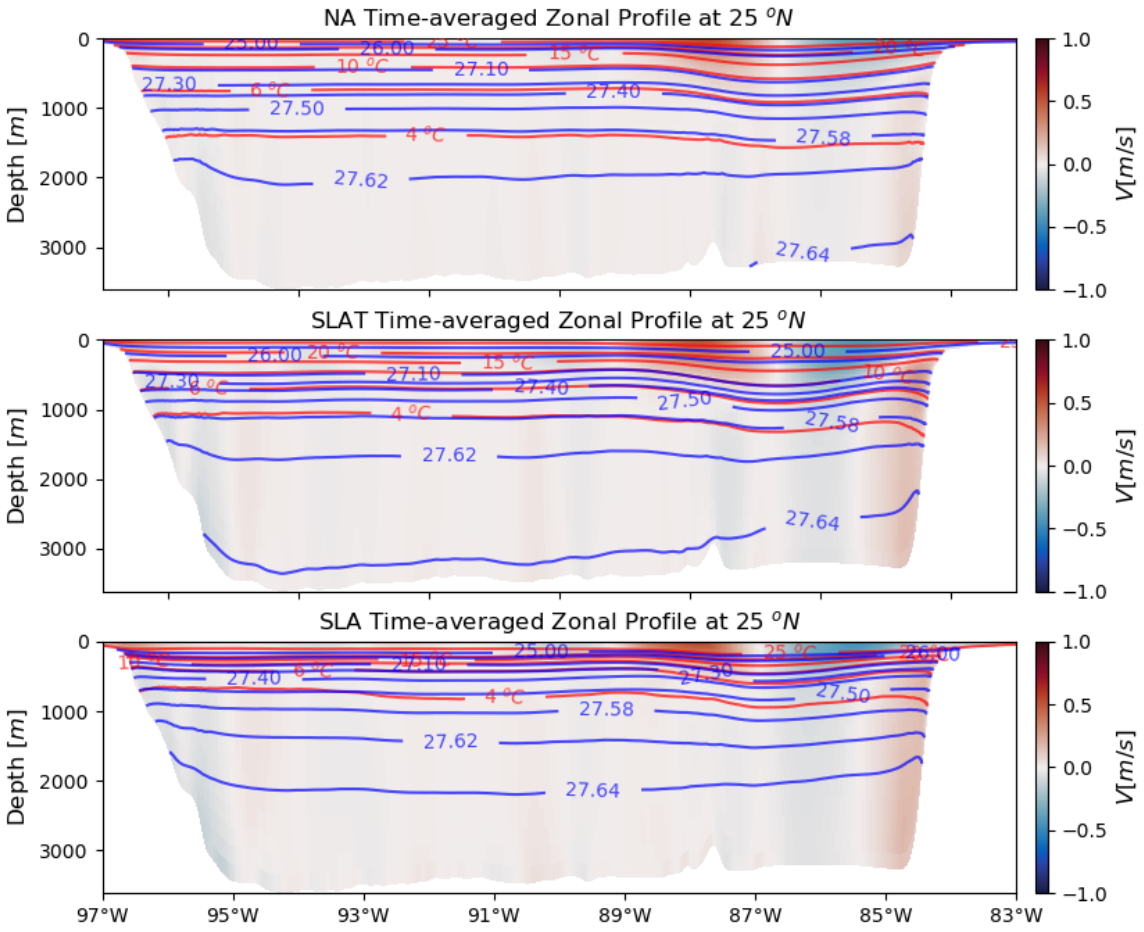

Figure 2.4: Time-averaged zonal z coordinate section of meridional velocity along 25 °N in NA (top panel), SLAT (middle panel) and SLA (bottom panel) simulations. The blue contours indicate the depths of the 9 selected potential density layers, the red contours are the isotherms, and the background colors are the meridional velocity.

The R-CESM outputs have a 3 km horizontal resolution, which could mitigate the problem generated by the sharp topographic changes in the σ coordinate and cause small depth changes between neighbor grid points. Therefore, we do the calculation for most variables in both σ_θ and z coordinates, such as the stream function and vorticity.

2.3.3 Vector Correlation

Vector correlation is calculated to check the relationship between the observations and simulations. As the assimilated data are SSHA and SST at the ocean surface rather than velocity data in the ocean, comparing the observed velocities and the simulated velocities at the same locations is used to check the model dynamics.

The equations 2.11 to 2.6 (Crosby et al., 1990) are used in this research to calculate the temporal correlation of velocities at the same spatial locations between R-CESM and observations.

$$\begin{aligned} f_{vc}(u_1, v_1, u_2, v_2) = \sigma^2(u_1, u_1)\big[\sigma^2(u_2, u_2) \cdot \sigma^2(v_1, v_2) + (\sigma^2(v_2, v_2) \cdot \sigma^2(v_1, u_2)\big] \\ +\sigma^2(v_1, v_1)\big[\sigma^2(u_2, u_2) \cdot \sigma^2(u_1, v_2) + (\sigma^2(v_2, v_2) \cdot \sigma^2(u_1, u_2)\big] \\ +2\big[\sigma(u_1, v_1) \cdot \sigma(u_1, v_2) \cdot \sigma(v_1, u_2) \cdot \sigma(u_2, v_2)\big] \\ +2\big[\sigma(u_1, v_1) \cdot \sigma(u_1, u_2) \cdot \sigma(v_1, v_2) \cdot \sigma(u_2, v_2)\big] \\ -2\big[\sigma^2(u_1, u_1) \cdot \sigma(v_1, u_2) \cdot \sigma(v_1, v_2) \cdot \sigma(u_2, v_2)\big] \\ -2\big[\sigma^2(v_1, v_1) \cdot \sigma(u_1, u_2) \cdot \sigma(u_1, v_2) \cdot \sigma(u_2, v_2)\big] \\ -2\big[\sigma^2(u_2, u_2) \cdot \sigma(u_1, v_1) \cdot \sigma(u_1, v_2) \cdot \sigma(v_1, v_2)\big] \\ -2\big[\sigma^2(v_2, v_2) \cdot \sigma(u_1, v_1) \cdot \sigma(u_1, u_2) \cdot \sigma(v_1, u_2)\big] \end{aligned} \tag{2.3}$$

$$\begin{aligned} g_{vc}(u_1, v_1, u_2, v_2) = \big[\sigma^2(u_1, u_1) \cdot \sigma^2(v_1, v_1) - \sigma^2(u_1, v_1)\big] \\ \cdot\big[\sigma^2(u_2, u_2) \cdot \sigma^2(v_2, v_2) - \sigma^2(u_2, v_2)\big] \end{aligned} \tag{2.4}$$

$$\sigma^2(u, v) = E(u \cdot v) - E(u) \cdot E(v) \tag{2.5}$$

$$r_{vc}^2 = f_{vc}/g_{vc} \tag{2.6}$$

Equation 2.6 gives the vector correlation coefficient r_{vc}^2 based on all the covariance terms between the u and v velocities at the two selected locations. In equations 2.11 to 2.6, u and v are the zonal velocity and meridional velocity, σ is the standard deviation operator of the two inputs.

All the correlation coefficients are statistically significant at the 95% confidence level (CL) in

this research. The calculation of 95% CL is based on the effective degrees of freedom (EDoF) (Chelton, 1983; Thomson and Emery, 2014) instead of degrees of freedom. EDof is calculated by equations 4.1 and 2.8.

$$\rho_{xy}(\tau) = \frac{Cov_{xy}(\tau)}{\sigma(x,x) \cdot \sigma(y,y)} \tag{2.7}$$

$$EDoF = \frac{N}{\sum_{\tau=-\infty}^{\infty} \left[\rho_{xx}(\tau) \cdot \rho_{yy}(\tau) + \rho_{xy}(\tau) \cdot \rho_{yx}(\tau)\right]} \tag{2.8}$$

In equations 4.1 and 2.8, σ is the same standard deviation operator as equation 2.5. The two input time series are shown as x and y, $Cov_{xy}(\tau)$ is the cross/auto-covariance function of lagging τ between the two inputs x and y. Therefore, $\rho_{xy}(\tau)$ is the normalized cross/auto-covariance function of lagging τ between x and y, and N is the total length of the input time series.

2.3.4 Stream Function

Stream function is introduced to discuss the evolution of both zonal and meridional velocities as one variable to simplify the dynamics problems. The stream function $\boldsymbol{\psi}$ is defined by the traditional formula shown as equation 2.9 (Batchelor, 1967; Lamb, 1932), where $\boldsymbol{u}$ and $\boldsymbol{v}$ are the northward and eastward ocean velocities in the z coordinate, x and y are longitude and latitude, z is depth, and t is time.

$$\boldsymbol{\psi}(x,y,z,t) = \int \boldsymbol{u}(x,y,z,t)dy - \boldsymbol{v}(x,y,z,t)dx \tag{2.9}$$

Stream function in the σ_θ coordinate is only calculated for some lower layers in the deep GoM region where the bottom is relatively flat to avoid the sharp depth change caused by the tilt topography. Therefore, the stream function $\boldsymbol{\psi}$ in the σ_θ coordinate is calculated via the same equation 2.9 but only for a single σ_θ layer, which is more consistent with model dynamics. For instance, we calculate the stream function at the 27.5 kg/m^3 σ_θ layer, which is around 1000 m depth in the LC region. When the 27.5 kg/m^3 σ_θ layer approaches the coastal slopes and reaches its end, this contour line is determined as the boundary of the stream function.

2.3.5 Potential Vorticity

For further research of the LCS dynamics, Ertel's PV $\boldsymbol{q}$ is calculated by equation 2.10 (Candela et al., 2002; Pedlosky et al., 1987), including planetary vorticity, relative vorticity, and stratification. This simplified equation is based on the Boussinesq approximation and neglects derivatives of the vertical velocity, as the terms containing derivatives of vertical velocity can be dropped via scale analysis (Beal and Bryden, 1999). For each term from left to right, ρ_0 is the reference mean density constant (1025 kg/m^3), f is the planetary vorticity (Coriolis parameter), $\partial \boldsymbol{v}/\partial x - \partial \boldsymbol{u}/\partial y$ is the relative vorticity, $\partial \rho/\partial z$ is the vertical gradient of potential density refers to the stratification, the rest two terms are the shear vorticity along isopycnals combining stratification.

$$q(x, y, z, t) = \frac{1}{\rho_0}\left[\left(f + \frac{\partial \boldsymbol{v}}{\partial x} - \frac{\partial \boldsymbol{u}}{\partial y}\right)\frac{\partial \rho}{\partial z} + \frac{\partial \boldsymbol{u}}{\partial z}\frac{\partial \rho}{\partial y} - \frac{\partial \boldsymbol{v}}{\partial z}\frac{\partial \rho}{\partial x}\right] \tag{2.10}$$

$$q(x, y, z, t) = \frac{1}{\rho_0}\left[\left(f + \frac{\partial \boldsymbol{v}}{\partial x} - \frac{\partial \boldsymbol{u}}{\partial y}\right)\frac{\partial \rho}{\partial z}\right] \tag{2.11}$$

In our research, we calculate the PV $\boldsymbol{q}$ between every two σ_θ layers instead of interpolated z layers to maintain the original model dynamics following the model structure. As there are no horizontal gradients of density along a single isopycnal, the $\partial \rho/\partial x$ and $\partial \rho/\partial y$ terms are zero. Therefore, we obtain PV $\boldsymbol{q}$ on 8 intermediate σ_θ layers via the simplified equation 2.11.

2.4 Characteristics Analysis

Dimension reduction is a common way to simplify complex processes for characteristics analysis. We use Empirical Orthogonal Function (EOF) and Principal Component Analysis (PCA) methods as the traditional methods to capture their prominent features and generate the initial vectors for further Self-organizing Map (SOM) analysis.

2.4.1 Empirical Orthogonal Function/Principal Component Analysis

EOF and PCA analyses are performed using the Singular Value Decomposition (SVD) method based on the Python NumPy package (Harris et al., 2020) instead of calculating the eigenvectors and eigenvalues of the covariance matrix $\boldsymbol{C}$ (Thomson and Emery, 2014). The major difference

between the EOF and PCA applied in this research is that the spatial grids in EOF are replaced by multiple variables in PCA. For example, the spatial patterns and corresponded time series of the stream function $\boldsymbol{\psi}$ is calculated via equation 2.12.

$$\psi(s,t) \overset{\text{SVD}}{=} U \cdot S \cdot V^T \tag{2.12}$$

In equation 2.12, the stream function $\boldsymbol{\psi}$ is selected at a specific depth/layer and reorganized sequentially along longitude and latitude as dimension s, and its other dimension t is time. The decomposed term U is the spatial vector for each mode of the input stream function $\boldsymbol{\psi}$, and $S \cdot V^T$ is the corresponding time series. In PCA analysis, the input matrix is replaced by the time series of multiple variables from different locations instead of the same variable at each grid point.

2.4.2 Self-organizing Map

The Self-organizing Map (SOM) is an unsupervised neural network technique to capture the prominent features and recognize the dominant patterns of the input data via projecting the high-dimensional input data onto a low dimensional space (e.g., two dimensions) while preserving its topology. Our SOM analysis is based on the Python MiniSom package (Vettigli, 2018) obtaining the weights of each neuron $\boldsymbol{w}$ shown in equation 2.13 (Liu et al., 2006), where t is the learning iteration times, η is the learning rate, $T_{i,J}$ is the topological neighborhood function of the winning neural J, and x is the input data vector.

$$w_i(t+1) = w_i(t) + \eta(t) \cdot T_{i,J}(t) \cdot [x(t) - w_i(t)] \tag{2.13}$$

The winning neural J is also called the Best Matching Unit (BMU), defined by the lateral distance between neurons as equation 2.14. When the distance $S_{x,i}$ between input data vector x and weight vector w_i (i is from 1 to I, I is the total number of neurons) reach the minimum value as equation 2.15, the index of i is chosen as the BMU index J.

$$S_{i,j} = ||w_i - w_j|| \tag{2.14}$$

$$S_{x,i} = ||x - w_i|| \rightarrow J = argmin_i||x - w_i|| \tag{2.15}$$

The learning rate η is a decay function defined by the decaying parameter τ_η and initial learning rate η_0 as equation 2.16.

$$\eta(t) = \eta_0 \cdot exp\bigg(- \frac{t}{\tau_\eta}\bigg) \tag{2.16}$$

The topological neighborhood function $T_{i,J}$ is defined as a Gaussian function depending on the lateral distance between the winning neuron and all other neurons ($S_{i,J}$) as equation 2.17, where $\sigma(t)$ is the neighborhood radius at the learning iteration time t. The neighborhood radius is depended on the distance decaying parameter τ_T and initial neighborhood radius σ_0 as equation 2.18.

$$T_{i,J}(t) = exp\bigg(- \frac{S_{i,J}^2}{2\sigma(t)^2}\bigg) \tag{2.17}$$

$$\sigma(t) = \sigma_0 \cdot exp\bigg(- \frac{t}{\tau_T}\bigg) \tag{2.18}$$

We use the sum of the first two PCA modes of the input data vector multiplied by a weighted parameter (from -1 to 1) as the initial weights of each neuron. For the iteration procedure, we use the sequential training process to pick up the input data vector along one input dimension (e.g., time or space). There are two different ways to get a trained SOM model of our Spatio-temporal data. The first way is to do the training iteration for each time stamp (input spatial series), and the second way is along the spatial dimension for each grid point (input time series). Therefore, the final weight vectors of temporally trained SOM (input spatial series) present the characteristic spatial patterns of the input data. Its BMU time series indicate the evolution of these patterns over time. The spatially trained SOM (input time series) can find the characteristics of the input time series, and its BMU for each grid point can be used to recognize each grid and group different regions (Liu et al., 2016).

In this research, all the SOM models are established with the same parameters as the followings.

The rectangular topology is used with a neighborhood radius σ_0 = 1, the initial learning rate η_0 = 0.5, and the learning iteration times t = 5000. The total number of neurons is defined by the map size of the rectangular topology $m \times n$, which is 3 $\times$ 3 and 4 $\times$ 4 in this research.

2.4.3 Variance-preserving Spectra

The estimated Power Spectral Density (PSD) in section 4.5 is based on the periodogram method from Thomson and Emery (2014). The variance-preserving spectra are estimated as Morey et al. (2020) to facilitate direct comparison and interpretation. The multiplication of frequencies revises the visual distortion of the transform from linear coordinate to exponential coordinate, and a 13-point smoothing is applied as in the previous study as well. Smoothing can increase the Degree of Freedom (DoF) by frequency band averaging to the $DoF \times FilterLength$ (Thomson and Emery, 2014), which is 26 for the confidence intervals in this research. Instead of subsampling after frequency band averaging, the original resolution is kept in this research to keep the variance-preserving spectra smooth.

3. LOOP CURRENT SYSTEM IN NUMERICAL SIMULATIONS

3.1 Validation of the Free-run Simulation

The nine-year free-run simulation (from January 2010 to December 2018) presents a similar mean deep circulation system (top panel in Figure 3.1) as the observations from deep floats (Furey et al., 2018; Hamilton et al., 2018, 2019). The time-averaged LC area in the simulation is consistent with the satellite observations. The orange contour region in Figure 3.1 is the SSH large standard deviation region (> 25 cm), indicating the most dynamic region and major LC intrusion region. The regional averaged sea surface height anomaly (SSHA) index is calculated as the regional averaged SSHA in this LC intrusion region (orange contour region in Figure 3.1 top panel). The SSHA index indicates the higher frequency and more periodic LCEs shedding events in the simulation than the observation (bottom panel in Figure 3.1). Table 2.2 to Table 2.4 in section 2 also show more LCEs shedding events in the free-run simulation (6 times from 2010 to 2012) than in the SLAT and SLA simulations (4 times from 2010 to 2012) during the overlapping period.

In the SAIC observations, the LC reaches the 6°C isotherm at 800 m to 1200 m. Below this layer, the velocity profiles become more depth-independent, concentrating between 0 to 0.1 m/s with smaller standard deviations than the upper layer. Figure 3.2 shows the vertical extension of the time-averaged LC along the two selected sections of the free-run simulation (Figure 3.1). The LC is the primary feature in the upper ~1000 m, and the vertical profiles are quasi-barotropic below ~1000 m, which is consistent with the SAIC observations.

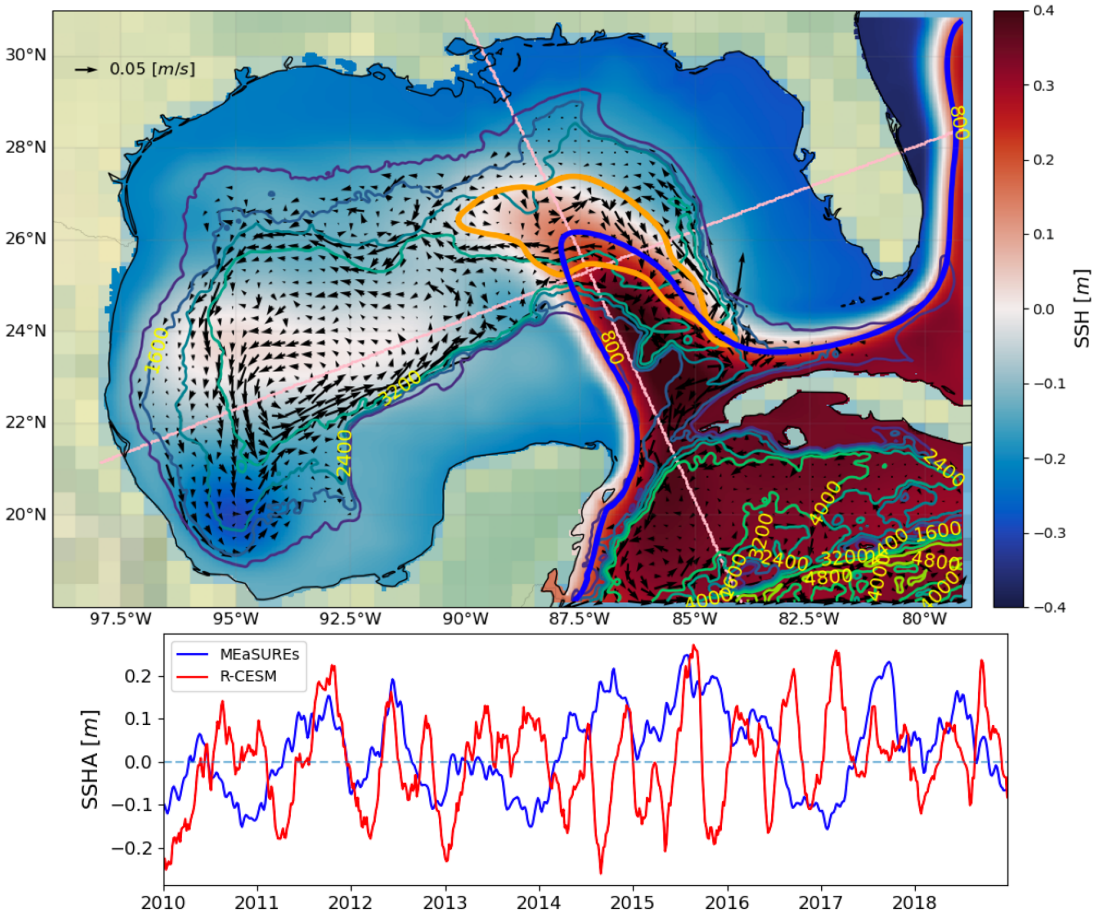

Figure 3.1: The top panel shows the mean spatial distributions of SSH (colors) and velocity (vectors) in the second bottom layer of R-CESM. The depth of the second bottom layer in the 3200 m region is approximately 200 m above the bottom. The contours with yellow numbers show the depth of the second bottom layer in different regions. The thick blue contour indicates the 17 cm SSH, which is the mean location of the LC during the whole period. The thick orange contour marks out the region that has the highest standard deviation of SSH, which is the selected region for the SSHA index in the bottom panel. The bottom panel shows the regional averaged SSHA from the Making Earth System Data Records for Use in Research Environments (MEaSUREs) data (blue line) and R-CESM data (red line). The regions are selected by their corresponding standard deviations of SSHA (larger than 0.2 m for MEaSUREs, larger than 0.25 m for R-CESM). The orthogonal pink lines indicate the along-LC section and across-LC section in Figure 3.2.

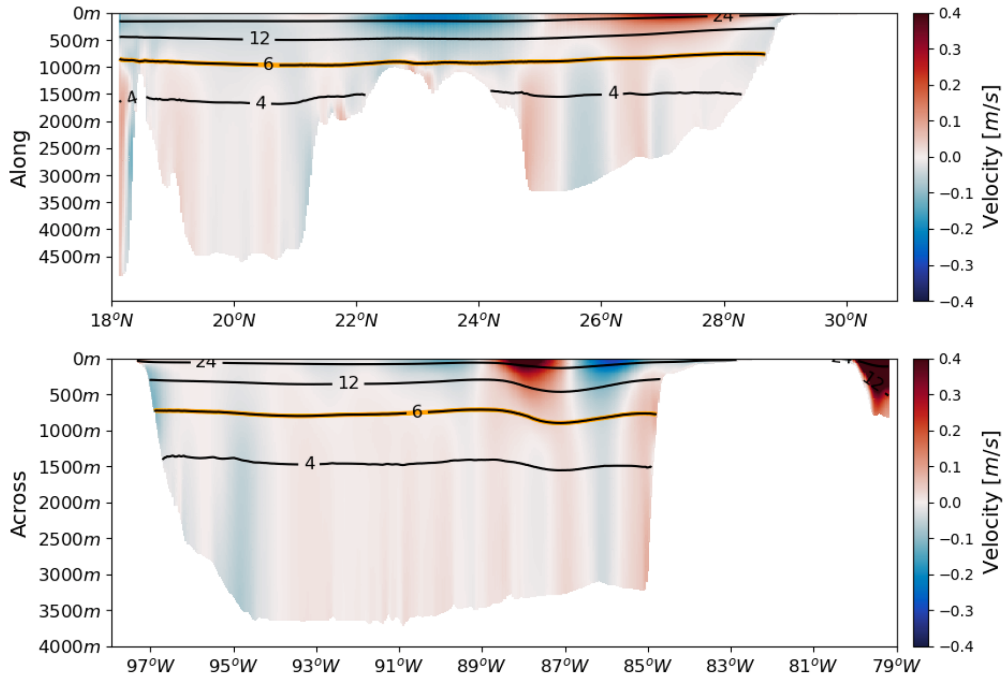

Figure 3.2: The sections along the LC (top panel) and across the LC (bottom panel). The colors show the velocity across the sections (red is northward/eastward, blue is southward/westward). The orange contour shows the depth of the 6°C isotherm along the section, which indicates the depth of the thermocline and the bottom of the LC. The black contours present some isotherms in the unit of [°C].

In the histograms of speed of Figure 3.3, the σ-layer velocity outputs from R-CESM are interpolated into the SAIC current meter locations, except the 100 meters above the bottom (mab) is replaced as 200 mab due to the rough vertical resolution in the R-CESM approaching the bottom. It shows the R-CESM velocity at 600 m is more concentrated in the high values range than the SAIC velocity, but the R-CESM lower-layer velocity is more concentrated in the low values range. The simulation has a more energetic upper layer but a less energetic lower layer.

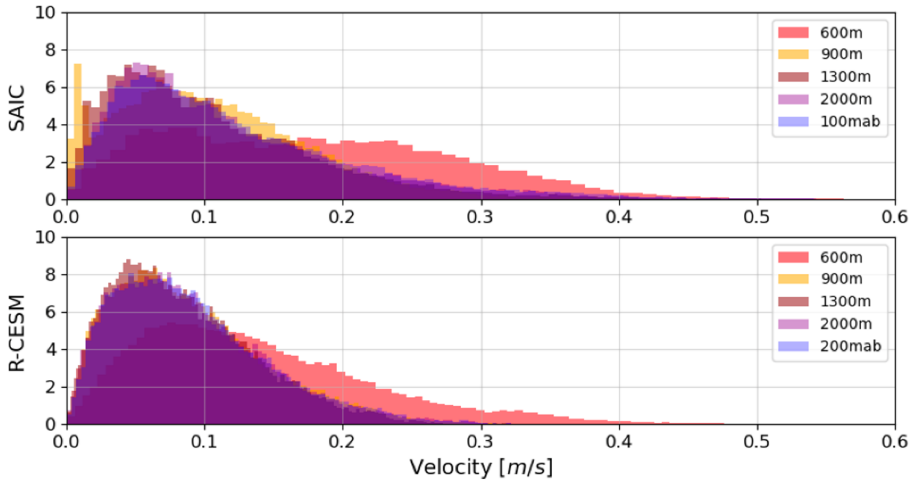

Figure 3.3: The histogram of the spatial averaged velocities at the locations of the SAIC moorings from SAIC observations (top panel) and R-CESM free-run outputs(bottom panel). Different colors indicate different depths.

The temperature and salinity data from the free-run simulation are interpolated to the SAIC moorings to check the model temperature-salinity (TS) structure as Figure 3.4. Figure 3.5 presents all the temperature and salinity data from SAIC moorings with their errors as a comparison. Since there are only four salinity sensors on the SAIC arrays, we cannot get a TS diagram from SAIC mooring observations. Their temperature structures are in a similar range, from 15 °C to 30 °C at the surface layer and from 4 °C to 7 °C at the bottom of thermocline (~1000 m). The high subsurface salinity core (Portela et al., 2018) at ~22 °C is reconstructed in the R-CESM simulation, and the lower layer TS structure is also in the similar range as observations.

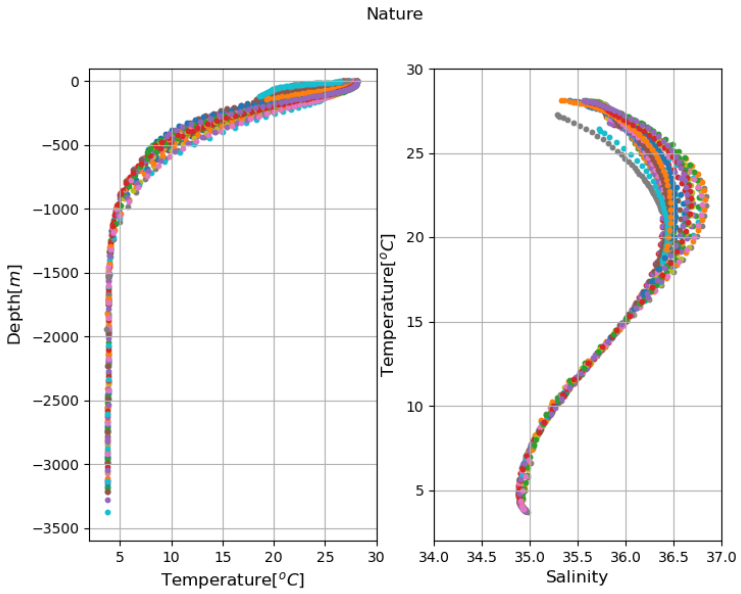

Figure 3.4: The temperature-depth profile (left panel) and temperature-salinity (TS) profile (right panel) of free-run simulation interpolated at all the SAIC mooring locations. Each color represents a unique mooring station.

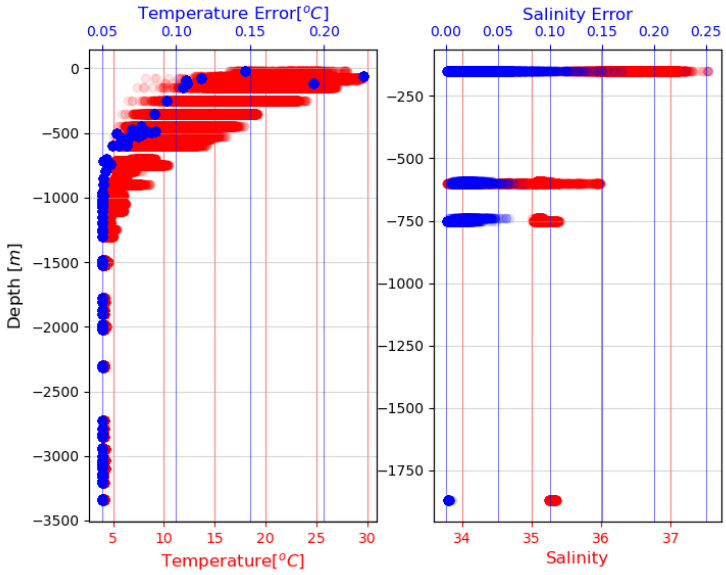

Figure 3.5: The temperature profile (left panel) and salinity profile (right panel) of all the SAIC moorings. The red color (bottom x-axis) presents the temperature or salinity data, and the blue color (top x-axis) presents the corresponding error defined as the temporally averaged standard deviation of every 12-hour interval.

Four mooring stations (A2, C2, N4, and Y6) from SAIC and CICESE arrays are selected to investigate the TS structure. A2 and C2 stations are SAIC tall moorings, showing the features at the west and east branches of the LC. N4 and Y6 stations are CICESE full-depth moorings, presenting the characteristics of the west branch of the LC close to the necking-down region and at the Yucatan Channel. The necking-down region is ~24 °N, where a pair of cyclonic features form a neck-like feature from both sides of the LC before the LCE separation. The distances between each two stations are larger than the first baroclinic Rossby radius of deformation in the GoM, which is about 40 to 50 km (Chelton et al., 1998).

Figures 3.6 to 3.9 are the potential temperature structure with the regression trend between each station and the interpolated R-CESM at each station (top panel), and the histogram of their potential temperature (bottom panel).

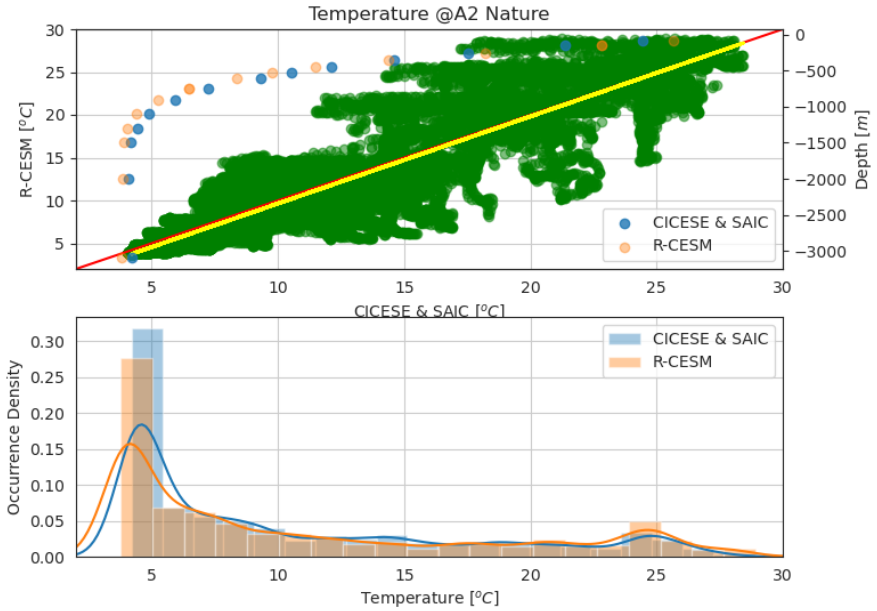

Figure 3.6: The top panel is the time-averaged potential temperature profile (x-axis is the temperature, the right y-axis is the depth) at station A2 of observation (blue) and interpolated free-run simulation (orange). The top panel also presents the regression relationship between potential temperature from observation and interpolated free-run simulation at all depths and times (green). The red line is the 45° line to be compared with the yellow regression line. The bottom panel shows the histogram of the same temperature data as the top panel from observation (blue) and simulation (orange).

Figures 3.6 and 3.7 present similar results for stations A2 and C2. The difference between the R-CESM and SAIC temperature profiles varies in depth. The R-CESM simulated mooring stations have a warmer (~0.5 °C) upper ~ 400 m and a cooler (~0.2 °C) lower layer. This warmer upper layer and cooler lower layer is consistent with the dynamical features, showing a more energetic upper layer and a less energetic lower layer, especially for the LC region. The shape of green dots and the corresponding up-tilted regression line is also as expected, the R-CESM simulated mooring stations have a cooler bottom layer and a warmer top layer than the SAIC observations.

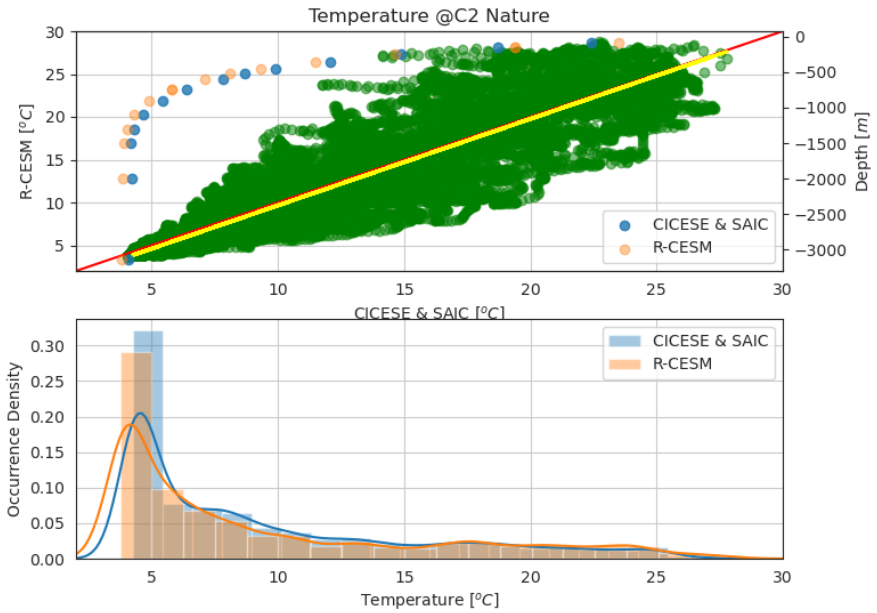

Figure 3.7: The top panel is the time-averaged potential temperature profile (x-axis is the temperature, the right y-axis is the depth) at station C2 of observation (blue) and interpolated free-run simulation (orange). The top panel also presents the regression relationship between potential temperature from observation and interpolated free-run simulation at all depths and times (green). The red line is the 45° line to be compared with the yellow regression line. The bottom panel shows the histogram of the same temperature data as the top panel from observation (blue) and simulation (orange).

The histograms of stations A2 and C2 present a similar distribution between the R-CESM simulated mooring stations and SAIC mooring stations, but the temperature range of the R-CESM simulated mooring stations has a larger range with a warmer surface and a cooler bottom. The high occurrence in the lowest temperature bar is due to the vertical distribution of temperature sensors.

As the observation data from CICESE arrays contain more data gaps than the SAIC arrays, the number of CICESE observation data points counted in the histogram of Figures 3.8 and 3.9 is less than in Figures 3.6 and 3.8 while the number of simulation data points is the same for the entire period. Therefore, the integrated number of occurrences is different between R-CESM simulation and CICESE observation.

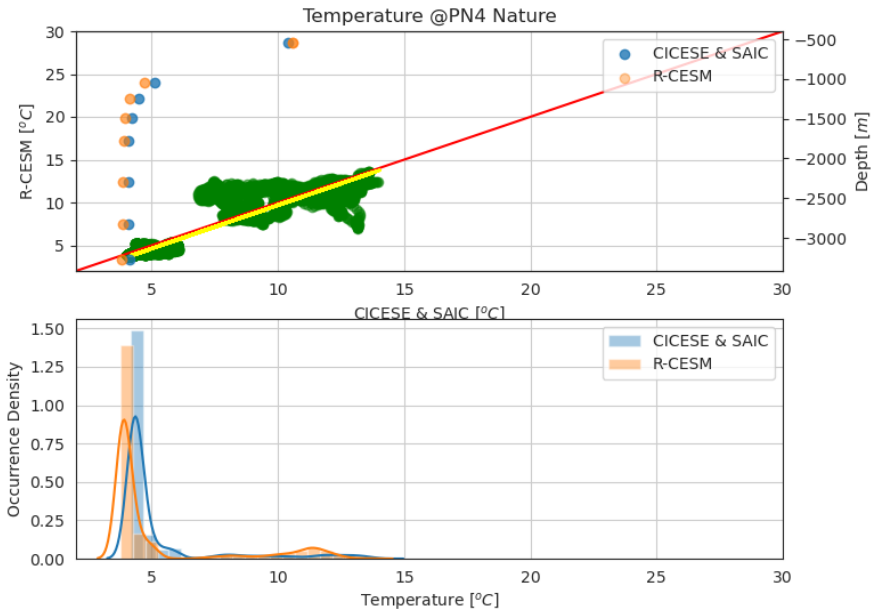

Figure 3.8: The top panel is the time-averaged potential temperature profile (x-axis is the temperature, the right y-axis is the depth) at station N4 of observation (blue) and interpolated free-run simulation (orange). The top panel also presents the regression relationship between potential temperature from observation and interpolated free-run simulation at all depths and times (green). The red line is the 45° line to be compared with the yellow regression line. The bottom panel shows the histogram of the same temperature data as the top panel from observation (blue) and simulation (orange).

Compare to stations A2 and C2, the potential temperature profiles of stations N4 and Y6 have smaller biases with changes in depth. Therefore, the regression yellow line of these CICESE stations is closer to the red 45° line than the previous SAIC stations. The shape of green dots still presents a warmer upper layer and a cooler lower layer in the R-CESM simulated mooring stations compared to the CICESE observations. Furthermore, station N4 shows a stronger bias than station Y6, this difference may be due to the shorter distance of station N4 to the LC major intrusion region.

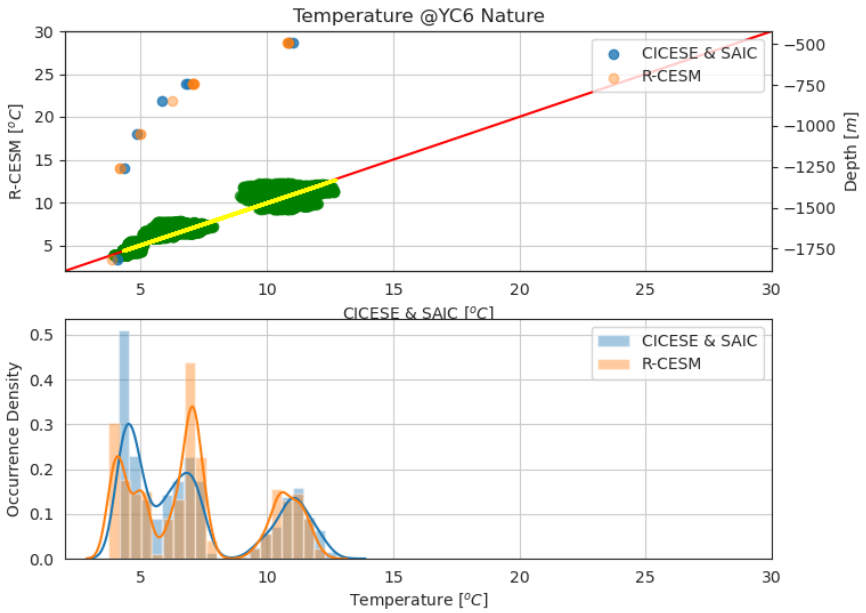

Figure 3.9: The top panel is the time-averaged potential temperature profile (x-axis is the temperature, the right y-axis is the depth) at station Y6 of observation (blue) and interpolated free-run simulation (orange). The top panel also presents the regression relationship between potential temperature from observation and interpolated free-run simulation at all depths and times (green). The red line is the 45° line to be compared with the yellow regression line. The bottom panel shows the histogram of the same temperature data as the top panel from observation (blue) and simulation (orange).

The peaks of occurrence density in the histograms of stations N4 and Y6 have similar distributions between the R-CESM simulation and CICESE observation. Both stations show a cooler bottom layer in the R-CESM simulation.

The power spectra are similar at all mooring stations after 40-hour low-passed filtering. The only selected station for checking the variance during the overlapping period between R-CESM and observations is station N4, as station N4 presents the signals around the LC necking-down region. Figure 3.10 shows the power spectra of lower layer velocities in R-CESM free-run simulation and station N4.

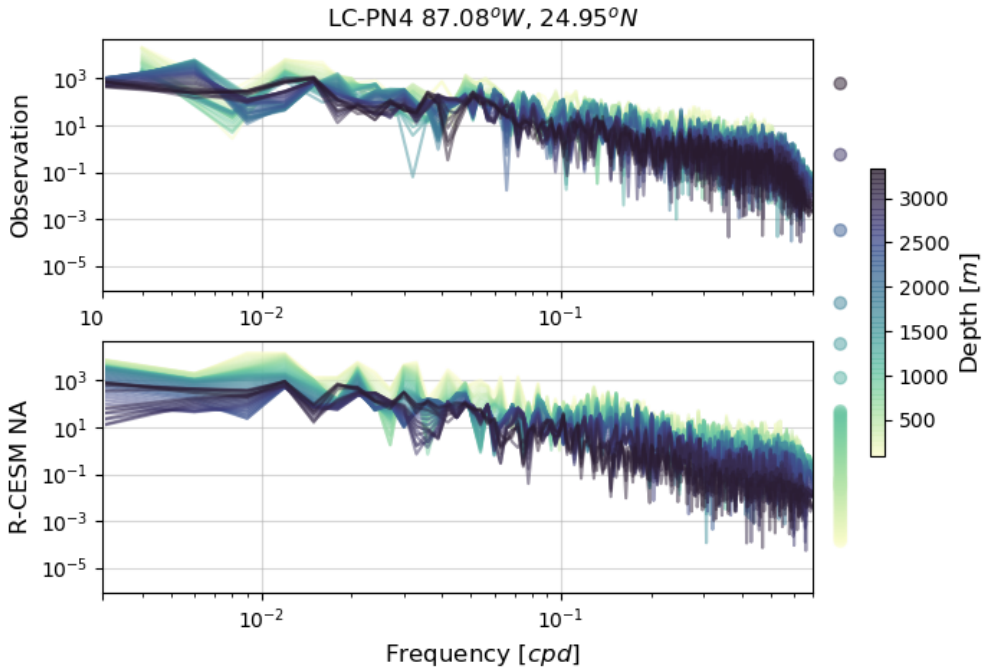

Figure 3.10: The top panel is the power spectra of velocity at multiple depths of CICEIE mooring station N4, and the bottom panel is the power spectra of velocity at interpolated depths of free-run R-CESM data at the same spatial spots. The depths are shown by the color bar, the vertical scatter plot presents the sampling distribution.

Figure 3.10 presents similar power spectra between observation and R-CESM at some depths in the subsurface. The most significant difference between R-CESM and observations is the vertical distribution of their power. Lower-layer power is more comparable to the upper-layer power in the observations than in the R-CESM simulations. In the R-CESM outputs, its power spectra present the feature of a strong vertical stratification, whose power decreases with depth shown as different layers. As the major frequency of the LCS is ~ 60 to 100 days, the model dynamics of R-CESM can be used in our research to study the low-frequency (> 40 hours) processes.

The lower-layer circulation related to the upper layer LCS is reconstructed by the R-CESM simulations. The dipoles of deep eddies are found in the free-run simulation as we expected (Furey et al., 2018) (Figure 3.11). The leading anticyclonic deep eddy indicates the direction of LCE propagation, and the trailing cyclonic deep eddy interacts with the upper-layer meander for necking

down the LC as LCE shedding events. Thus, the model dynamics of R-CESM has the capability to capture the major features of LCE detachments/reattachments in both upper and lower layers.

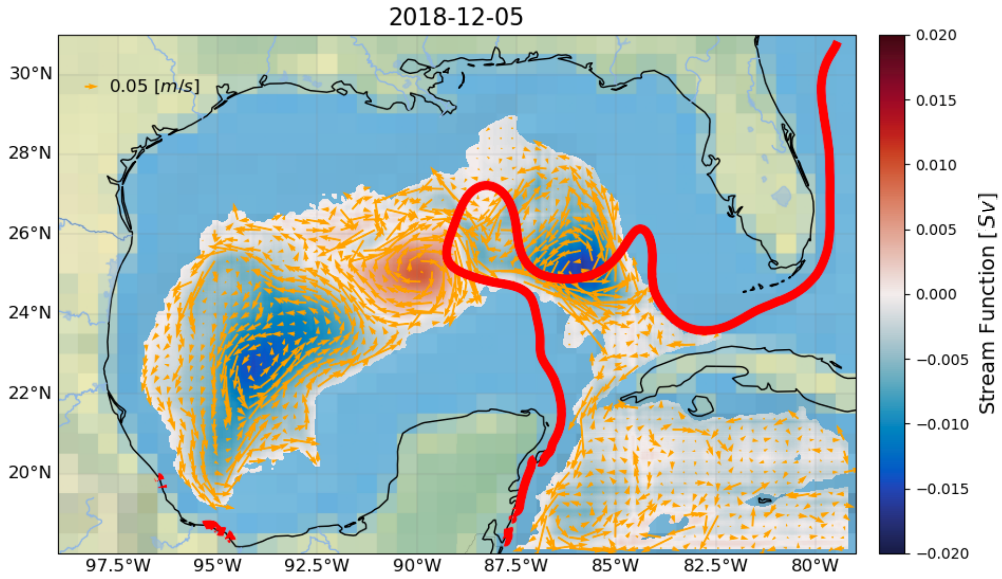

Figure 3.11: The spatial distributions of stream function in the second bottom (σ) layer of R-CESM on December 15th, 2018. The depth of the second bottom layer in the 3200 m region is approximately 200 m above the bottom. The orange vectors are velocity fields associated with the stream function. The thick red contour indicates the 17 cm SSH, which is the location of the LC on December 15th, 2018.

We speculate these biases of the LC may be induced by the inefficient downward propagation and conversion of EKE, which could keep more energy in the upper layer contributing to a higher occurrence of LC shedding events. These biases can cause more unrealistic numerical results in the NA run, which will be further discussed in section 4. Therefore, in subsequent runs, we need to improve the simulations using different observations to adjust the intensity of the LC. In general, the model dynamics of R-CESM can reconstruct the structure and characteristics of the LCS.

3.2 Loop Current Evolution

Because the free-run simulation presents the model dynamics defined by the physical equations without any constraints and is the longest output among three numerical simulations containing

nineteen LCE shedding events, the SOM model is trained with the free-run outputs to extract the dynamical processes of the LCS and to identify the principal patterns of variability associated with those processes.

Spatially trained nine-neuron SOM models and temporally trained sixteen-neuron SOM models are applied in this section, whose map sizes are 3×3 and 4×4 due to their expected number of features, respectively. The input SSH and stream function data are temporally and spatially resampled to 5 days, and 9 km after 40-hour low-pass filtering for computational efficiency and features conservation, and the primary parameters are the same as in section 2.4.2.

3.2.1 Sea Surface Height Evolution

The surface processes of the LCS are commonly described by the SSH. Therefore, the SSH data is used as the input vectors for the SOM models to extract the upper layer characteristics. In Figure 3.12, there are nine regions been sorted, showing the main axis of the LC and LCEs, and the peripheral regions. The grid points with the same color mean their SSH time series have similar temporal patterns. Hence, the main axis of the LC and propagating LCEs is shown as region 1, 3, and 4. Region 2 and 5 present the peripheral regions of the LC. Regions 6 to 9 are along the coastal slope surrounding the LCS, indicating the information of bathymetry. Region 2 is the most highlighted region as a small part of the peripheral regions. It is a joint of region 5 along the east branch of LC and connects to region 3, which is the main LC. Since the upper-layer LC meander of the east branch caused by the peripheral frontal cyclonic eddies and intensified via the baroclinic instability is along the eastern peripheral regions, region 2 is the initialization region of the LC meander. The peripheral frontal cyclonic eddies propagate along the LC from the Yucatan slope to region 2, and then these eddies keep accumulating and growing in region 2. Therefore, the primary features (Liu et al., 2006, 2016; Nickerson et al., 2022) of the LCS can be identified by the SOM model.

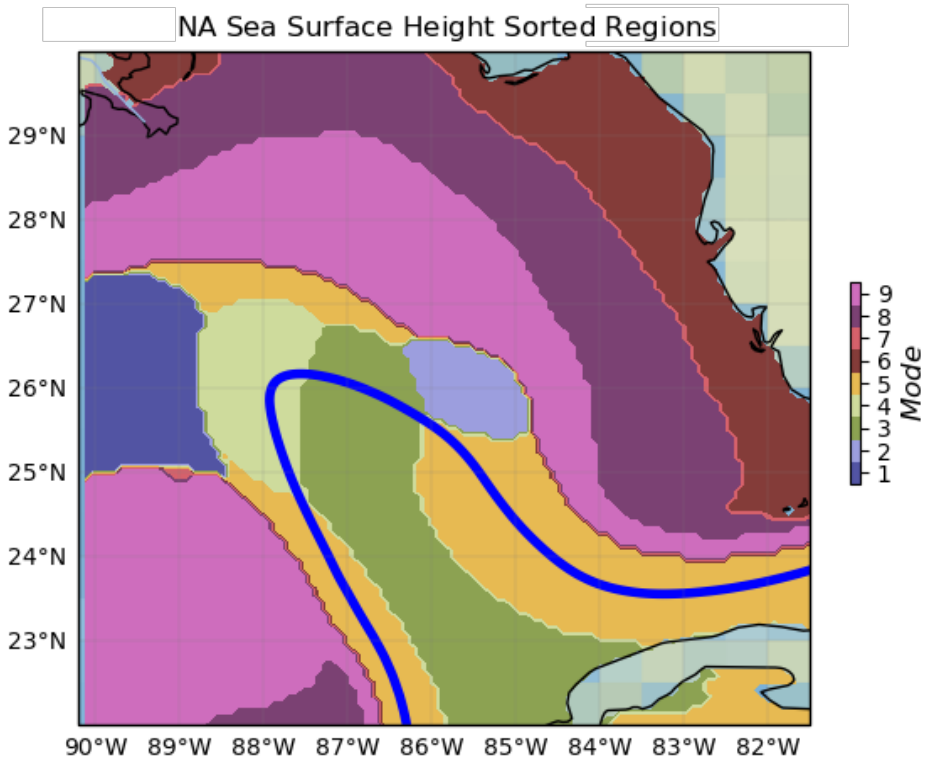

Figure 3.12: The sorted SSH regions are shown based on the spatially trained SOM of the free-run simulation. The shading color indicates different areas distinguished by the SSH time series at that grid point. The blue contour is the time-averaged 17 cm SSH line presenting the mean location of the LC.

This spatially trained SOM of SSH indicates the areas have similar temporal evolution, it can emphasize some unique regions, such as region 2, but the temporal evolution of SSH cannot be displayed. Hence, the temporally trained sixteen-neuron SOM model is used to extract the spatial patterns of SSH and group the time series by matching the closet spatial pattern at each time stamp. Combining the weighted vectors with the BMU, the temporal and spatial evolution of SSH could be revealed.

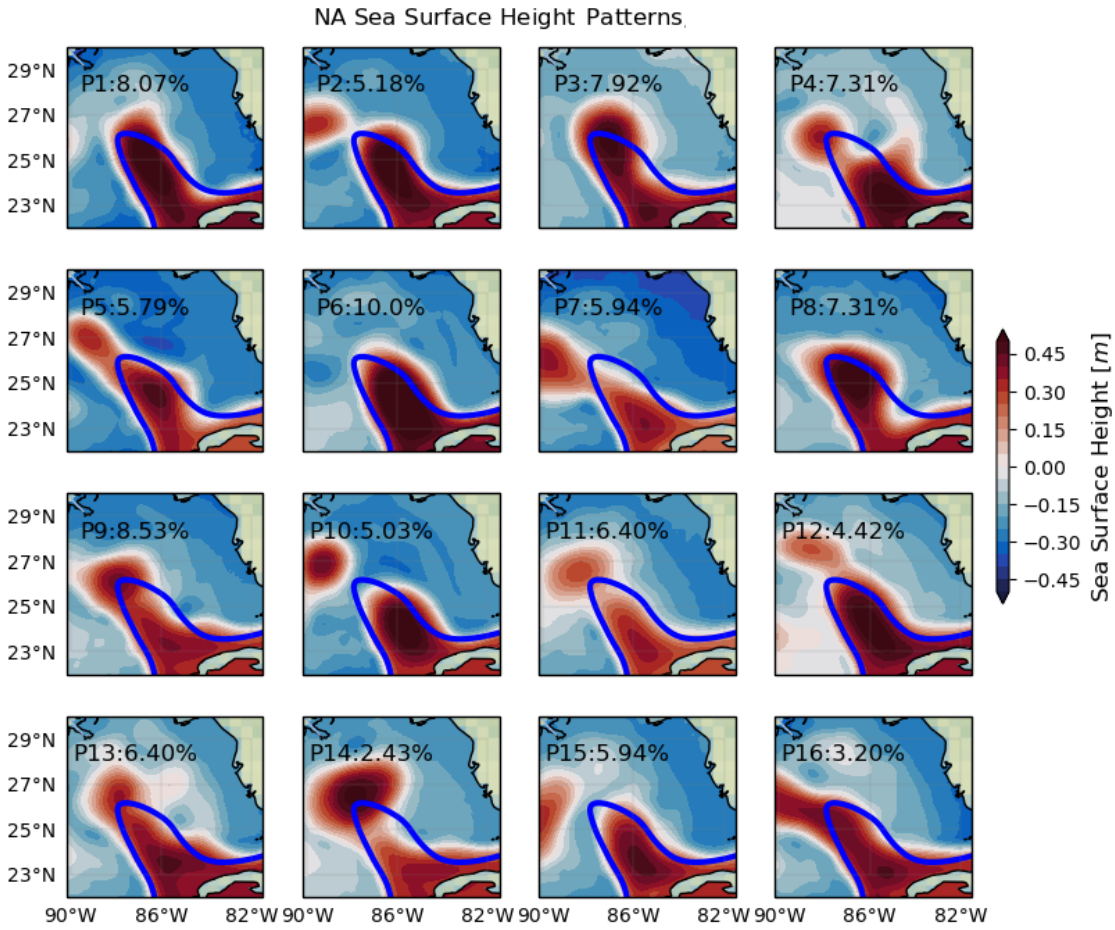

Figure 3.13: The sixteen panels present the SOM-captured primary spatial patterns of the SSH in the free-run simulation. The frequency of occurrence is shown as the subtitles of each pattern. The shading color indicates the SSH reconstructed from the SOM weighted vectors. The blue contour is the time-averaged 17 cm SSH line presenting the mean location of the LC, which is same in each panel.

The sixteen patterns are shown by the weighted vectors in Figure 3.13. The most outstanding feature that differs in different patterns is the state of the LCE. In patterns 1 and 6, the LCE is growing in the LC, which means the LCE is developing within the averaged LC location. These two patterns are identified as the intrusion of the LC before the separation occurs. The grown LCE

is about to separate from the LC in patterns 3, 8, and 14. The separated LCE is shown by patterns 2, 10, and 15. Other patterns present a connecting LCS, whose LCE is connected with the LC while the core of LCE is separated from the center of LC and weaker than the LC. There are different scenarios in the connecting LCS patterns, such as further penetration of the LC and reattachments of the LCE. Therefore, four groups of patterns can be distinguished as **Group I**: intrusion patterns (1 and 6), **Group II**: growing patterns (3, 8, and 14), **Group III**: detached patterns (2, 10, and 15), and **Group IV**: transit patterns (4, 5, 7, 9, 11, 12, 13, and 16). Since the LCS reaches its most considerable variability during the separation LCEs, most patterns could be seen among different separation events.

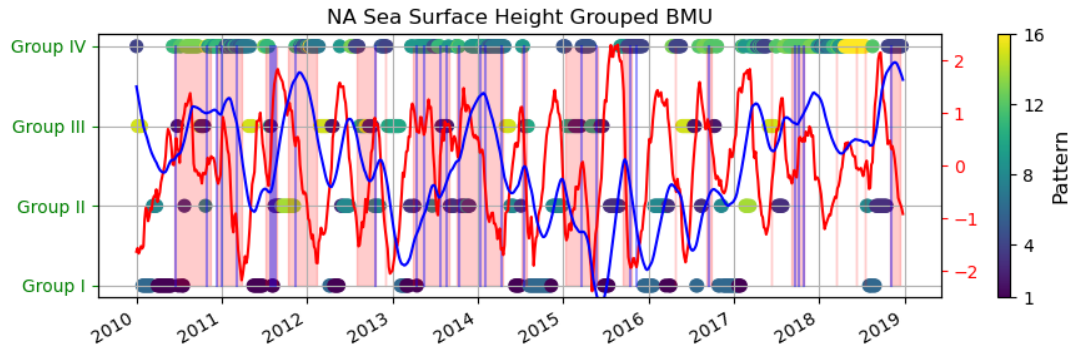

Figure 3.14: The colored dots show the grouped BMU of the SSH in the free-run simulation. The shading areas indicate all the LCEs shedding events from their first separation to their final separation, and the vertical blue lines present the reattachment occurring during each LCEs shedding event. The red line is the normalized SSHA index from the orange region in Figure 3.1, and the blue line shows the normalized accumulating SSHA index from the same region that has the maximum SSH standard deviation.

The BMU time series presents the most outstanding pattern at each time stamp, and the recognized patterns are the closest to the spatial distribution at that time. In Figure 3.14, the evolution of SSH spatial patterns in the free-run simulation is shown as the green dots. As the LCEs shedding events occur more frequent in the free-run simulation, the intervals between each events are temporally shorter than the observations and assimilative runs. The large uncertainty of LC position

during LCEs shedding events in the free-run simulation is also indicated by the normalized SSHA and cumulative SSHA indices. These indices could reach their extreme values several times during one separation event and have a big range of amplitudes during different events. Therefore, the detailed temporal and spatial evolution of LCEs shedding events will be discussed via the SLAT and SLA assimilative runs.

3.2.2 SLAT Simulation

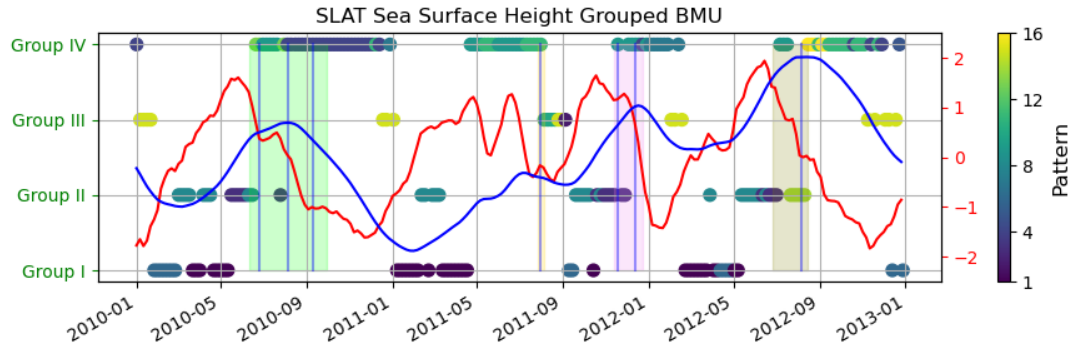

Figure 3.15: The colored dots show the grouped BMU of the SSH in the SLAT simulation. The shading areas indicate all the LCEs shedding events from their first separation to their final separation, and the vertical blue lines present the reattachment occurring during each LCEs shedding event. The red line is the normalized SSHA index from the orange region in Figure 3.1, and the blue line shows the normalized accumulating SSHA index from the same region that has the maximum SSH standard deviation.

The BMU of SLAT simulation is sorted by the same free-run trained SOM to extract the highlighted dynamical processes during the four LCEs shedding events in the three-year assimilative simulation. The snapshot of SSH during each event is shown in Figure 3.16 to indicate the actual position of each separation event.

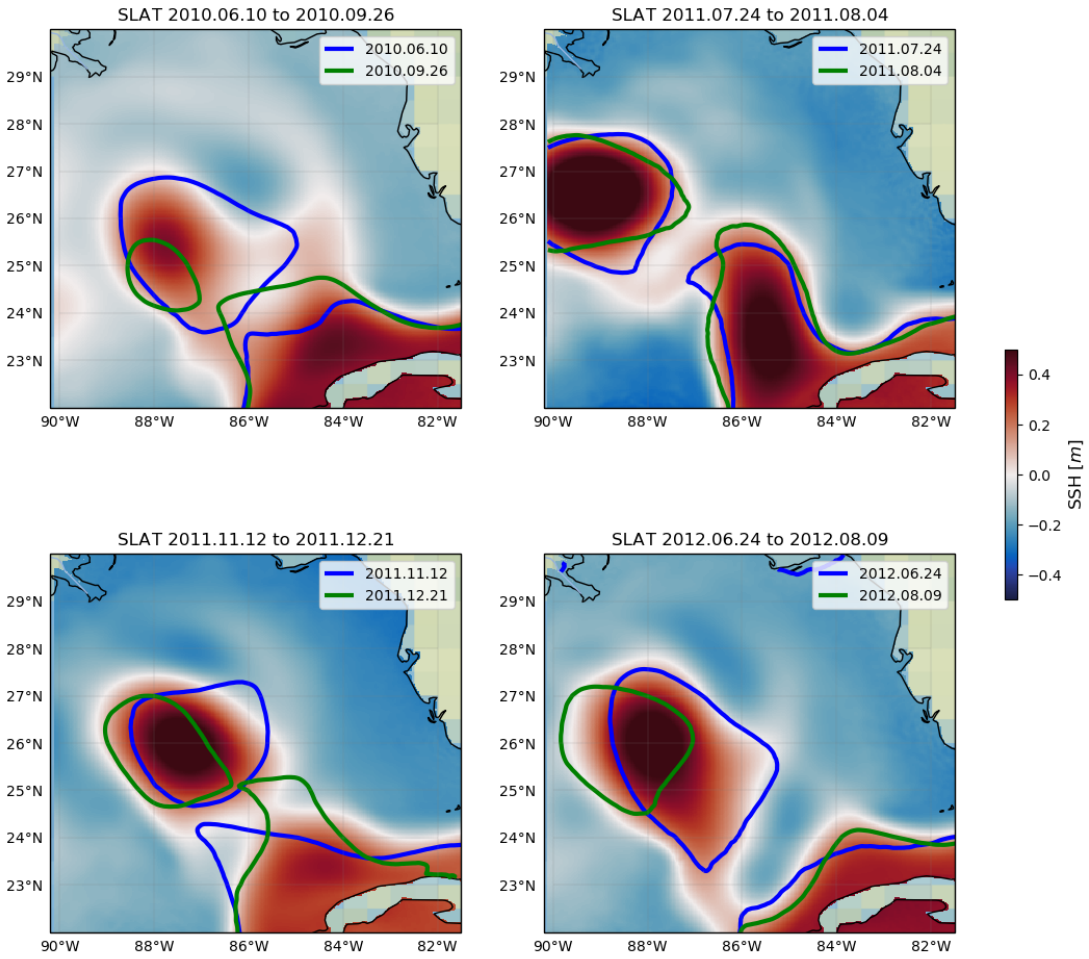

Figure 3.16: Four panels present the four LCEs shedding events in the SLAT simulation, the colors is the time averaged SSH from the first separation to the final separation, the blue contours show the 17 cm SSH at the date of first separation, and the green contours indicate the 17 cm SSH at the date of final separation

Combining the patterns from Figure 3.13 and the SLAT BMU time series from Figure 3.15, the major dynamical processes of the four LCEs shedding events could be described as the evolution of dominant patterns (Table 3.1).

LCE Event 1 is initialized as patterns 1, 3, 6, and 8 before the first separation. The LCS starts with a less penetrated LC and keeps intruding into the GoM with a growing LCE. Patterns 4, 9, and 13 are the leading patterns during the separation of the first event. They indicate a detached core of the LCE, while the edge of the LCE attaches to the LC several times. The first LCE shedding event ends with pattern 4, which has a blocked LC and detached LCE.

LCE Event 2 has a more extended LC than other events. The LC in the second event has a long penetration period shown as patterns 1, 8, and 9, which leads the LCS to intrude further north into the GoM. After growing for a longer time than in other cases, the separation of the second LCE is quick and with only one reattachment presented by patterns 10 and 11. Then, the LCS reaches to patterns 6 and 8 to penetrate into the GoM again for the third LCE shedding event.

LCE Event 3 is dominated by patterns 3 and 9. There are two reattachments during the third event. Therefore, the SSH spatial patterns present separated cores of the LC and LCE like the first event. Finally, the LCS reaches pattern 7, showing the westward propagating LCE.

LCE Event 4 is initialized by patterns 3 and 8 as the growth of the LCE in the LC. Then, patterns 9 and 14 stand out during the separation. Patterns 11 and 16 present a westward propagating LCE with a strong intruded LC after the current separation.

Table 3.1: LCE shedding events of the SLAT simulation, separation is defined by the separated 17 cm SSH contour, and associated SSH SOM patterns are from the Figure 3.13.

LCE Event	Event Name	Separation Start	Associated Patterns	Final Separation
1	Franklin	2010.06.10	1,3,4,6,8,9,13	2010.09.26
2	Hadal	2011.07.24	1,6,8,9,10,11	2011.08.04
3	Icarus	2011.11.12	3,7,9	2011.12.21
4	Jumbo	2012.06.24	3,8,9,11,14,16	2012.08.09

3.2.3 SLA Simulation

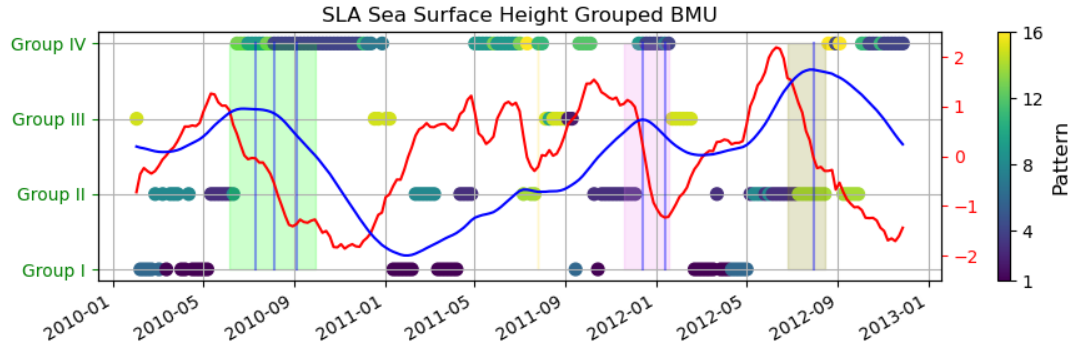

Figure 3.17: The colored dots show the grouped BMU of the SSH in the SLA simulation. The shading areas indicate all the LCEs shedding events from their first separation to their final separation, and the vertical blue lines present the reattachment occurring during each LCEs shedding event. The red line is the normalized SSHA index from the orange region in Figure 3.1, and the blue line shows the normalized accumulating SSHA index from the same region that has the maximum SSH standard deviation.

As the SLAT simulation and SLA simulation are assimilated with similar SSH data, the temporal and spatial surface evolution is similar in the two assimilative simulations. Figures 3.17 and 3.18 present the same contents as Figures 3.15 and 3.16 but in the SLA simulation. Compare Figures 3.16 and 3.18, the four LCEs shedding events in two assimilative simulations only present a few differences. These differences can lead to some differences between their BMU time series.

The second LCE shedding event is the most distinguishable difference between the surface evolution of SLAT and SLA simulations. In the SLAT simulation, the second LCE shedding event has one reattachment, and its BMU stays with patterns 9 to 11. In the SLA simulation, the second LCE shedding event has no reattachment, and its BMU varies among patterns 9 to 16. Figure 3.17 shows the BMU time series of the SSH in SLA simulation, similar to the SLAT simulation result in Figure 3.15. The SSHA and cumulative SSHA indices present a similar temporal evolution as well. The dominant spatial SOM pattern changes among patterns 13, 14, and 16 before the separation.

This could be the consequence of the further penetrated LC. The four LCEs shedding events in the SLA run is shown in Table 3.2.

Table 3.2: LCE shedding events of the SLA simulation, separation is defined by the separated 17 cm SSH contour, and associated SSH SOM patterns are from the Figure 3.13.

LCE Event	Event Name	Separation Start	Associated Patterns	Final Separation
1	Franklin	2010.06.05	1,3,4,8,9,13	2010.09.27
2	Hadal	2011.07.28	1,3,9,10,11,12,13,14,15,16	2011.07.28
3	Icarus	2011.11.19	3,4,7,9,15	2012.01.18
4	Jumbo	2012.06.24	3,4,8,11,14,16	2012.08.13

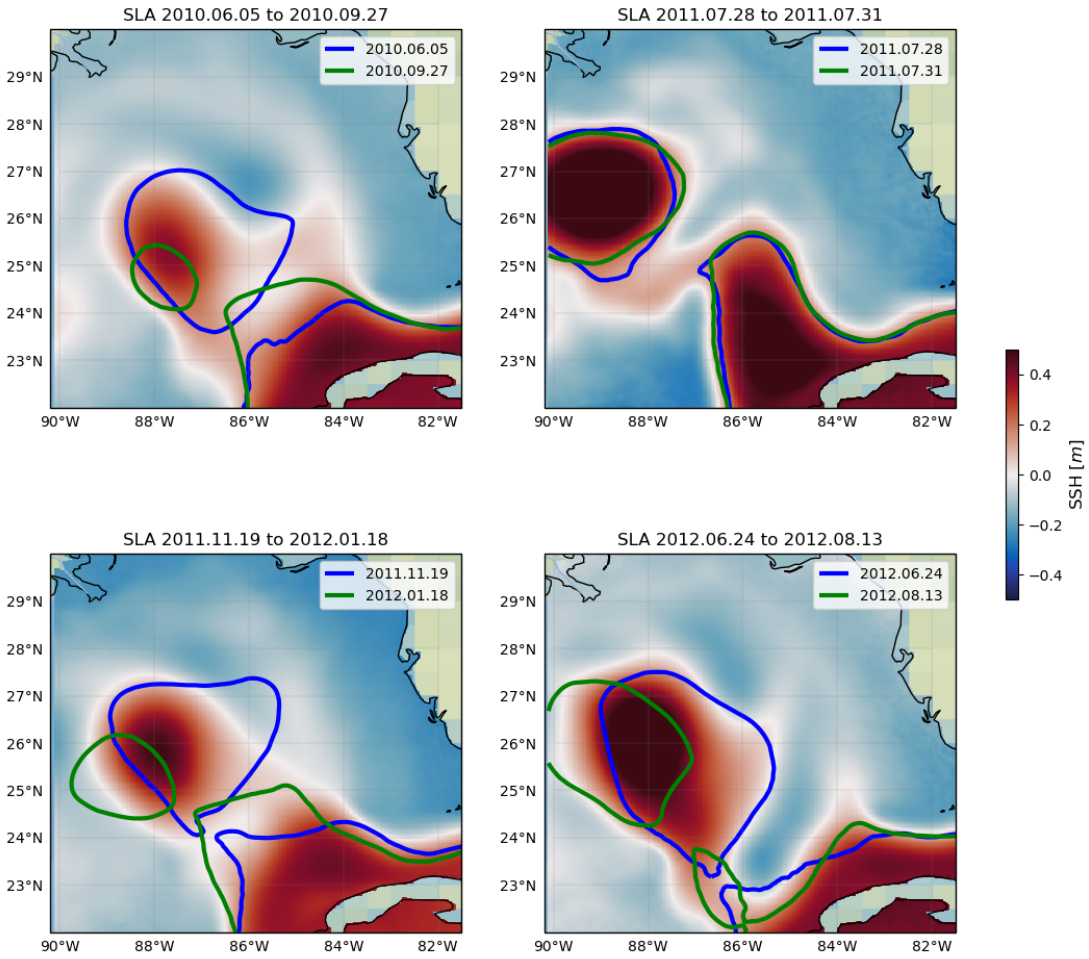

Figure 3.18: Four panels present the four LCEs shedding events in the SLA simulation, the colors is the time averaged SSH from the first separation to the final separation, the blue contours show the 17 cm SSH at the date of first separation, and the green contours indicate the 17 cm SSH at the date of final separation

3.2.4 Surface SOM Analysis

The SOM model is successfully established and tested with the SSH in NA, SLAT, and SLA simulations. It can be used to extract the dominant spatial features from the free-run simulation based on the model dynamics without any constraints. The spatial evolution of SSH can be distinguished into four groups of SOM spatial patterns as different states of LCS. Two similar BMU time series are obtained via applying the temporally trained SOM model to the two assimilative simulations. The SOM patterns in different groups highlighted by their BMU describe the four LCEs shedding events in two assimilative runs as their temporal evolution. Hence, the surface temporal and spatial evolution in the SLAT and SLA simulations are similar due to the constraining of satellite SSH data assimilation.

3.2.5 Deep Stream Function Evolution

The bottom layer of the LCS is commonly defined as the 6° isotherm. In this research, the 27.5 kg/m^3 σ_θ layer shown in Figure 2.3 is used as the bottom of the LCS, which is about 100 m deeper than the 6° isotherm. The vertical movement of the 27.5 kg/m^3 σ_θ layer is consistent with mooring observations during LCEs shedding events, being compressed by the penetrated LC. Therefore, the 27.5 kg/m^3 σ_θ layer is selected to identify the lower-layer features and avoid the variations from the upper-layer LCS.

As the SOM models are successfully tested with the SSH data, showing the capabilities of extracting the dominant features, the temporally trained sixteen-neuron SOM model is applied in this section. This SOM model is trained by the free-run stream function at the 27.5 kg/m^3 σ_θ layer, showing the geostrophic flow field at depth. The input stream function is temporally and spatially resampled to 5 days, and 9 km after 40-hour low-pass filtering, and the primary parameters are the same.

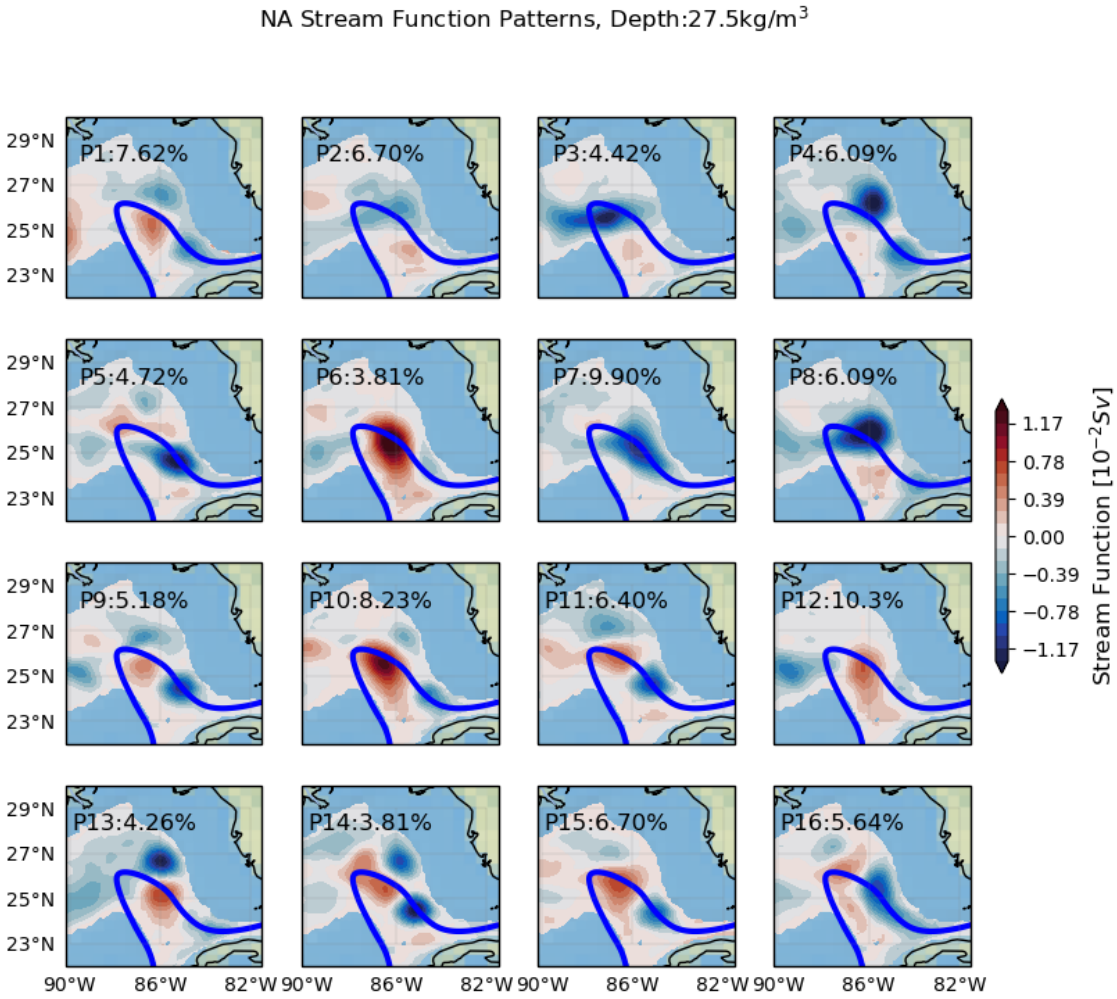

Figure 3.19: The sixteen panels present the SOM-captured primary spatial patterns of the stream function in the free-run simulation. The frequency of occurrence is shown as the subtitles of each pattern. The shading color indicates the stream function reconstructed from the SOM weighted vectors. The blue contour is the time-averaged 17 cm stream function line presenting the mean location of the LC.

The weighted vectors of the sixteen neurons are shown in Figure 3.19, indicating the different leading spatial patterns at the 27.5 kg/m^3 σ_θ layer. Based on the spatial distribution of the deep cyclonic (blue shades) eddies and deep anticyclonic (red shades) eddies, the spatial patterns can be generally sorted into four groups.

Group I is the penetration patterns: 6, 10, and 12, indicating the intrusion of the LC and the growth of the LCE. There is a strong deep anticyclonic eddy under the LC in these patterns, showing the presence of the penetration and growth.

Group II is the precursor patterns: 4, 5, 9, 14, and 16, presenting several deep cyclonic eddies surrounding the deep anticyclonic eddy. This group of patterns indicates the initialization and early break of the LCEs. The propagation of these deep cyclonic eddies will push the deep anticyclonic eddy further into the GoM, like the separation of LCE in the upper layer, such as pattern 4 to pattern 5.

Group III is the blocking patterns: 2, 3, 7, 8, and 13, which shows a blocking feature by connecting strong deep cyclonic eddies. These patterns should be seen both during LCEs separation and after LCEs separation because these blocking features could contribute to the LCEs separation by stopping the penetrating LC from reconnecting to the LCE. The retracted LC can also be blocked before the following intrusion.

Group IV is the transient patterns: 1, 11, and 15. These spatial features show another deep anticyclonic eddy in the west of the LCS with an equivalent intensity to the deep anticyclonic eddy below the LC region. A westward propagating LCE and a penetrating LC are identified by the fourth group of patterns. Therefore, patterns 1, 11, and 15 are the spatial patterns after the final separation of an LCE shedding event with the beginning of the following LC intrusion.

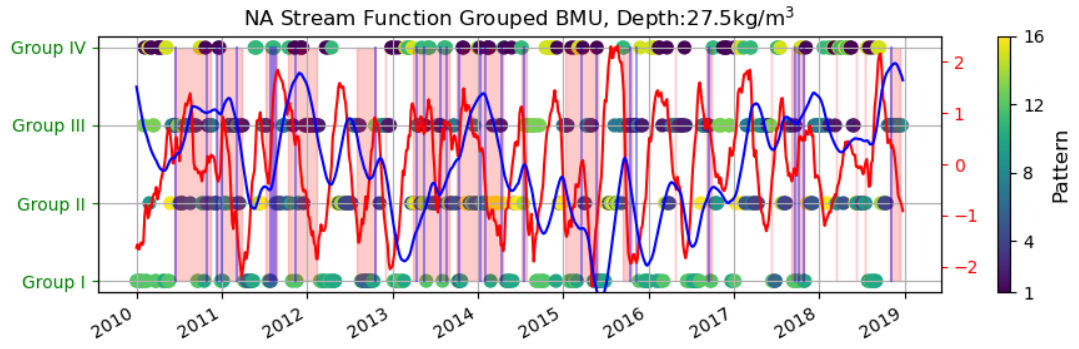

Figure 3.20: The colored dots show the grouped BMU of the stream function in the free-run simulation. The shading areas indicate all the LCEs shedding events from their first separation to their final separation, and the vertical blue lines present the reattachment occurring during each LCEs shedding event. The red line is the normalized SSHA index from the orange region in Figure 3.1, and the blue line shows the normalized accumulating SSHA index from the same region that has the maximum SSH standard deviation.

Similar to the BMU time series of the SSH results, the stream function BMU time series of the NA simulation in Figure 3.20 also changes among lots of different patterns due to the relatively shorter intervals between each LCEs shedding event. All the 16 patterns have stood out during some LCEs shedding events and concentrated on fewer patterns during the non-separation periods. This is the consequence of lacking the LC at this layer, whose most outstanding feature is not as distinguishable as the LC in the upper layer. Hence, the characteristics of non-separation periods are more capturable to the SOM model. The detailed LCEs shedding cases will be further discussed via the SLAT and SLA simulations and compared to the surface SSH results.

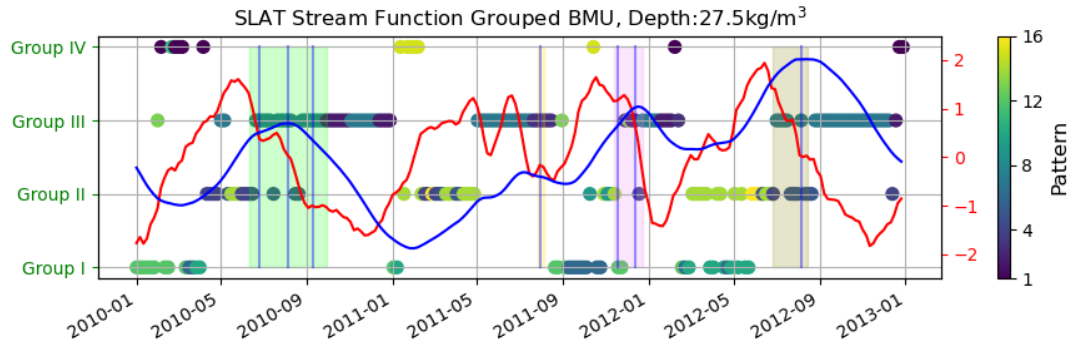

Figure 3.21: The colored dots show the grouped BMU of the stream function in the SLAT simulation. The shading areas indicate all the LCEs shedding events from their first separation to their final separation, and the vertical blue lines present the reattachment occurring during each LCEs shedding event. The red line is the normalized SSHA index from the orange region in Figure 3.1, and the blue line shows the normalized accumulating SSHA index from the same region that has the maximum SSH standard deviation.

The stream function BMU time series of the SLAT simulation is shown in Figure 3.21, and the corresponding normalized SSHA and cumulative SSHA indices indicate the temporal evolution of the LCEs shedding event on the ocean surface. Pattern 7 is highlighted during the first, third, and fourth LCEs shedding events, especially the end period. The second event is an outlier compared to the others, whose LC penetrates further north into the GoM before the separation begins, as seen in Figures 3.16 and 3.18. Before the second LCE separation occurs, pattern 7 becomes the dominant feature at the end of the long-last LC intrusion. As a pattern of the blocking pattern group, pattern 7 changes to and from patterns 2 and 3 during and after separations, these blocking patterns contribute to the separation processes and stop the following LC until patterns 10 and 12 for the subsequent LC penetration. Blocking pattern 8 does not occur in the SLAT simulation.

Patterns 4, 5, and 14 protrude at the beginning of the separations before the blocking patterns occur. They are the precursor patterns before the LCEs separate from the LC during the blocking patterns. Three deep cyclonic eddies initialize surrounding the strong deep anticyclonic eddy from the northeast corner, east necking down region, and the west to the LC region to transfer growing patterns into the blocking patterns.

In the SLAT simulation, the LCEs shedding events start from the growing patterns (**Group I**: 6, 10, and 12) to precursor patterns (**Group II**: 4, 5, 9, 14, and 16), then the blocking patterns (**Group III**: 2, 3, 7, 8, and 13) contribute to the LCEs separations. Patterns 1, 11, and 15 (**Group IV**) are the transient patterns, appearing relatively short time during the SLAT simulation. The associated patterns of the four LCEs shedding events in SLAT simulation are shown in Table 3.3.

Table 3.3: LCE shedding events of the SLAT simulation, separation is defined by the separated 17 cm SSH contour, and associated stream function SOM patterns are from the Figure 3.19.

LCE Event	Event Name	Separation Start	Associated Patterns	Final Separation
1	Franklin	2010.06.10	1,2,4,5,7,14	2010.09.26
2	Hadal	2011.07.24	3,4,5,7,12,13,14	2011.08.04
3	Icarus	2011.11.12	2,3,4,6,7,9,12,13,14,15	2011.12.21
4	Jumbo	2012.06.24	4,5,6,7,10,14,16	2012.08.09

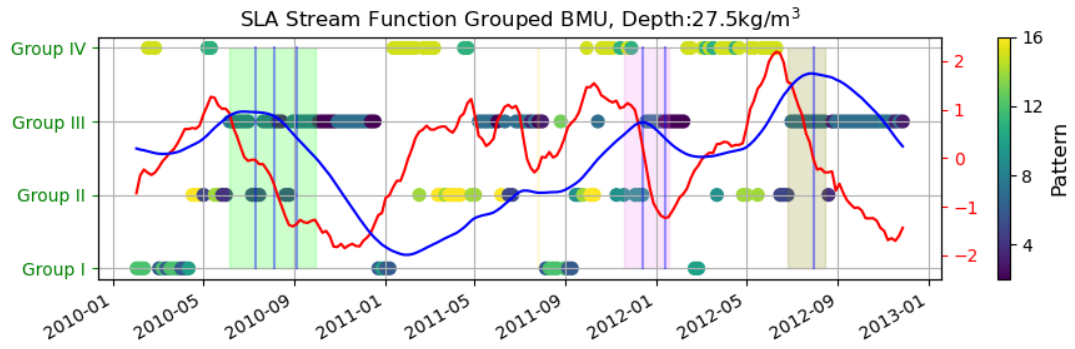

Figure 3.22: The colored dots show the grouped BMU of the stream function in the SLA simulation. The shading areas indicate all the LCEs shedding events from their first separation to their final separation, and the vertical blue lines present the reattachment occurring during each LCEs shedding event. The red line is the normalized SSHA index from the orange region in Figure 3.1, and the blue line shows the normalized accumulating SSHA index from the same region that has the maximum SSH standard deviation.

The temporal evolution of the SLA simulation is shown in Figure 3.22, and it indicates some

different dominant spatial patterns during the non-separation period compared to the SLAT simulation. The occurrence of pattern 15 increases significantly, which works like pattern 14 as a precursor pattern, but there is a weak anticyclonic anomaly in the west region in pattern 15. The occurrence of other patterns are similar to the SLAT simulation. The precursor patterns are the most critical part of our research to define the predictive metric of the LCEs separation. The associated patterns of the four LCEs shedding events in SLA simulation are shown in Table 3.4.

Table 3.4: LCE shedding events of the SLA simulation, separation is defined by the separated 17 cm SSH contour, and associated stream function SOM patterns are from the Figure 3.19.

LCE Event	Event Name	Separation Start	Associated Patterns	Final Separation
1	Franklin	2010.06.05	2,3,4,5,6,7,8,11,14	2010.09.27
2	Hadal	2011.07.28	2,3,5,6,7,8,9,12,13	2011.07.28
3	Icarus	2011.11.19	2,7,9,11,15	2012.01.18
4	Jumbo	2012.06.24	3,4,5,7,14,15	2012.08.13

3.2.6 Characteristics of Stream Function at Different Depths

The EOF analysis is applied to the stream function calculated via equation 2.9 based on the vertically interpolated velocity u and v to check whether the spatial patterns similar to the SOM spatial patterns can be extracted. Four z layers (300 m, 1000 m, 1500 m, and 3000 m) are selected from SLAT and SLA simulations to extract the highest correlated modes to the LCEs shedding events at each depth.

As the depth of the **LC velocity core** is in the upper 200 m, the 300 m z layer is selected to present the significant features of the LC, avoiding other near-surface variations. The 1000 m z layer is selected as the interface between the upper and lower layers, which is about the 27.5 kg/m^3 σ_θ layer in the LC region. Since the layers between 1000 m and 2000 m are ideal to present the lower layer characteristics and eliminate the impacts from bottom topography, the 1500 m z layer is selected. The 3000 m z layer is selected to show the variations in the bottom layer. All the data used in the EOF analysis are 5-day resampled after being 40-hour low-pass filtered by the

equations 2.1 and 2.2, including the u and v velocity.

The first five modes of stream function EOF analysis results at four selected depths are truncated in SLAT and SLA simulations, following the order of their contributions to the total variance. Contributions of each mode are shown in Figure 3.23. The sums of their contributions are all over 50% of their total variance for each depth individually. The selection of modes for describing the characteristics of the LCS related to the LCEs shedding events at different depths is based on the correlation between their principal component (PC) time series and the SSHA index in SLAT and SLA simulations. Therefore, only one mode is selected at each depth with the highest correlation coefficient between its PC time series and the SSHA index. All the selected modes at each depth in both SLAT and SLA simulations are shown in Table 3.5 and Figures 3.24 and 3.25.

Table 3.5: The selected EOF modes (shown in Figures 3.24 and 3.25) at different depths for SLAT and SLA simulations.

Depth	SLAT (Contribution)	SLAT r (95%CL)	SLA (Contribution)	SLA r (95%CL)
300 m	Mode 2 (17.3%)	-0.63 (0.52)	Mode 2 (12.67%)	-0.82 (0.79)
1000 m	Mode 3 (9.74%)	0.51 (0.37)	Mode 4 (6.92%)	-0.37 (0.36)
1500 m	Mode 4 (9.22%)	-0.44 (0.28)	Mode 3 (11.42%)	0.31 (0.28)
3000 m	Mode 2 (17.35%)	0.59 (0.4)	Mode 2 (15.17%)	0.43 (0.23)

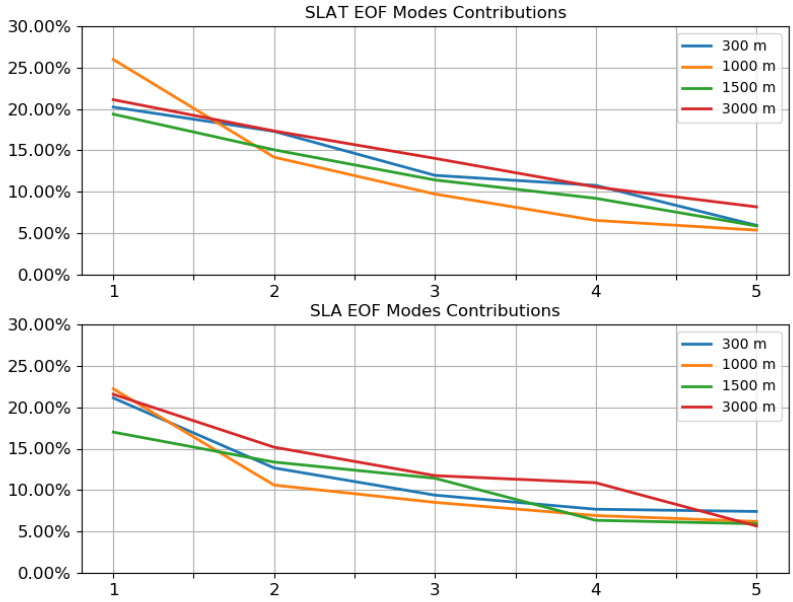

Figure 3.23: The contributions of the first five modes of EOF results at selected depths in SLAT (top panel) and SLA (bottom panel) simulations. The different colors present different depths, the four selected depths are 300 m (blue), 1000 m (orange), 1500 m (green), and 3000 m (red).

In the SLAT simulation, the four selected modes from four EOF analysis results of the normalized stream function at the four selected depths are shown in Figure 4.3. The 2nd mode at 300 m depth offers the highest correlation with the SSHA index among all the four selected modes because it has more upper-layer features close to the core depth of the LC. When the PC time series is negative, the spatial pattern shows a positive stream function anomaly covering the SSHA index region, indicating an anticyclonic circulation presenting the LC. Combining its spatial pattern with its PC time series, the increasing PC time series indicates a retracting LC in the spatial pattern, with a low stream function anomaly in the SSHA index region. Vice versa, the decreasing PC time series presents an intruding LC in its spatial pattern. It means this mode shows the features in the SSHA index region directly. Therefore, this mode has the highest correlation coefficient, and its PC time series is almost opposite to the SSHA index time series.

At 1000 m depth, the 3rd mode has the highest correlation with the SSHA index. Like the 2nd

mode at 300 m, the 3rd mode at 1000 m still shows a significant stream function anomaly area in the SSHA index region, which is opposite to the surrounding stream function anomaly. The difference in amplitude between the stream function anomaly in the SSHA index region and the surrounding opposite stream function anomaly becomes larger compared to the 300 m 2nd mode, as the LCS has a stronger impact on the 1000 m than the surrounding periphery frontal eddies or deep eddies. The core of the stream function anomaly on the east branch of the LC in the necking-down region is further into the LC (more western) than the 300 m 2nd mode. Since the 1000 m 3rd mode spatial pattern presents an opposite phase compared to the spatial pattern of 300 m 2nd mode, its PC time series also offers an opposite correlation coefficient with the SSHA index. Accordingly, the increasing PC time series indicates an intruding LC in the spatial pattern with a high stream function anomaly in the SSHA index region, which is opposite to the 300 m 2nd mode.

The 4th mode is the highest correlated mode at 1500 m depth to the SSHA index. The dipole of stream function anomaly is more significant in the 1500 m 4th mode spatial pattern than other selected modes. The center of the stream function anomaly is right on the east branch of the LC in the necking-down region, which is even further into the LC (more western) than the 1000 m 3rd mode. This stream function anomaly core is slightly more robust than the opposite stream function anomaly in the SSHA index region under the LC. This difference in the amplitude between these two dominant stream function anomalies indicates the one on the east branch of the LC has more contribution to the LCEs shedding events. The 1500 m 4th mode PC time series has similar phase changes as the 300 m 2nd mode PC time series. As the 1500 m 4th mode PC time series changes from negative to positive during all the four LCEs shedding events, there is a cyclonic stream function anomaly in the necking-down region covering most of the deep parts before the beginning of the separation of the LCEs. Hence, the 1500 m 4th mode contains the most variance of the deep eddies related to the LCEs shedding events.

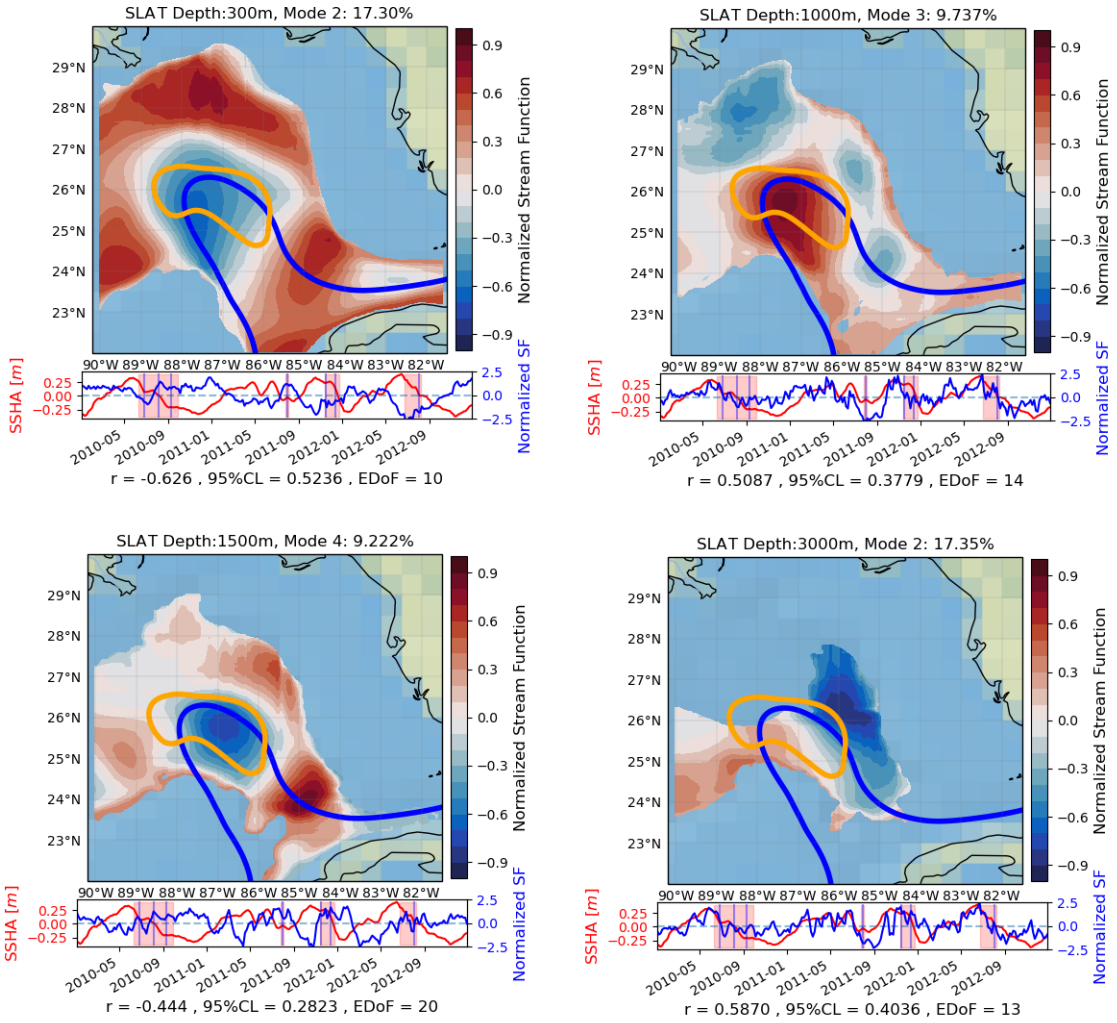

Figure 3.24: The four panels present four modes from four EOF analysis results of SLAT simulation at different depths shown in each title. These modes have the highest correlation coefficient between their PC time series and the SSHA index, their contributions are also shown in each title. For each panel, the top figures show the spatial pattern of the normalized stream function of each selected mode, the bottom figure presents the corresponding time series (blue line) and the SSHA index (red line). In the top figures, the blue contour is the time-averaged 17 cm SSH line indicating the mean location of the LC. The orange contour in the top figures circles the SSH large standard deviation region (> 27 cm), the averaged SSHA in this region is used as the SSHA index. The shading area in the bottom figures indicate all the LCEs shedding events from their first separation to their final separation, and the vertical blue lines present the reattachment occurring during each LCEs shedding event. The bottom labels show the correlation coefficients, EDoF, and corresponding 95% confidence level for each selected mode.

In the bottom layer at 3000 m, the 2nd mode has the highest correlation with the SSHA index.

This deep-layer mode still has a high correlation coefficient to the LCEs shedding events, which is the second-highest among all the selected modes. The primary spatial characteristics shown in the stream function spatial pattern at 3000 m is a deep cyclonic anomaly developed along the east branch of the LC, as the 3000 m 2nd mode PC time series has similar phase changes to the SSHA index.

Comparing the PC time series of all four selected modes at different depths in SLAT simulation (Figure 3.24), the highest correlated modes at 1000 m and 1500 m present the spatial patterns similar to the SOM precursor patterns. Therefore, the 1000 m and 1500 m layers in the SLAT simulation are the best candidates to establish a metric as a precursor of the LCEs shedding events.

The four selected modes in the SLA simulation (Figure 3.25) present some different characteristics than the SLAT simulation, but the EOF mode at 1500 m still offers a leading feature. In the upper layer, the 2nd mode at 300 m depth has the highest correlation with the SSHA index. The 300 m 2nd mode PC time series is highly correlated with the SSHA index and statistically significant. This mode shows the primary features of the LC intrusion and retraction, as it is in the upper layer dominated by the LC. The 300 m 2nd mode in the SLA run is similar to the SLAT run, combining its spatial pattern with its PC time series, the increasing PC time series indicates a retracting LC in the spatial pattern, with a low stream function anomaly in the SSHA index region, showing an LCE shedding event.

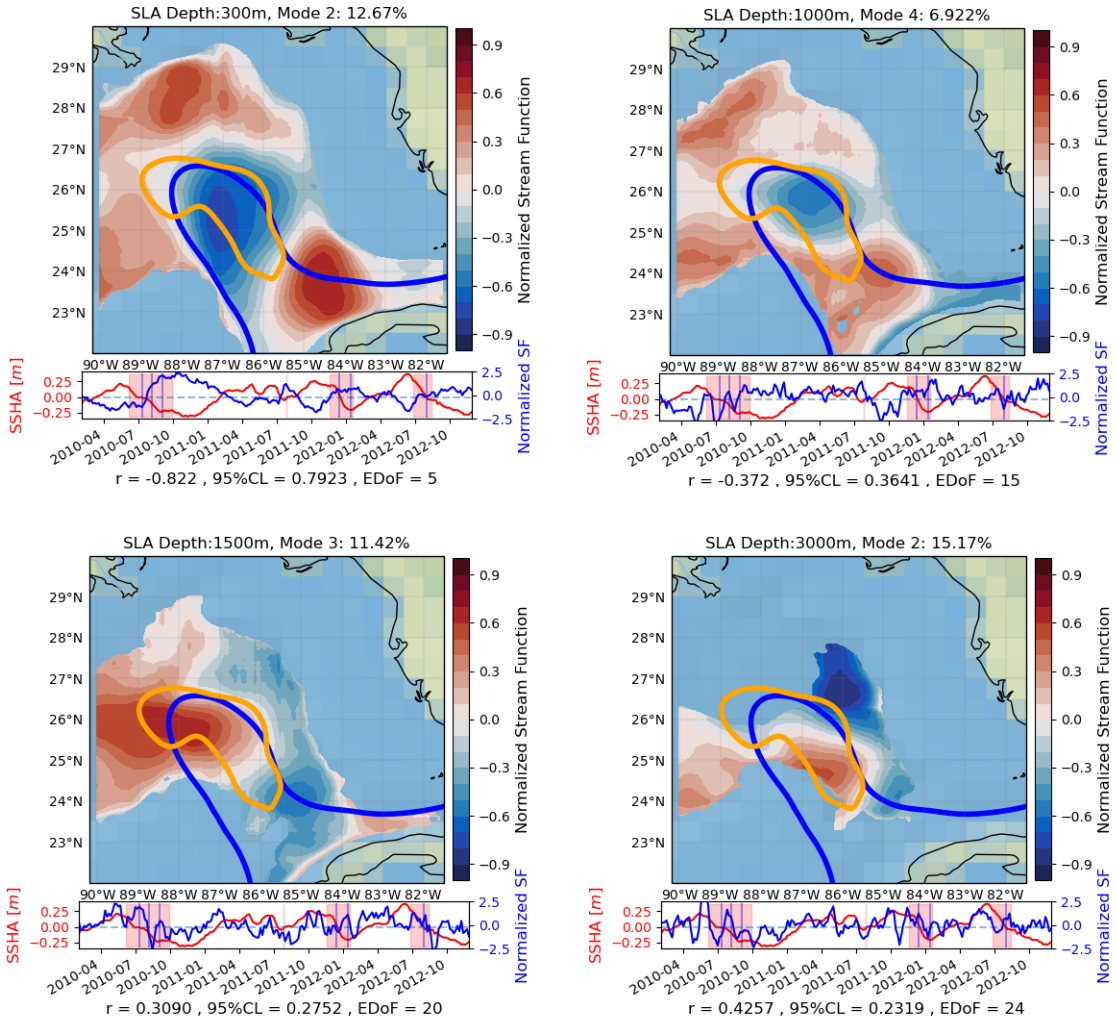

Figure 3.25: The four panels present four modes from four EOF analysis results of SLA simulation at different depths shown in each title. These modes have the highest correlation coefficient between their PC time series and the SSHA index, their contributions are also shown in each title. For each panel, the top figures show the spatial pattern of the normalized stream function of each selected mode, the bottom figure presents the corresponding time series (blue line) and the SSHA index (red line). In the top figures, the blue contour is the time-averaged 17 cm SSH line indicating the mean location of the LC. The orange contour in the top figures circles the SSH large standard deviation region (> 27 cm), the averaged SSHA in this region is used as the SSHA index. The shading area in the bottom figures indicate all the LCEs shedding events from their first separation to their final separation, and the vertical blue lines present the reattachment occurring during each LCEs shedding event. The bottom labels show the correlation coefficients, EDoF, and corresponding 95% confidence level for each selected mode.

The orders of modes at 1000 m and 1500 m vary between the SLAT run and the SLA run

because the contributions of modes 3 to 5 are similar to each other. Based on the highest correlation coefficients to the SSHA index, the selected modes in the SLA simulation are similar to those in the SLAT simulation. The 4th mode at 1000 m depth in SLA simulation shows a different spatial pattern compared to the 1000 m mode in SLAT simulation, but there is still a stream function anomaly dipole in the SLAT index region and the necking-down region. The 1000 m 4th mode PC time series presents some significant oscillations previous to the three longer LCEs shedding events, as the center of the stream function anomaly on the east branch of the LC covers the necking-down region like the 1500 m 4th mode in SLAT simulation. The stream function anomaly around the SSHA index region of 1000 m mode presents the upper-layer variance in the SLA simulation and lower-layer variance of deep eddies instead of the periphery frontal eddies in the SLAT simulation.

In the 1500 m layer, the 3rd mode offers the highest correlation to the SSHA index in the SLA simulation. It presents a similar spatial pattern to the SLAT run. The SLA 1500 m 3rd mode PC time series shows a leading phase to the SSHA index with a further intruded stream function anomaly on the east branch of the LC covering the necking-down region. Therefore, the 1500 m modes in both SLA and SLAT simulations show a deep cyclonic anomaly in the necking-down region before or during each LCE shedding event.

The 2nd mode at 3000 m depth has the highest correlation coefficient to the SSHA index. It shows second-highest among all the selected modes in the SLA simulation, which is similar to the SLAT simulation. Combining its spatial pattern and PC time series, it also indicates strong cyclonic stream function anomalies around the east branch of the LC before the three longer LCEs shedding events.

The four selected modes at different depths in SLA simulation (Figure 3.25) present a different result compared to the SLAT simulation. The 1000 m 4th mode and 1500 m 3rd mode are unlike the SOM precursor patterns as the SLAT EOF results. Therefore, the SOM precursor patterns can be identified as an orthogonal mode by the EOF analysis in the SLAT simulation. Still, in the SLA simulation, the distinguished modes have different spatial patterns.

3.3 Discussion

In section 3.1, the free-run R-CESM simulation presents a more energetic upper layer and a less energetic lower layer feature on both dynamics and thermal structure. The underestimation of parameters for downward energy propagation can be a reason for this situation. This impact intensity from surface variations differs between the SLAT and SLA simulations. The full-depth effect from the surface changes in the SLA simulation is much stronger shown in Figures 3.26 and 3.27. Figures 3.26 and 3.27 present the velocity profiles during the first LCE shedding event in SLAT simulation and SLA simulation.

In Figure 3.26, the velocity profiles are based on the SLAT simulation, whose assimilation depth is limited to ~2000 m. There is a significant interface between the upper ~2000 m and the lower layer. This interface can cut the water column into opposite directions between the upper and lower parts. This numerical feature appears after the first ~100 days of running, then the difference across the interface keeps growing to be stable at ~ 12 hours delay in the lower layer. It means the free-run lower layer in the SLAT simulation needs to take an extra ~ 12 hours to respond to the changes in the assimilated upper layer. This extra responding time can cause the slow down of the vertical propagation of energy in the R-CESM simulations. In the SLAT simulation, the upper ~2000 m layer is impacted by the surface assimilation simultaneously. Therefore, this vertical propagation lag in the free-run simulation could be more significant, which causes the more energetic upper layer and less energetic lower layer. As our analysis focuses on the low frequency (> 40 hours), this ~2000 m interface can be erased by the 40-hour low-pass filter.

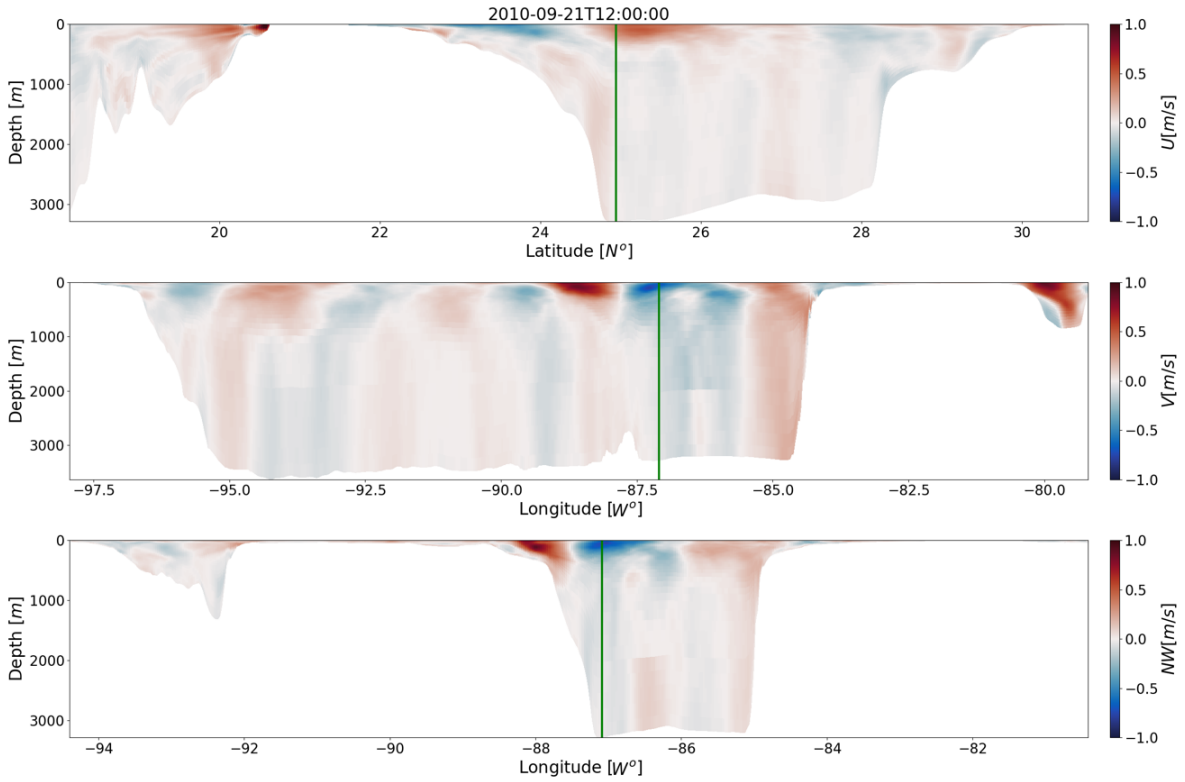

Figure 3.26: The three panels are the σ-layer velocity anomaly profiles across station N4 of the SLAT simulation at noon on September 21st, 2010. The top panel is the meridional section, the middle panel is the zonal section, and the bottom panel is the cross-shore section. The green vertical line indicates the location of station N4, the red color is the positive velocity (eastward, northward, and northwestward), and the blue color is the negative velocity (westward, southward, and southeastward).

Compared to the SLAT simulation, the impact of the LC on the lower-layer velocity in the SLA simulation is stronger, as shown in Figure 3.27. The lower layer velocity profile in the SLA simulation shows a more quasi-barotropic feature than the SLAT simulation, no matter whether the interface at ~2000 m is considered. The lower layer in the SLA simulation may be overestimated due to the full-depth impact of the ocean surface data assimilation.

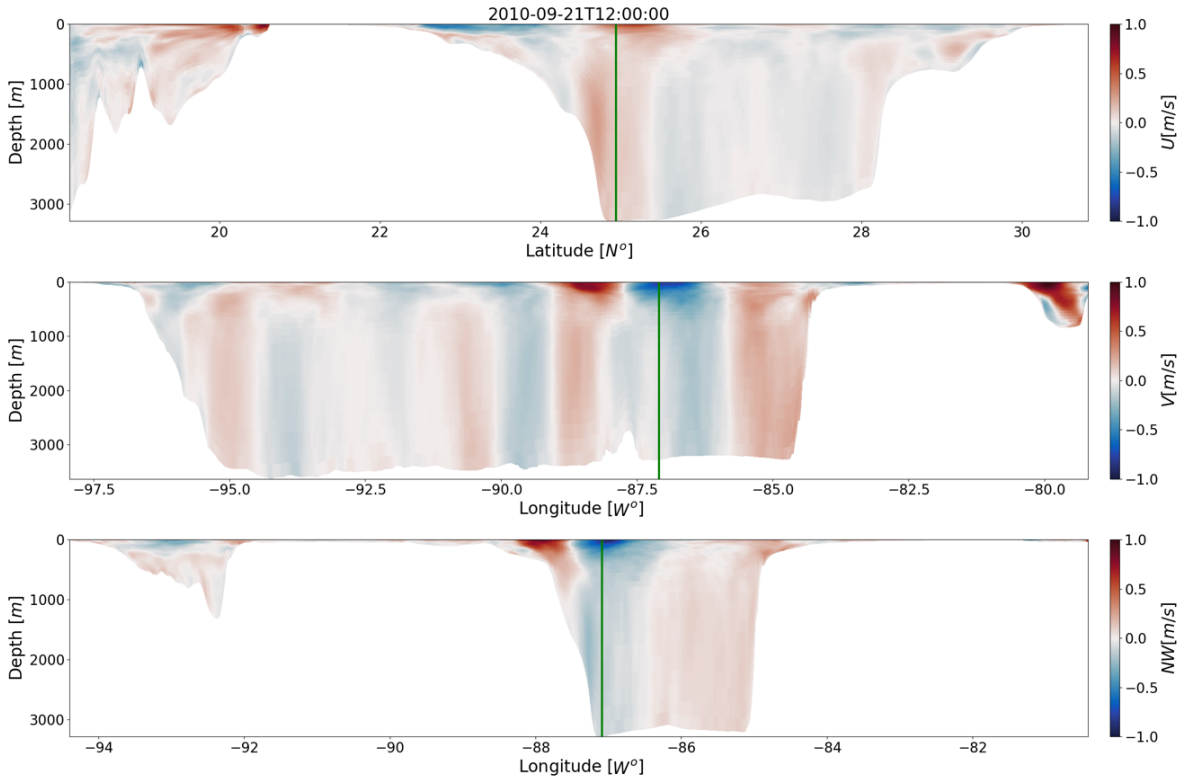

Figure 3.27: The three panels are the σ-layer velocity anomaly profiles across station N4 of the SLA simulation at noon on September 21st, 2010. The top panel is the meridional section, the middle panel is the zonal section, and the bottom panel is the cross-shore section. The green vertical line indicates the location of station N4, the red color is the positive velocity (eastward, northward, and northwestward), and the blue color is the negative velocity (westward, southward, and southeastward).

Without the data assimilation, the vertical propagation lag in the free-run simulation can result in some other unexpected LCS features, not only the higher separation frequency. There are some extreme LC intrusion events in the free-run simulation. The simulated LC can make an unexpected curve around the Yucatan Platform. Then, the LC will turn to reach the slope on the Texas Louisiana Shelf. Each state of LC movement can last for a few days.

The free-run simulation has an over-energetic LC, the SLAT simulation has an interface at ~2000 m cutting the model domain, and the impact of the LC in SLA simulation may be overestimated. Therefore, which numerical simulations are proper for the LCS dynamics studies should be further discussed.

The SOM is a useful tool to describe the temporal and spatial processes, but the mechanisms need to be further analyzed. Since the free-run simulation is model dynamics without any constraints, it will be used for extracting the dynamical relationships. Although the SLAT simulation has a separate bottom layer, the layers between 1000 m and 2000 m are still valuable to check the dynamics under the LC. As the ~ 2000 m interface in the SLAT simulation is erased after being 40-hour low-pass filtered, both the SLAT and SLA simulations have a quasi-barotropic lower layer under the LC.

4. LOOP CURRENT INDICATOR METRIC

This chapter compares the assimilative runs with the in-situ observations and free-run simulation, including the dynamical and thermal structure. Then, wavelet analysis is performed to capture the variability in different frequency bands. The indicator metric is established via the weighted parameters from the PCA analysis. The detail of the high-frequency variability revealed by the wavelet analysis is described as the Mixed Rossby-Gravity (MRG) wave in this dissertation. A more detailed dynamical examination of this mysterious wave trains features should be taken in the future works.

4.1 Improvements from Data Assimilation

Velocity profiles from mooring observation are used to check the improvements of the simulated dynamics after data assimilation, and temperature and salinity data reconstructed from PIES are used to check the thermal structure of the assimilated runs below 100 m. The assimilated dataset is the SSHA and SST data on the ocean surface. The significant improvement is the temporal and spatial evolution of LCEs compared to the free-run simulation. As the ocean is constrained by surface assimilation, the evolution of SSHA in SLAT simulation is similar to the satellite observation. Therefore, the frequency of LCEs shedding events is also constrained.

4.1.1 Dynamical Structure

The simulation of the LCS dynamics improved significantly in the upper 1500 m, comparing the vector correlations among the three different runs. Figure 4.1 is the vector correlation for the three simulations. By definition, r_{vc}^2 equal to 2 is the perfect correlation for two vectors. The upper-layer vector correlations between R-CESM simulations and observations are significantly improved by data assimilation. In the upper ~ 1000 m, the SLA run shows a higher correlation with the observations than the SLAT run. The low-layer vector correlations are improved as well compared to the free-run result.

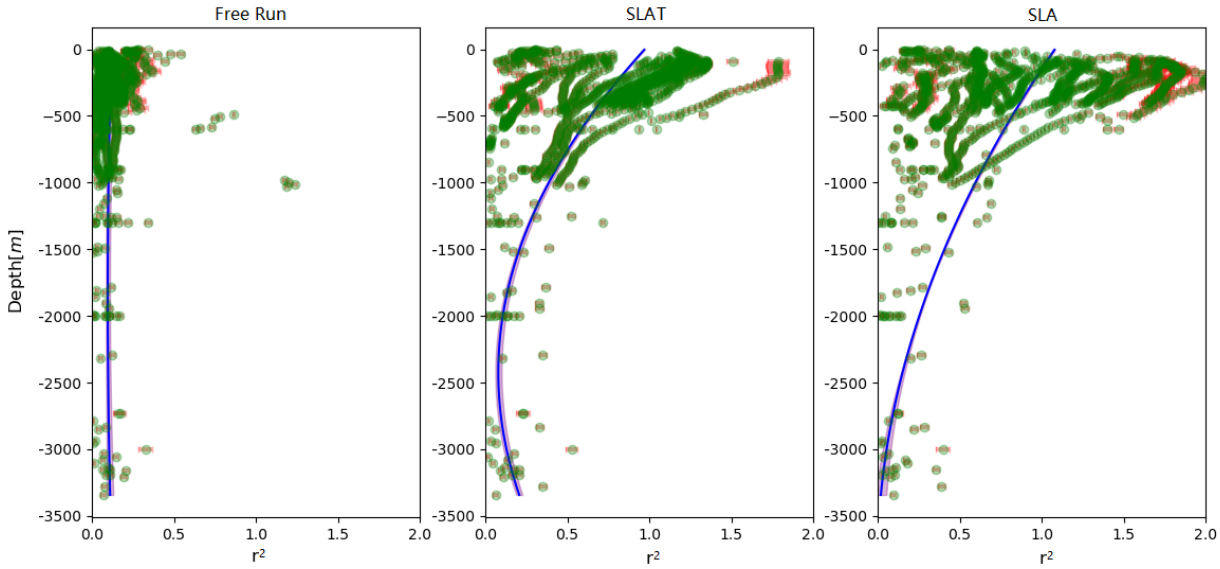

Figure 4.1: The three panels are the vector correlation coefficient r_{vc}^2 at all current meter locations for free-run simulation (left panel), SLAT simulation (middle panel), and SLA simulation (right panel). The green dots indicate the r_{vc}^2 (x-axis) of each sensor at different depths (y-axis). The red error bar is the corresponding error for each r_{vc}^2. The blue line is the fitted function of r_{vc}^2 varying on depth, and the purple shading is the corresponding error range.

The u and v velocity at the free-run simulation validation stations (A2, C2, N4, and Y6) are selected to check the improvements of data assimilation at the upper and lower layer interface depth. Figures 4.2 and 4.3 show the histograms of the u velocity, v velocity, speed at those four stations. All the data in the histogram are interpolated to the spatial point of the observations and temporally subsampled to the same sample frequency (6 hours). At station A2 (Figure 4.2), the distribution of velocities in SLAT simulation is closest to the observations, and the SLA simulation has the most bias. The v velocity in the SLA simulation has some extremely large values compared to other data.

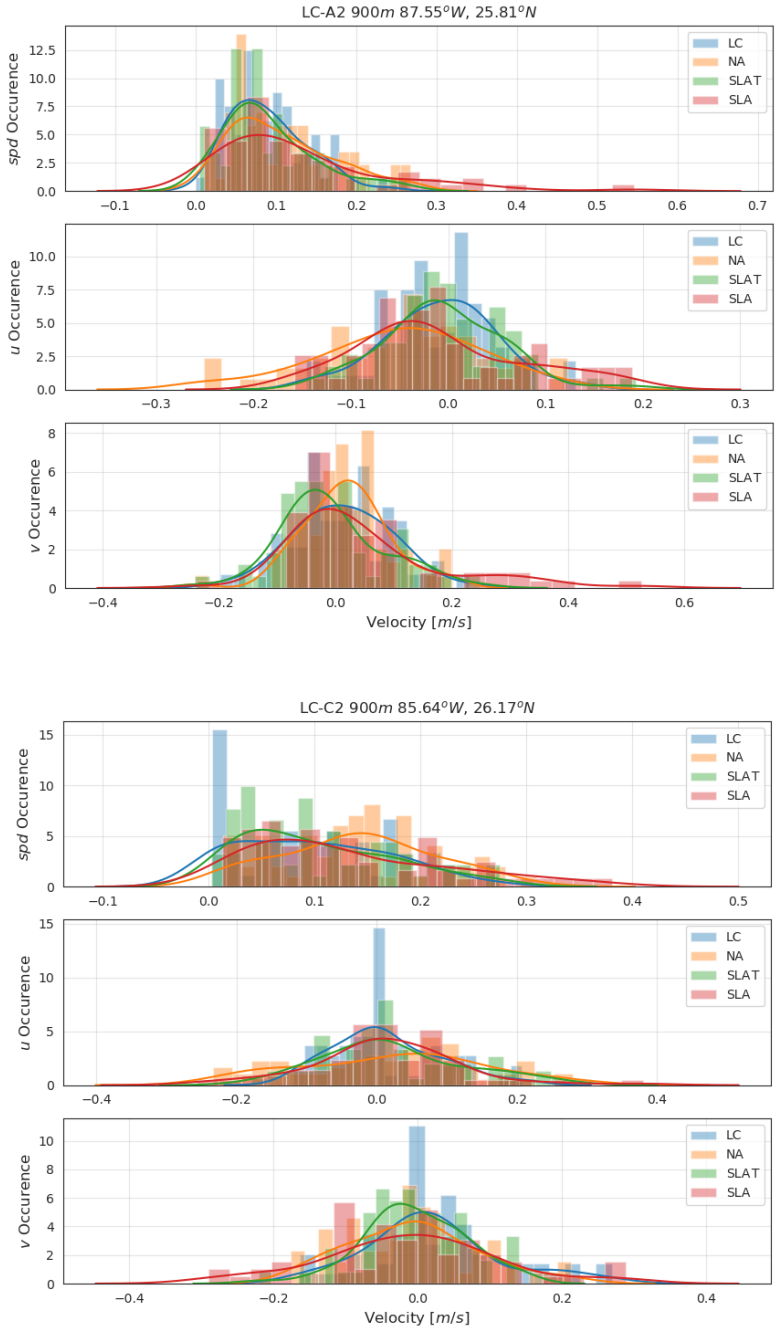

Figure 4.2: The speed histogram (top panel), u velocity histogram (middle panel), and v velocity histogram (bottom panel) at 900 m depth of SAIC stations A2 (top three panels) and C2 (bottom three panels). The station information is in the subtitles. Each color represents a different dataset, blue is the mooring observation, orange is the NA simulation, green is the SLAT simulation, and red is the SLA simulation.

In Figure 4.2 bottom three panels, the NA simulation shows the most different distributions from the observations. The mean speed of the NA run is larger than others due to the bias in the u velocity. As station A2, the SLAT simulation is the most similar to the observations at station C2.

At the CICESE mooring N4 (Figure 4.3), the NA simulation shows a significant bias in v velocity, and the SLAT and SLA simulations have a bias in the u velocity. Still, the SLAT simulation presents the closest distribution to the observations with an offset. In the Yucatan Channel, compared to the observation at station Y6, the NA simulation is too quiescent, and the SLA simulation is too energetic.

Since all the stations have a similar conclusion, the SLAT simulation reconstructs the best dynamics around the interface between the upper and lower layers.

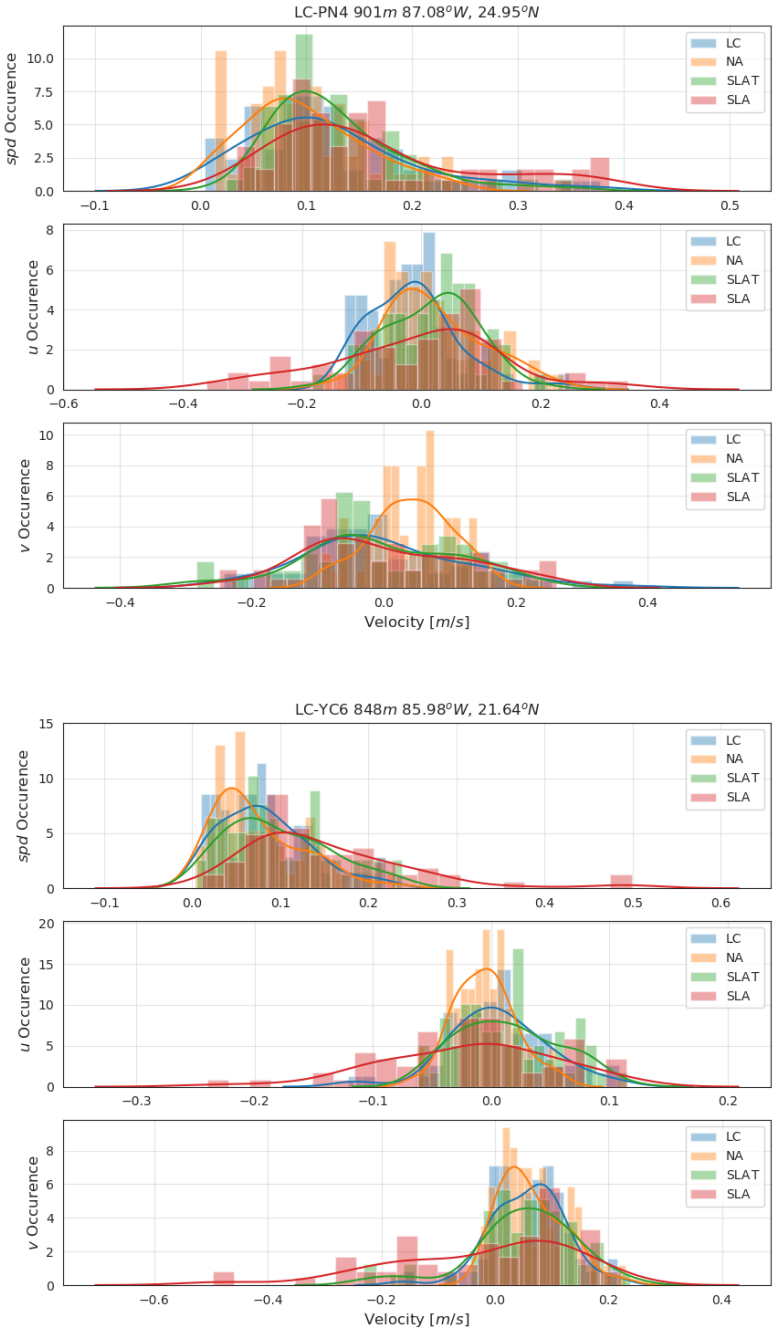

Figure 4.3: The speed histogram (top panel), u velocity histogram (middle panel), and v velocity histogram (bottom panel) at 901 m and 848 m depth of CICESE stations N4 (top three panels) and Y6 (bottom three panels). The station information is in the subtitles. Each color represents a different dataset, blue is the mooring observation, orange is the NA simulation, green is the SLAT simulation, and red is the SLA simulation.

4.1.2 Thermal Structure

The LCS TS structures of assimilated R-CESM simulations are not improved as the LCS dynamics. The TS structures show a warmer surface and a cooler bottom is stronger in the assimilative runs as Figures 4.4 and 4.5. The TS structure of the SLAT run is similar to the free-run simulation, but the SLA run has a significant bias in the upper ~ 500 m temperature. This bias may be due to the lacking of constraint from SST assimilation compared to the SLAT run. The assimilation of SSHA can adjust the LCS dynamics but induce some unexpected biases in the TS structure. These biases can be partially revised by the assimilation of SST following the model dynamics.

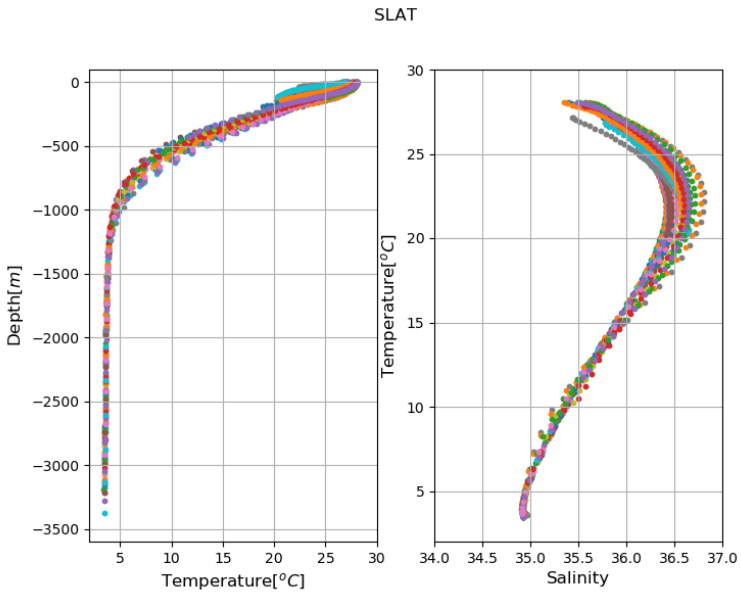

Figure 4.4: The temperature-depth profile (left panel) and temperature-salinity (TS) profile (right panel) of SLAT simulation interpolated at all the SAIC mooring locations. Each color represents a mooring station.

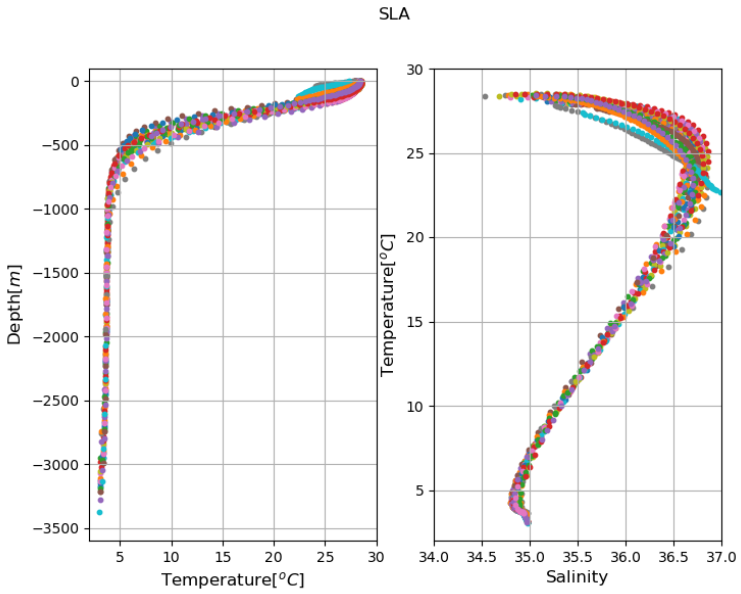

Figure 4.5: The temperature-depth profile (left panel) and temperature-salinity (TS) profile (right panel) of SLA simulation interpolated at all the SAIC mooring locations. Each color represents a mooring station.

The vertical TS profiles are selected from four PIES stations: 52, 62, 65, and 75. The distance between these stations is similar to the distance between stations A2 and C2. As the variations of temperature and salinity below 1000 m depth are negligible, Figures 4.6 and 4.7 only present the histograms in the upper 1000 m. The temperature from all three simulations is transferred to the in-situ temperature to be compared with the observations.

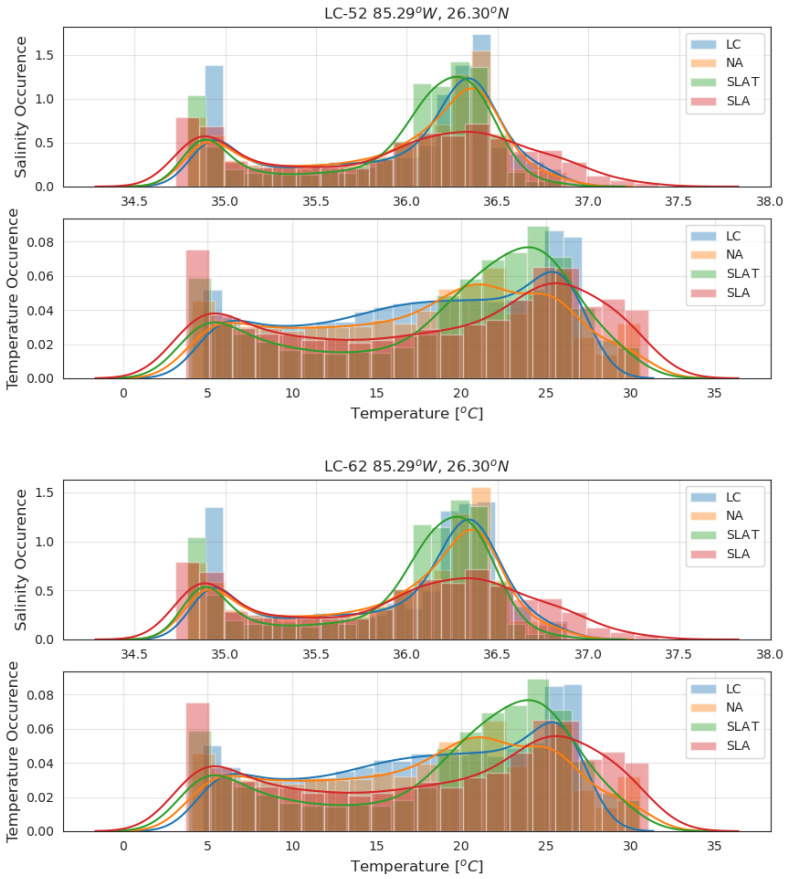

Figure 4.6: The salinity histogram (top panel) and temperature histogram (bottom panel) above 1000 m of PIES stations 52 (top two panels) and 62 (bottom two panels). The station information is in the subtitles. Each color represents a different dataset, blue is the mooring observation, orange is the NA simulation, green is the SLAT simulation, and red is the SLA simulation.

At stations 52 and 62, the SLA simulation has the highest temperature and salinity with the largest vertical gradient. The salinity distributions are similar among the NA simulation, SLAT simulation, and observations. As the SLAT simulation assimilates the satellite SST, the temperature structure of the SLAT is closest to the observations.

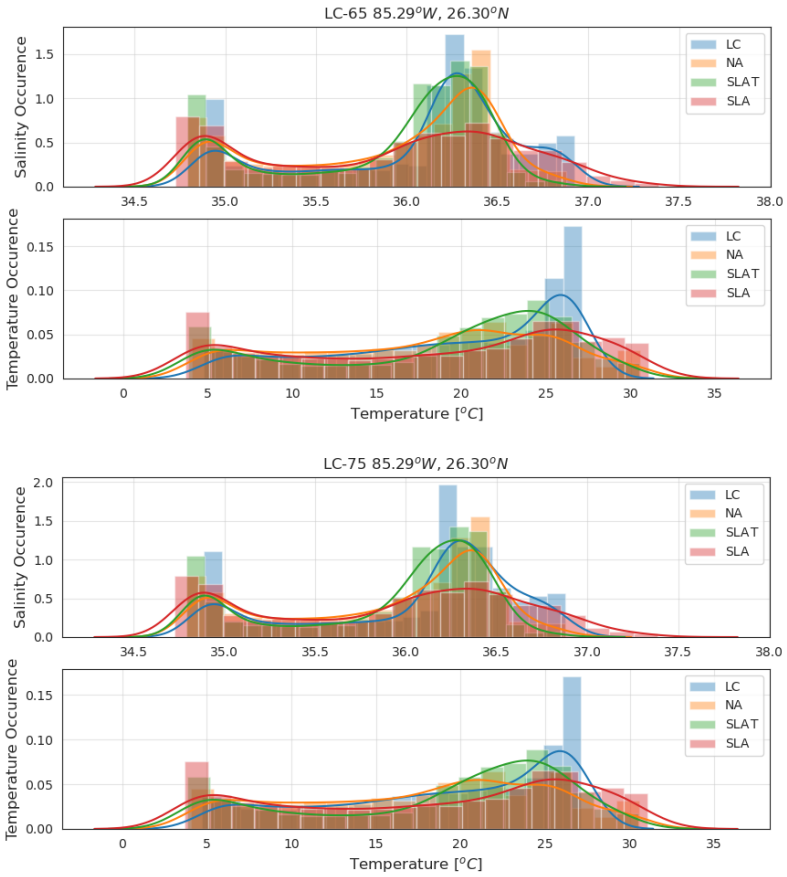

Figure 4.7: The salinity histogram (top panel) and temperature histogram (bottom panel) above 1000 m of PIES stations 65 (top two panels) and 75 (bottom two panels). The station information is in the subtitles. Each color represents a different dataset, blue is the mooring observation, orange is the NA simulation, green is the SLAT simulation, and red is the SLA simulation.

In Figure 4.7, the TS structures of different data are like in Figure 4.6. The SLA simulation still has the largest bias, which has a higher temperature and salinity on the surface and decreases sharply with depth to the values lower than other simulations around the thermocline. This thermal structure bias can also be seen in Figure 2.3, showing the SLA simulation has narrower isotherms. Hence, only the SLAT simulation will be used with the NA simulation for the following analysis to establish the indicator metric.

4.2 Wavelet Analysis

Before establishing the indicator metric of the LCEs shedding event, the target range of frequency occurring in the precursor patterns in section 3 should be identified. Hence, five regions in Figure 4.8 are selected to be used to present the precursor spatial patterns in Figure 3.19. Regions 1, 3, and 5 show the surrounding deep cyclonic eddies, and regions 2 and 4 indicate the deep anticyclonic eddy under the LC. The $u + v$ time series are the input vectors for the wavelet analysis, as $u + v$ contains the variance of both meridional and zonal velocities and the covariance part of them.

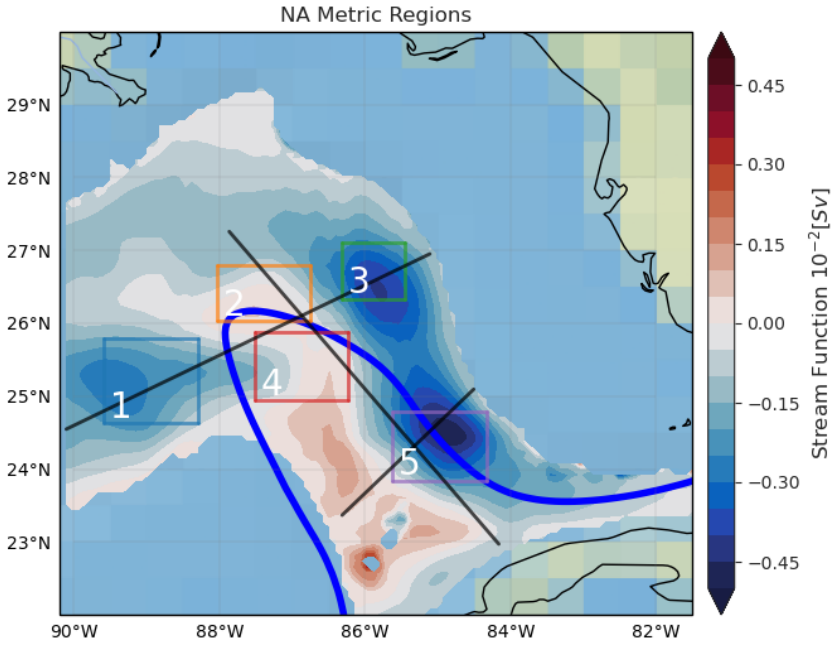

Figure 4.8: The time averaged steam function at the 27.5 kg/m^3 σ_θ layer in the NA simulation, the five boxes indicate the five regional averaged regions, the black lines present the three sections in Figure 4.9.

The temporal evolution of the 27.5 kg/m^3 σ_θ layer depth along the three sections in Figure 4.8 is shown in Figure 4.9. The depth data in Figure 4.9 is from the SLAT simulation, which is more

similar to the observations than the NA simulation. The depth of 27.5 kg/m^3 σ_θ layer is deeper in the NA simulation compared to the SLAT simulation.

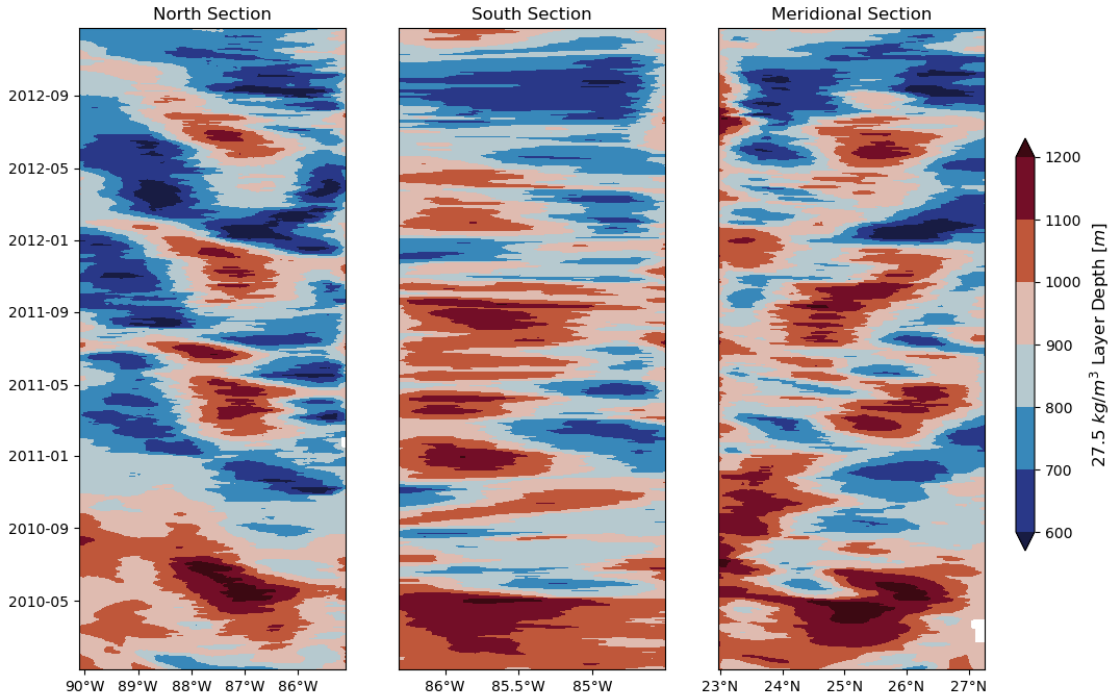

Figure 4.9: The depth of 27.5 kg/m^3 σ_θ layer in the SLAT simulation, the left panel is the north zonal section in Figure 4.8, the middle panel is the south section in Figure 4.8, and the right panel is the meridional section along the LC in Figure 4.8.

The deeper (red in Figure 4.9) 27.5 kg/m^3 σ_θ layer indicates the LC is in that area. The north section is consistent with LC dynamics studies, showing the deepened thermocline under the LC during LCEs shedding events. The south section presents similar features ahead to the north section, as the path of the LC is from the west side of the Yucatan Channel to the north. The meridional section along the LC shows a south-to-north propagation of the deepened layer with the penetration of the LC.

4.2.1 Observations

Three stations in regions 2, 3, and 4 are selected from the CICESE and SAIC moorings. In Figures 4.10 to 4.12, the wavelet transform of $u + v$ around the 27.5 kg/m^3 σ_θ layer shows the temporal evolution of their variance in the frequency domain. The input time series is 40-hour low-pass filtered, and observation gaps are filled by the flat line to keep the same length of time series. Station B1 is in region 2, showing the penetrated deep anticyclonic eddy with the LC intrusion. Station C1 is in region 3, presenting the intensified cyclonic eddies. Station N4 is in region 4, which is close to the west side of the LC necking-down region.

There are four LCEs shedding events during the observation period. The first one is the eddy Ekman (separation begins in 07/2009), the second one is the eddy Franklin (separation begins in 05/2010), the third one is the eddy Galileo (separation begins in 06/2011), and the fourth one is the eddy Hadal (separation begins in 08/2011). The eddy Galileo is significantly smaller than the others, and it cannot be identified by the 17 cm SSH contour in the two data assimilative runs.

At station B1, the LCEs shedding events are represented by the variance around the 32-64 days band. There are also some high-frequency variances being stimulated during these LCEs shedding events. The variances of the 8-16 days band are highlighted before or with the 32-64 days band variances. The first, second, fourth, and fifth peaks of the 8-16 days scale-averaged variance indicate the four observed LCEs shedding events, while the third peak may be the consequence of a failure separation with a prolonged intrusion.

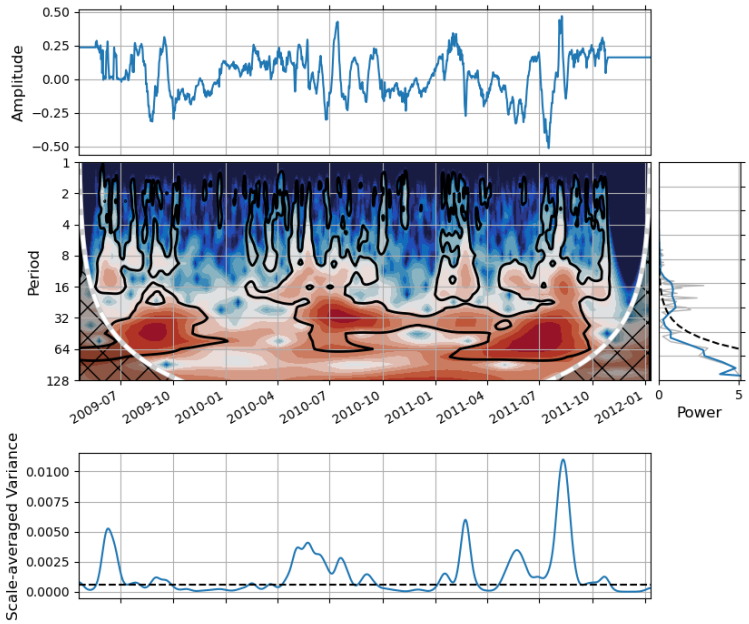

Figure 4.10: The wavelet analysis of $u + v$ at 900 m depth at station B1 in the period of days. The top panel shows the original input time series, the right panel in the middle is the wavelet transform, the left panel in the middle present the time-averaged power at different period, and the bottom panel is the temporal evolution of 8-16 days scale-averaged variance. The shadow region in the wavelet transform indicates the values below the 95% significant level. The dashed line in the bottom and right middle panels is the 95% significant level. The gray line in the right middle panel is the power via the fast Fourier transform.

In region 3, the wavelet analysis of $u + v$ at 900 m depth at station C1 presents a wide range of highlighted variance from mesoscale to the weather band as well. The 8-16 days scale-averaged variance reaches its peaks at different times compared to station B1 because the location changes from west to the east in the LC region. The peaks related to the final separation of eddy Ekman and eddy Franklin are the largest extremums. There are also peaks before the eddy Franklin and eddy Galileo indicating the beginning of the separations. As the eddy Hadal separates further north compared to others, station C1 only captures a relatively smaller variance at the 8-16 days band.

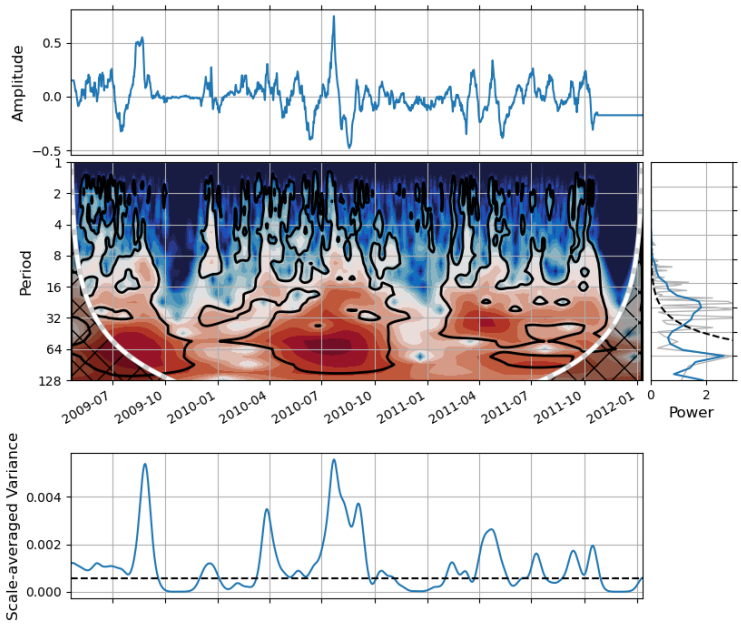

Figure 4.11: The wavelet analysis of $u + v$ at 900 m depth at station C1 in the period of days. The top panel shows the original input time series, the right panel in the middle is the wavelet transform, the left panel in the middle present the time-averaged power at different period, and the bottom panel is the temporal evolution of 8-16 days scale-averaged variance. The shadow region in the wavelet transform indicates the values below the 95% significant level. The dashed line in the bottom and right middle panels is the 95% significant level. The gray line in the right middle panel is the power via the fast Fourier transform.

Station N4 is in the southern region 4 along the west branch of the LC, presenting the penetration of the deep anticyclonic eddy. As the breaking location of the LCE shedding event is different, the 32-64 days band variance of eddy Franklin is as outstanding as stations B1 and C1. The high-frequency bands are still highlighted during the eddy Franklin and the other two. The 8-16 days scale-averaged variance becomes larger during the eddy Ekman, and before the eddy Franklin and eddy Galileo. Multiple regions should be combined to establish a general metric indicating the occurrence of the LCEs separation somewhere in the eastern GoM.

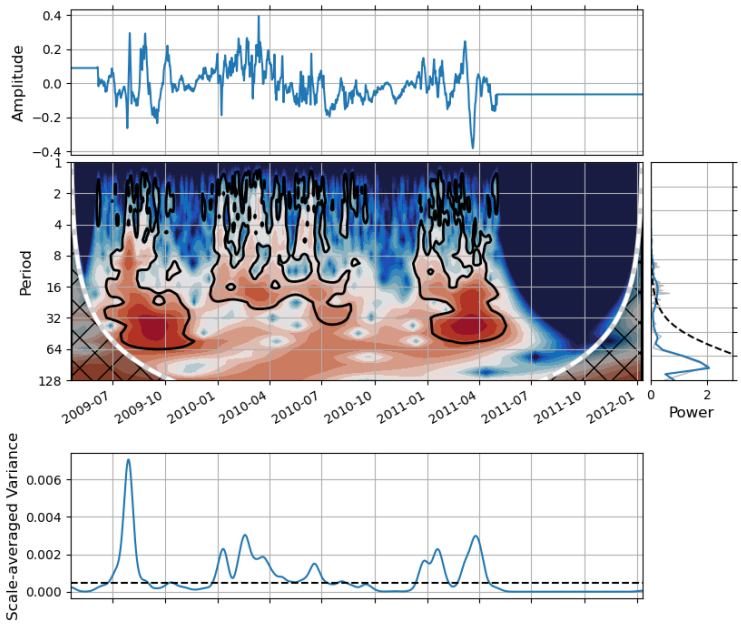

Figure 4.12: The wavelet analysis of $u + v$ at 901 m depth at station N4 in the period of days. The top panel shows the original input time series, the right panel in the middle is the wavelet transform, the left panel in the middle present the time-averaged power at different period, and the bottom panel is the temporal evolution of 8-16 days scale-averaged variance. The shadow region in the wavelet transform indicates the values below the 95% significant level. The dashed line in the bottom and right middle panels is the 95% significant level. The gray line in the right middle panel is the power via the fast Fourier transform.

Since the coverage of observations is limited in the northeast region of the LC, the western region 1 and eastern necking-down region 5 are not covered. Based on the SOM analysis in section 3, region 1 and region 5 are critical regions related to the LCEs separations. Before and during the separations, region 1 shows deep cyclonic anomalies as a blocking eddy, and region 5 contains the strongest deep cyclonic eddy in the eastern GoM. Hence, the NA and SLAT simulations are used for further analysis to find out the dynamical processes related to the 8-16 days band and establish the LC indicator based on all 5 regions.

4.2.2 Numerical Simulations

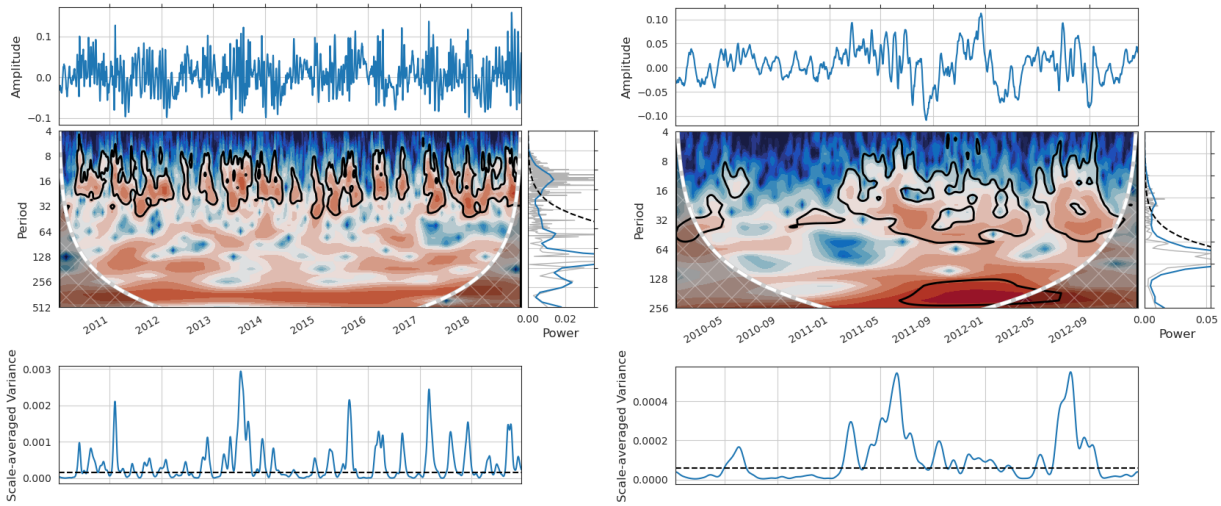

Figure 4.13: The wavelet analysis of regional averaged $u + v$ at 27.5 kg/m^3 σ_θ layer of region 1 in the period of days. The left part is the free-run simulation, and the right part is the SLAT simulation. The top panel shows the original input time series, the right panel in the middle is the wavelet transform, the left panel in the middle present the time-averaged power at different period, and the bottom panel is the temporal evolution of 8-16 days scale-averaged variance. The shadow region in the wavelet transform indicates the values below the 95% significant level. The dashed line in the bottom and right middle panels is the 95% significant level. The gray line in the right middle panel is the power via the fast Fourier transform.

The regional averaged $u + v$ at 27.5 kg/m^3 σ_θ layer of the five regions in Figure 4.8 are transformed by the wavelet analysis in NA and SLAT simulations shown in Figures 4.13 to 4.17. In Figure 4.13, the wavelet results of the two simulations present the highlighted 8-16 days band variance related to the LCEs shedding events, especially in the free-run simulation. Still, not all the separation events in each simulation are captured by the 8-16 days scale-averaged variance of region 1. Comparing the NA 8-16 days scale-averaged variance time series with Tables 2.2 and 2.3 (shown as shading in Figures 3.14 and 3.15), most peaks indicate an LCE detachment except the second peak in 2012 and the first peak in 2017. In the SLAT simulation, the third event is not

shown as significant as others in late 2011, and there are additional peaks related to the second LCE separation, which is a deeply penetrated case.

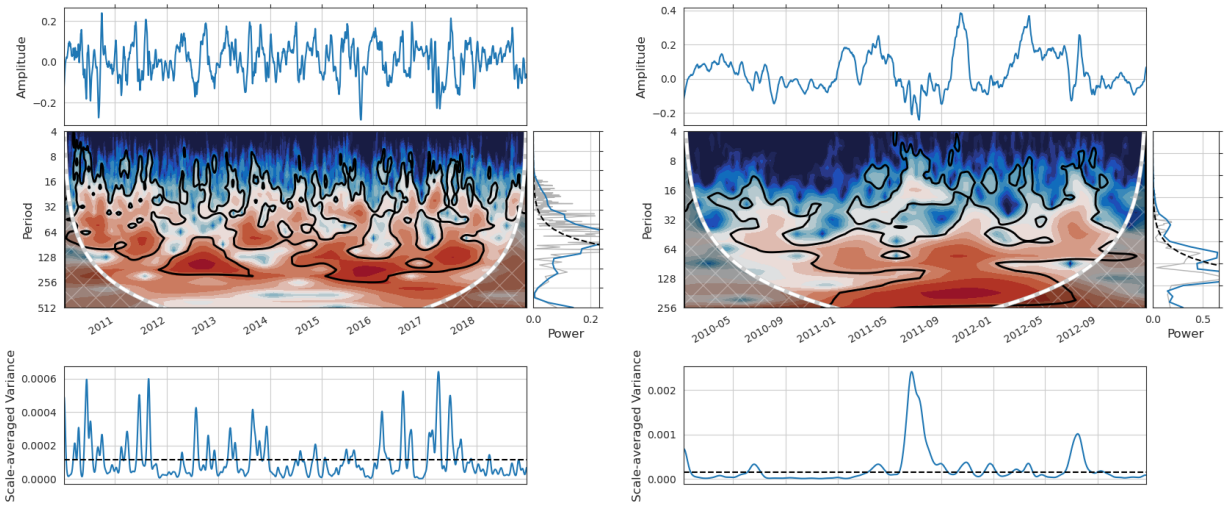

Figure 4.14: The wavelet analysis of regional averaged $u + v$ at 27.5 kg/m^3 σ_θ layer of region 2 in the period of days. The left part is the free-run simulation, and the right part is the SLAT simulation. The top panel shows the original input time series, the right panel in the middle is the wavelet transform, the left panel in the middle present the time-averaged power at different period, and the bottom panel is the temporal evolution of 8-16 days scale-averaged variance. The shadow region in the wavelet transform indicates the values below the 95% significant level. The dashed line in the bottom and right middle panels is the 95% significant level. The gray line in the right middle panel is the power via the fast Fourier transform.

The region 2 8-16 days scale-averaged variance (Figure 4.14) can show the most detachments in the free-run simulation except the first peak in 2017. In the SLAT simulation, the region 2 8-16 days scale-averaged variance has a tremendous before the second LCE detachment, a regular peak during the fourth LCE shedding event, and relatively more minor peaks around the first and third LCEs shedding events.

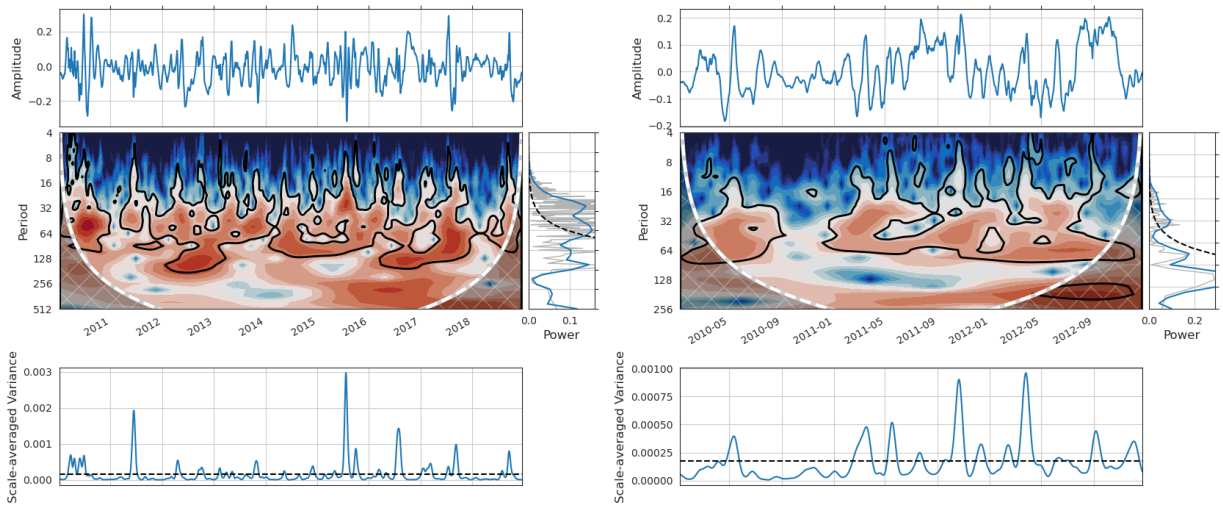

Figure 4.15: The wavelet analysis of regional averaged $u + v$ at 27.5 kg/m^3 σ_θ layer of region 3 in the period of days. The left part is the free-run simulation, and the right part is the SLAT simulation. The top panel shows the original input time series, the right panel in the middle is the wavelet transform, the left panel in the middle present the time-averaged power at different period, and the bottom panel is the temporal evolution of 8-16 days scale-averaged variance. The shadow region in the wavelet transform indicates the values below the 95% significant level. The dashed line in the bottom and right middle panels is the 95% significant level. The gray line in the right middle panel is the power via the fast Fourier transform.

The 8-16 days scale-averaged variance above 95% significant level of region 3 (Figure 4.15) only indicates the LCEs shedding events 1, 3, 5, 8, 11, 13 to 15, and 19. In the SLAT simulation, the region 3 8-16 days scale-averaged variance reaches the local peaks before the four LCEs shedding events, and there are two similar peaks before the second event.

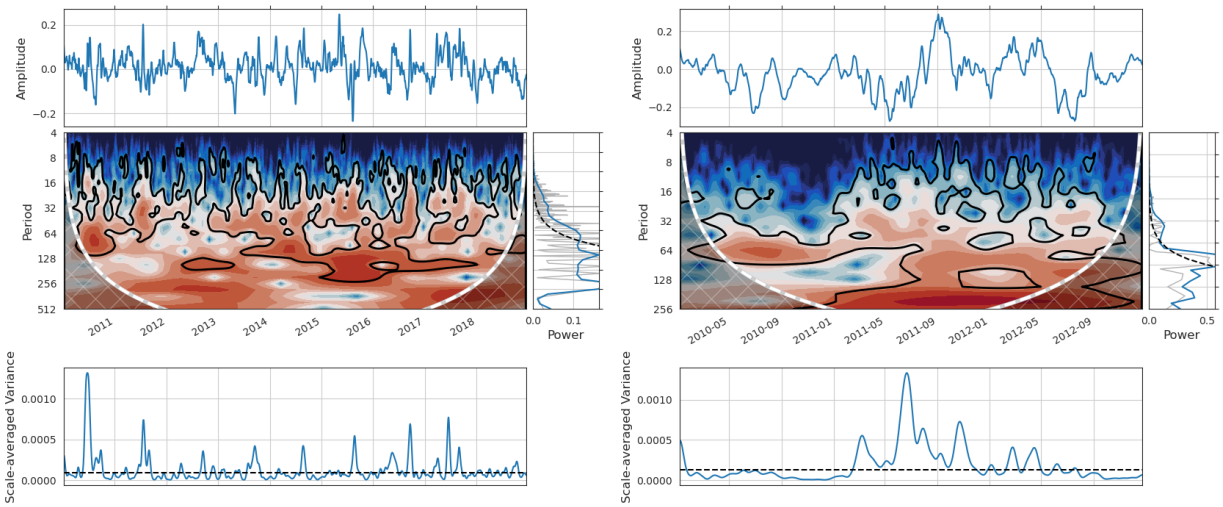

Figure 4.16: The wavelet analysis of regional averaged $u + v$ at 27.5 kg/m^3 σ_θ layer of region 4 in the period of days. The left part is the free-run simulation, and the right part is the SLAT simulation. The top panel shows the original input time series, the right panel in the middle is the wavelet transform, the left panel in the middle present the time-averaged power at different period, and the bottom panel is the temporal evolution of 8-16 days scale-averaged variance. The shadow region in the wavelet transform indicates the values below the 95% significant level. The dashed line in the bottom and right middle panels is the 95% significant level. The gray line in the right middle panel is the power via the fast Fourier transform.

In region 4 (Figure 4.16), 8-16 days scale-averaged variance of NA simulation show the local peaks around the LCEs shedding events 1, 3, 5, 8, 10 to 15, and 19. More cases are captured by region 4 than in region 3 of the free-run simulation. Only the second and third LCEs shedding events in the SLAT simulation are represented by region 4, which are the cases related to the prolonged LC penetration.

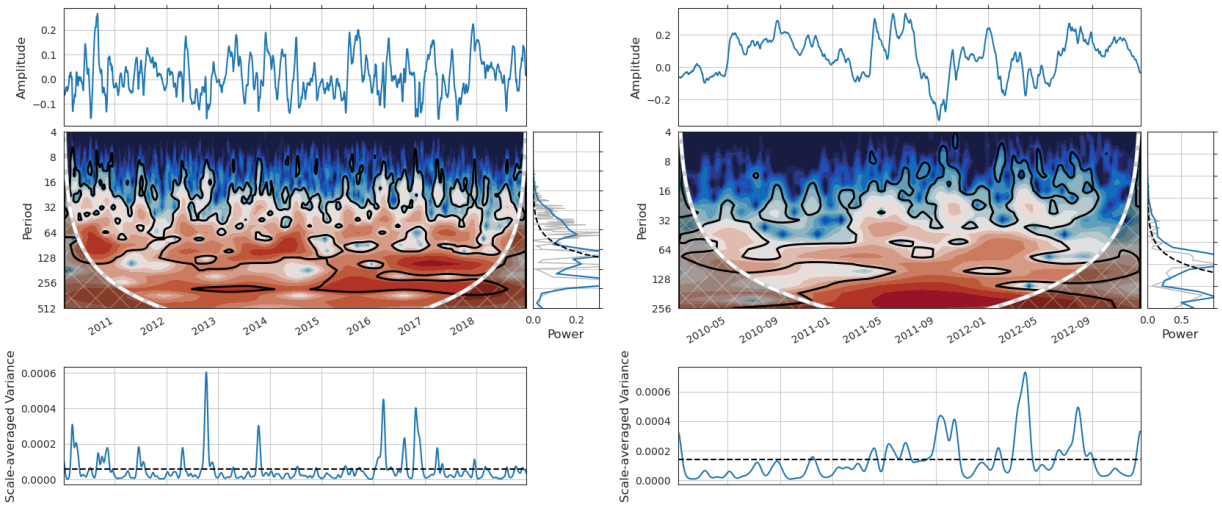

Figure 4.17: The wavelet analysis of regional averaged $u + v$ at 27.5 kg/m^3 σ_θ layer of region 5 in the period of days. The left part is the free-run simulation, and the right part is the SLAT simulation. The top panel shows the original input time series, the right panel in the middle is the wavelet transform, the left panel in the middle present the time-averaged power at different period, and the bottom panel is the temporal evolution of 8-16 days scale-averaged variance. The shadow region in the wavelet transform indicates the values below the 95% significant level. The dashed line in the bottom and right middle panels is the 95% significant level. The gray line in the right middle panel is the power via the fast Fourier transform.

The region 5 (Figure 4.17) is the eastern necking-down region based on the previous studies, but it does not show extreme peaks around all LCEs shedding events in NA and SLAT simulations. In the NA simulation, the region 5 8-16 days scale-averaged variance shows peaks before the LCEs shedding events 1 to 3, 5, 8, and 12 to 14. The region 5 8-16 days scale-averaged variance of the SLAT simulation indicates the third and fourth LCEs shedding events and reaches its maximum peak in early 2012. The variations in the necking-down region at 27.5 kg/m^3 σ_θ layer is not as critical as in the upper layer.

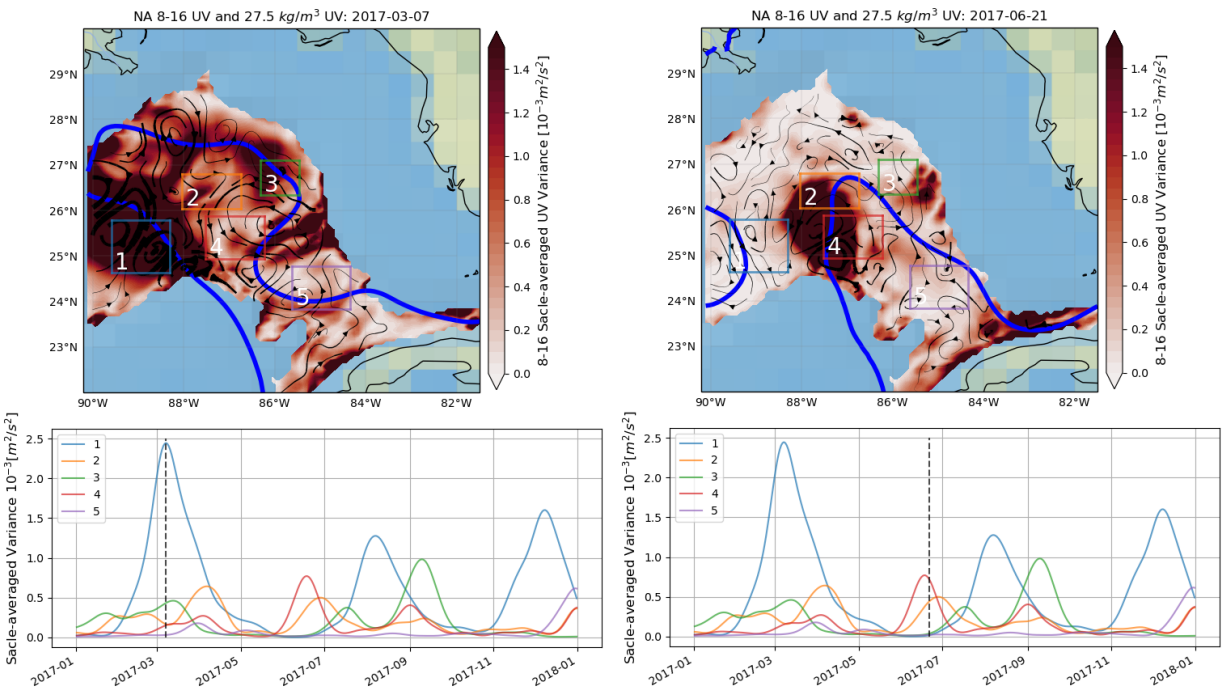

Figure 4.18: Two snapshots of the 8-16 days scale-averaged variance of $u + v$ distribution in the NA simulation, the time is on the title of each panel. In the upper panels, the streamline indicates the 8-16 band-pass filtered u and v velocity, the colors present the amplitude of the 8-16 days scale-averaged variance of $u + v$, and the blue contour is the simultaneous 17 cm SSH on the surface. The lower panels present the regional averaged 8-16 days scale-averaged variance time series of five regions, the vertical dashed line indicates the time of the snapshot.

Figure 4.18 shows an example of the 8-16 days scale-averaged variance of $u + v$ interacts with the LCEs shedding events. The areas with darker colors have larger 8-16 days scale-averaged variance, which are the pathway of the 8-16 days band propagating wave and the interface between some stationary deep eddies. The left snapshot is 03/07/2017, which has a tremendous peak in region 1. This peak is the consequence of the high-frequency propagating wave under the west branch of the LC to the northwest. As the propagation of this high-frequency propagating wave does not cross the bottom of LC, the LC keeps penetrating into the GoM instead of shedding the LCE. The right case is 06/21/2017, and it shows a short LCE separation with an 8-16 days scale-averaged variance peak in regions 2 and 4. The high-frequency propagating wave initializes when the LC is penetrating zonally to the west, then this high-frequency propagating wave passes across

the bottom of the LC neck and contributes to the LCE separation.

The wavelength of these 8-16 days waves varies around ~200 km during different LCEs shedding events, which are identified as MRG waves (Clarke, 1983; Pedlosky et al., 1987) in this dissertation and will be discussed in section 4.5. More analyses of this mysterious wave properties will be done in the future works. As the different regions represent different LCEs shedding events in the two simulations, the signals of all five regions should be combined to establish the indicating metric of the occurrence of LCEs separations.

4.3 Multi-variables Analysis

The LCEs shedding events not only interact with the $u + v$ at the 27.5 kg/m^3 σ_θ layer but also with some other processes, such as the variation of PV. Based on the equation 2.11, the PV is represented by two terms as the relative vorticity ($\frac{\partial \boldsymbol{v}}{\partial x} - \frac{\partial \boldsymbol{u}}{\partial y}$) term and vertical density gradient ($\frac{\partial \rho}{\partial z}$) term. The relative vorticity term presents the rotation of the selected water column, and the vertical density gradient is the stretching/compressing term showing the layer thickness in density coordinate.

Fifteen variables (three regional averaged variables of five regions) are used in a PCA analysis to extract the contributions of $u + v$ among different dynamical processes in this section. All the variables are at the 27.5 kg/m^3 σ_θ layer to show the variations in the lower layer in the LC region. The input variables are 8-16 days scale-averaged variance of $u + v$ to indicate the LCEs shedding events, the relative vorticity to present the rotating direction and intensity, and the vertical density gradient as the variations in the thermal structure.

4.3.1 NA Simulation

The fifteen variables in the NA simulation are temporally and spatially subsampled to 9 km and 1 day after 40-hour low-pass filtered. The leading four modes are shown in Figures 4.19 to 4.21. The total contribution of the leading four modes is about 50%. The first mode is controlled by the 8-16 days scale-averaged variance in regions 2 and 3, and the vertical density gradient in region 2. At the same time, the relative vorticity in regions 2 and 4 presents an opposite sign compared to

the other areas. The temporal evolution of PC1 time series is like the SSHA index, which reaches a local peak before the LCEs shedding events and decreases till the final separation. Before most LCEs shedding events, the regions 1 to 4 reach a large 8-16 days scale-averaged variance. Regions 2 and 3 gain more than regions 1 and 4. Regions 2 and 4 have anticyclonic anomalies, and regions 1, 3, and 5 show cyclonic anomalies, which is consistent with the SOM precursor patterns in section 3. At the same time, regions 2 and 4 are also compressed by the penetrated LC in the upper layer. Therefore, the PC1 shows the major features of the precursor patterns for most LCEs shedding events.

PC2 is a relative vorticity mode, the relative vorticity in regions 2 to 5 contributes the most to PC2. As region 4 has an opposite sign to the other regions, PC2 presents a cyclonic (anticyclonic) anomaly in region 4, surrounded by anticyclonic (cyclonic) anomalies. Region 1 does not show many contributions to the PC2. Therefore, PC2 presents the interaction between the deep anticyclonic eddy coming under the LC with the surrounding deep cyclonic eddies, and the frequency of the PC2 temporal evolution is higher than the PC1.

PC3 and PC4 are shown in Figure 4.20, and the leading variables in PC3 are the 8-16 days scale-averaged variance and vertical density gradient in region 5 with a negative relationship between them. It means when the intruding LC compresses region 5, the MRG wave or deep eddies interface around region 5 is weakened. The 8-16 days scale-averaged variance and vertical density gradient in region 1 show the same changes as region 5, while the amplitude is smaller. At the same time, the 8-16 days scale-averaged variance in regions 2 and 4 are increasing. Since the relative vorticity is still opposite between regions 1, 3, and 5 and regions 2 and 4, the PC3 presents the feature of a deep anticyclonic eddy under the retracted LC in region 5 and another deep anticyclonic eddy under the separated LCE covering region 1 (or a growing anticyclonic eddy under the intruding LC surrounding by deep cyclonic eddies).

The 8-16 days scale-averaged variance in region 4 contributes significantly larger than other variables to PC4. The time series of PC4 shows the peaks similar to the 8-16 days scale-averaged variance time series in Figure 4.16. Hence, PC4 is dominated by the $u + v$ variance in region 4

under the LC.

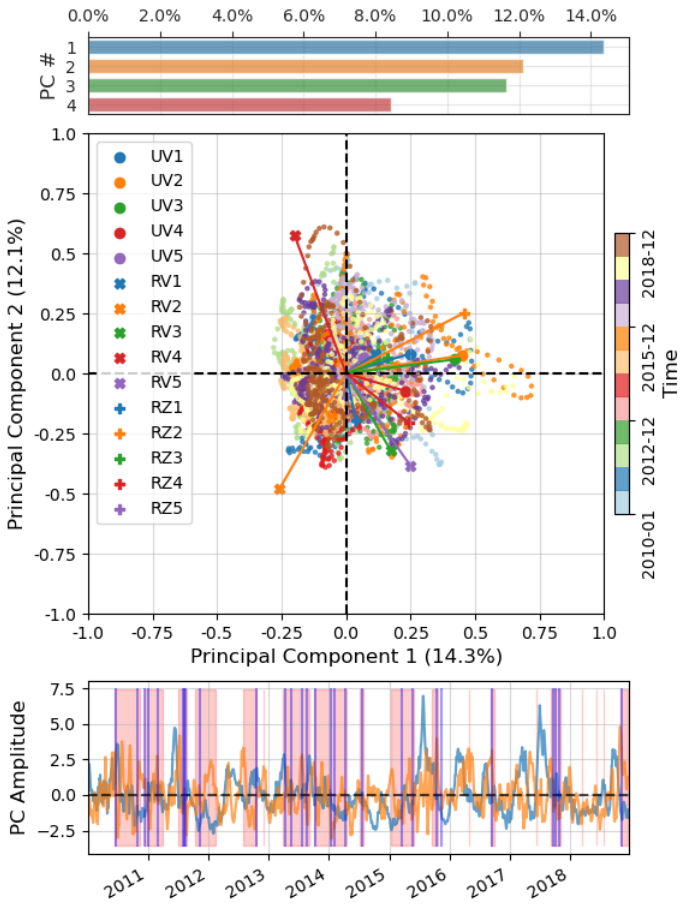

Figure 4.19: The PCA analysis results of the fifteen variables in NA simulation. The top panel shows the contributions of the leading four modes. The middle panel presents the PC1 and PC2 coefficients of the fifteen variables and the projected time series in the PC1 and PC2 coordinate. The different colors in the middle panel indicate the different regions from 1 to 5, and the different markers are the different variables. UV stands for the 8-16 days scale-averaged variance of $u + v$, RV stands for the relative vorticity term, and RZ is the vertical density gradient term. The color map presents the temporal evolution of the projected time series. The bottom panel shows the PC1 and PC2 time series, and their colors are as same as the top panel. The red shadings are the LCEs shedding events, and the vertical blue lines indicate the time of reattachments.

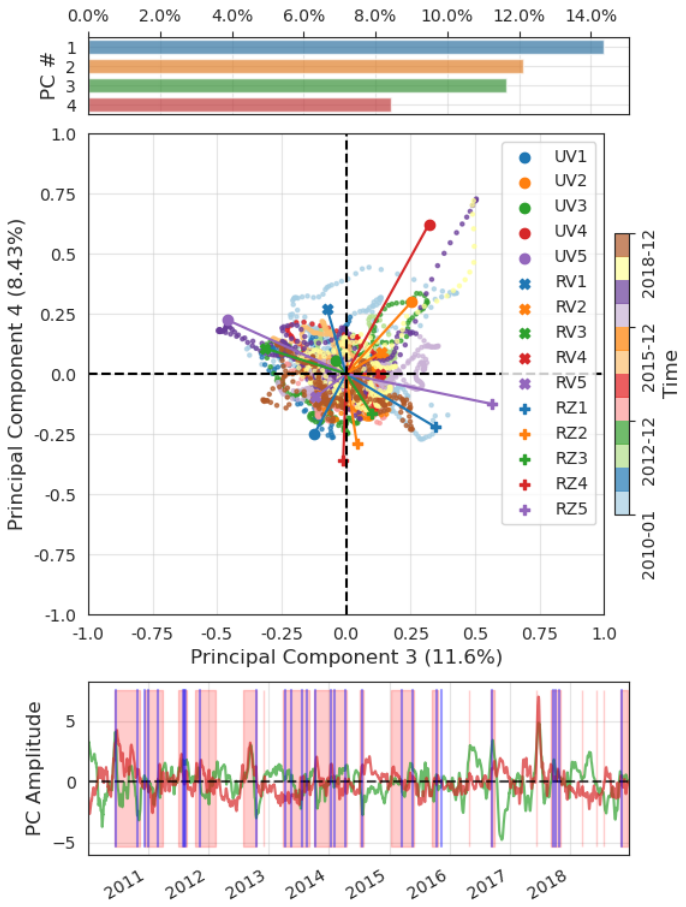

Figure 4.20: The PCA analysis results of the fifteen variables in NA simulation. The top panel shows the contributions of the leading four modes. The middle panel presents the PC3 and PC4 coefficients of the fifteen variables and the projected time series in the PC3 and PC4 coordinate. The different colors in the middle panel indicate the different regions from 1 to 5, and the different markers are the different variables. UV stands for the 8-16 days scale-averaged variance of $u + v$, RV stands for the relative vorticity term, and RZ is the vertical density gradient term. The color map presents the temporal evolution of the projected time series. The bottom panel shows the PC3 and PC4 time series, and their colors are as same as the top panel. The red shadings are the LCEs shedding events, and the vertical blue lines indicate the time of reattachments.

NA PC1-4 Coefficients

	UV1	UV2	UV3	UV4	UV5	RV1	RV2	RV3	RV4	RV5	RZ1	RZ2	RZ3	RZ4	RZ5
PC1	0.25	0.45	0.42	0.23	0.07	0.11	-0.26	0.17	-0.20	0.25	0.04	0.46	0.16	0.24	-0.00
PC2	0.08	0.07	0.06	-0.07	0.07	0.08	-0.48	-0.32	0.58	-0.38	-0.19	0.25	0.07	-0.21	-0.10
PC3	-0.12	0.25	-0.04	0.32	-0.46	-0.07	0.14	-0.32	0.13	-0.12	0.35	0.04	0.10	-0.01	0.57
PC4	-0.25	0.30	0.06	0.62	0.22	0.27	0.09	0.11	0.00	-0.10	-0.22	-0.29	-0.16	-0.36	-0.13

Figure 4.21: The coefficients of PCA analysis results for the fifteen variables in NA simulation. The colors of the headers are as same as Figures 4.19 and 4.20 to show the order of modes and regions. The yellow shades indicate the coefficient parameter of the 8-16 days scale-averaged variance used in section 4.4.

4.3.2 SLAT Simulation

The same fifteen variables in the SLAT simulation are temporally and spatially subsampled to 9 km and 1 day after 40-hour low-pass filtered as the NA simulation PCA analysis. The leading four modes are shown in Figures 4.22 to 4.24. The total contribution of the leading four modes is over 60%. Similar to the PC1 in NA PCA analysis, the time series of SLAT PC1 decreases to zero when the LCEs shedding events begins and keeps decreasing during the events. The positive PC1 shows the SOM precursor patterns as well, which has an anticyclonic eddy in regions 2 and 4 being surrounded by cyclonic eddies in regions 1, 3, and 5 with the increasing 8-16 days scale-averaged variance of $u + v$.

PC2 is controlled by the 8-16 days scale-averaged variance in regions 1, 2, and 4, covering the western part of the LCS. When the LCEs separate from the LC and propagate into region 1, the retracted LC is not as strong as before the separation, and the eastern regions 2, 3, 4, and 5 are relatively stretched. The increasing 8-16 days scale-averaged variance in regions 1, 2, and 4 is the consequence of the passing MRG wave, which contributes to the LCEs separations.

In Figure 4.23, PC3 is dominated by the vertical density gradient in region 2 and relative vorticity in region 4. The positive PC3 time series show a compressed LCS in regions 2 to 4 with

a cyclonic anomaly in region 4 surrounded by anticyclonic anomalies. PC4 shows the features of relative vorticity in region 2 and the 8-16 days scale-averaged variance in region 3. Since region 3 is compressed when region 2 is stretched, positive PC4 indicates the cyclonic anomalies generated from region 3 propagate to region 2.

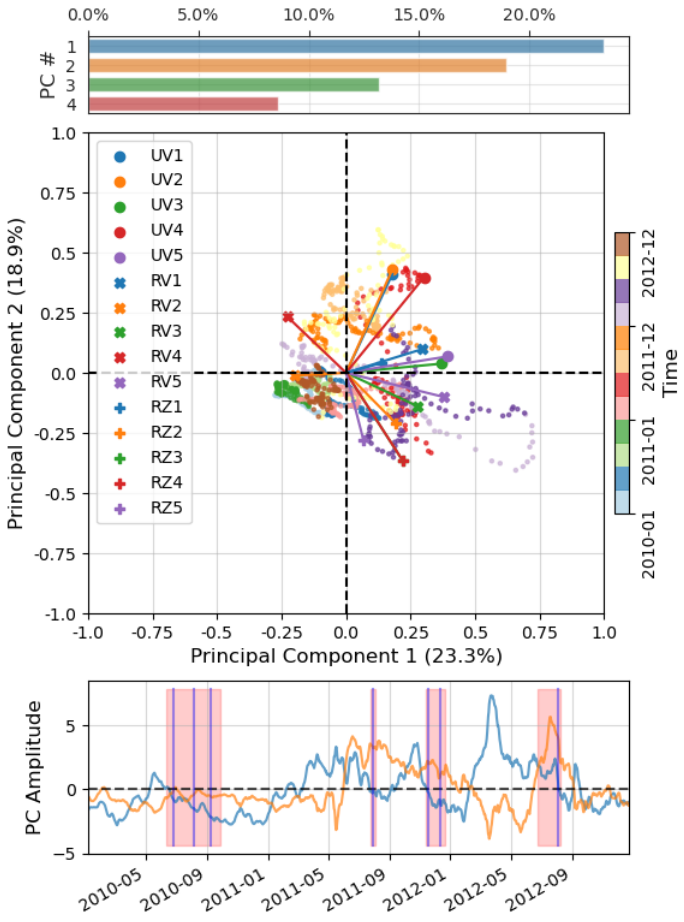

Figure 4.22: The PCA analysis results of the fifteen variables in SLAT simulation. The top panel shows the contributions of the leading four modes. The middle panel presents the PC1 and PC2 coefficients of the fifteen variables and the projected time series in the PC1 and PC2 coordinate. The different colors in the middle panel indicate the different regions from 1 to 5, and the different markers are the different variables. UV stands for the 8-16 days scale-averaged variance of $u + v$, RV stands for the relative vorticity term, and RZ is the vertical density gradient term. The color map presents the temporal evolution of the projected time series. The bottom panel shows the PC1 and PC2 time series, and their colors are as same as the top panel. The red shadings are the LCEs shedding events, and the vertical blue lines indicate the time of reattachments.

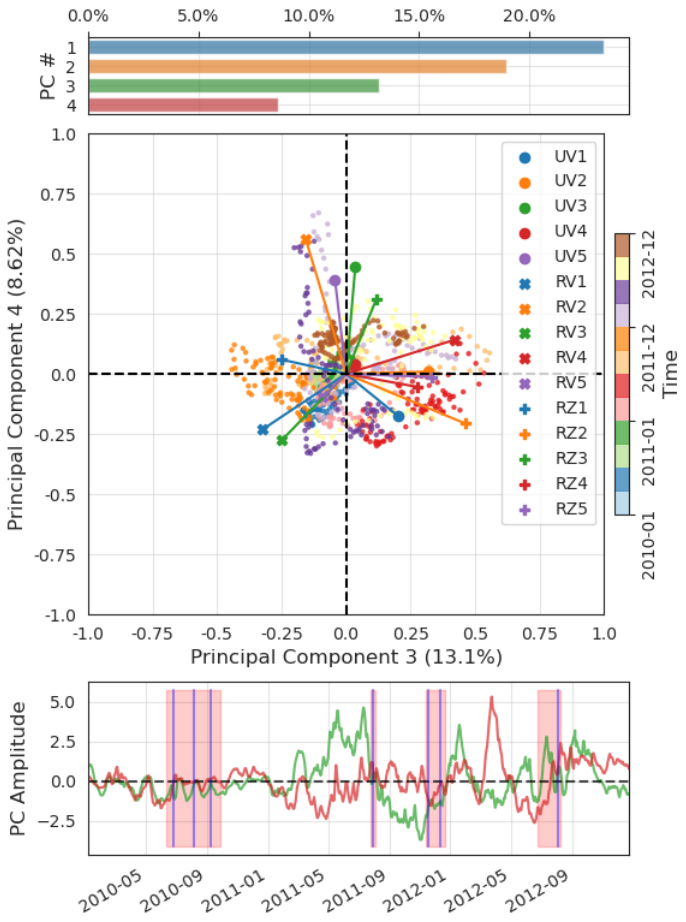

Figure 4.23: The PCA analysis results of the fifteen variables in SLAT simulation. The top panel shows the contributions of the leading four modes. The middle panel presents the PC3 and PC4 coefficients of the fifteen variables and the projected time series in the PC3 and PC4 coordinate. The different colors in the middle panel indicate the different regions from 1 to 5, and the different markers are the different variables. UV stands for the 8-16 days scale-averaged variance of $u + v$, RV stands for the relative vorticity term, and RZ is the vertical density gradient term. The color map presents the temporal evolution of the projected time series. The bottom panel shows the PC3 and PC4 time series, and their colors are as same as the top panel. The red shadings are the LCEs shedding events, and the vertical blue lines indicate the time of reattachments.

SLAT PC1-4 Coefficients

	UV1	UV2	UV3	UV4	UV5	RV1	RV2	RV3	RV4	RV5	RZ1	RZ2	RZ3	RZ4	RZ5
PC1	0.18	0.18	0.37	0.30	0.39	0.29	-0.20	0.28	-0.23	0.38	0.14	0.19	0.22	0.22	0.07
PC2	0.41	0.43	0.04	0.40	0.07	0.10	-0.01	-0.14	0.23	-0.10	0.04	-0.21	-0.37	-0.37	-0.28
PC3	0.20	0.32	0.04	0.03	-0.04	-0.32	-0.16	-0.25	0.42	-0.09	-0.25	0.46	0.12	0.28	0.33
PC4	-0.17	0.01	0.45	0.04	0.39	-0.23	0.56	-0.28	0.14	-0.10	0.06	-0.21	0.31	-0.05	-0.01

Figure 4.24: The coefficients of PCA analysis results for the fifteen variables in SLAT simulation. The colors of the headers are as same as Figures 4.23 and 4.24 to show the order of modes and regions. The yellow shades indicate the coefficient parameter of the 8-16 days scale-averaged variance used in section 4.4.

4.4 Indicator Metric

The indicator metric of LCEs shedding events is established by the weighted sum of the 8-16 days scale-averaged variance of $u + v$ from the five regions. The weighted parameters are calculated based on the multiple variables PCA analysis. For each region, the weighted parameter is its highest PCA coefficient multiplied by the contribution of the corresponding PC (only the leading four modes are considered). For instance, the weighted parameter for region 3 in SLAT simulation is 0.08×0.45^2. Since the amplitudes are in different orders of ten among the regions, all the variances are normalized from 0 to 1 by their maximum. The metric is calculated as equation 4.1.

$$f(t) = \sum_{i=1}^{5} c_j \cdot r_{ij}^2 \cdot UV_i(t) \tag{4.1}$$

In equation 4.1, c is the PC contribution of each mode, r is the PCA coefficient, UV represents the 8-16 days scale-averaged variance time series, i is the number of regions, j is the PC that has the highest PCA coefficient for that region. The summed time series of NA and SLAT simulations are shown in Figure 4.25.

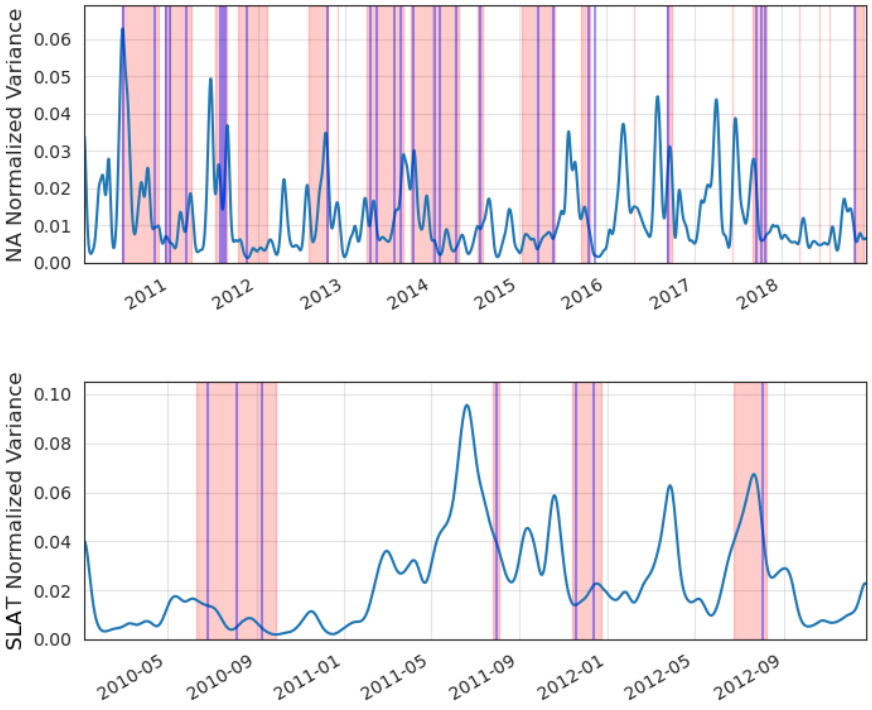

Figure 4.25: The indicator metric of NA simulation (top panel) and SLAT simulation (bottom panel). The red shadings are the LCEs shedding events defined by the close of 17 cm SSH, and the blue vertical lines indicate the reattachments of LCEs.

The indicator metric does not represent the LCEs shedding event identified by the traditional 17 cm SSH, but it is a necessary condition for the separations in both NA and SLAT simulations. For all the LCEs shedding events, this normalized 8-16 days scale-averaged variance index reaches a local peak before or during the events, except for the tiny LCEs in the middle of 2018 of NA simulation.

The LCE Franklin (first event in Table 2.3) is identified as a large LCE separated from the LC in 2010, dissipating in the southwestern GoM based on observations. The development and separation of LCE Franklin are reconstructed as the first LCE shedding event in the SLAT simulation, but it stays in the eastern GoM and dissipates. The 8-16 scale-averaged variance indicators in each region and the combined indicator do not show a significant increase in the middle of 2010 in SLAT simulation, while it is relatively more significant in the three observation stations. As

the LCE Franklin in SLAT simulation stays in the eastern GoM and is only defined by the 17 cm SSH on the surface, it may not be counted as an actual LCEs separation. The separation processes identified from the bottom of the LCS and the details of the MRG waves will be discussed via the LCEs shedding cases in R-CESM simulations.

4.5 Mixed Rossby-Gravity Wave

The temporal and spatial evolution of 17 cm SSH is essential to identifying the LCS, but may not be an ideal indicator of LCEs separations. The disconnect between the LCEs and the LC on the surface can be just the cyclonic anomalies caused by the passing through frontal eddies and other processes, and it may not be the actual symbol for a successful LCE separation. As the LCS can impact the western GoM primarily via the westward propagation of the separated LCEs, the successful LCEs separations are defined as the LCEs passing through the 90 °W into the western GoM with some accompanied dynamical phenomenons. The traditional method of defining the LCEs shedding events via the artificial 17 cm SSH may need to be improved since a constant value does not fit for cases with different dynamical scenarios, especially for an energetic system like the LCS. The LCEs shedding events 16 and 19 in the NA simulation and event 1 in the SLAT simulation are not considered as completed LCEs separations. The features of MRG waves are also not highlighted during these three cases, they are only identified by the closed 17 cm SSH from the surface. The rest seventeen cases in the NA simulation and three cases in the SLAT simulation are sorted into two groups based on the temporal and spatial evolution of MRG waves at the bottom of the LCS. There are five scenarios of the wave trains being defined based on their locations and pathways.

Compared to the equatorial MRG waves (Dickinson and Molinari, 2002; Pujiana and McPhaden, 2021), the waves in this research around 26°N have similar dispersion relations. Their wavelength is 10-20 times shorter than the equatorial MRG waves, which is about 100-200 km. Their phase speed is 10-20 times slower than the equatorial MRG waves as well, which is around 0.1 to 0.3 m/s. Based on the normalized dispersion curves for ocean waves, these waves are above the Rossby waves and close to the MRG waves (Gill and Adrian, 1982). Instead of being simulated by the wind

stress, the features of the MRG waves in the LCS region come from the interaction between the strong penetrating LC and the sharp topography from different directions. The energy from the strong deforming LC dissipates into higher frequency bands via the baroclinic instability. The MRG waves are mainly stimulated in three regions: the Mississippi Fan, the Yucatan Shelf, and the Florida Escarpment. The duration of these wave trains is from ~ 2 to 8 weeks, depending on the length of interaction between the LCS and the topography.

4.5.1 Two Groups of Shedding Cases

The first group of separations includes the LCEs shedding events 1, 3, 5, 6, 8, 10, 11, 12, 13, 15, 16, and 17 in NA simulation and event 2 in SLAT simulation. The primary feature of the first group is the zonally propagating MRG waves from east to west. Two typical cases in the first group are shown in Figures 4.26 to 4.29.

The case 6 in NA simulation is shown in Figures 4.26 and 4.27, it presents a typical case of a westward propagating wave generated from the Mississippi Fan. In Figure 4.26, the top panel shows the spatial difference between 2012-12-08 (shading colors) and 2012-12-05 (colored contours) on the 27.5 kg/m^3 σ_θ layer. The major feature is the westward MRG wave under the separated LCE, which was developed before the separation. The bottom 2D FFT displays the primary wavelengths in the chosen domain, and the input data is the 9 km subsampled $u + iv$ in the top panel. Therefore, the spatial Nyquist frequency of this domain is 18 km, which is around 5.6×10^{-5} m^{-1}. The fundamental spatial frequency in the zonal direction is smaller than the meridional direction due to the difference in the length and width of the chosen domain so that the zonal wavenumber has a higher resolution. The highlighted wavenumber band is around 0.5×10^{-5} m^{-1}, which equals 200 km in wavelength. The difference between the negative and positive wavenumbers indicates the phase shift between u and v rather than the propagation direction. The alignment of highlighted wavenumbers in different quadrants can present the propagation axis. Hence, the primary wave identified by the 2D FFT propagates along the zonal direction, and the three days difference in the top panel presents this wave propagating toward the west.

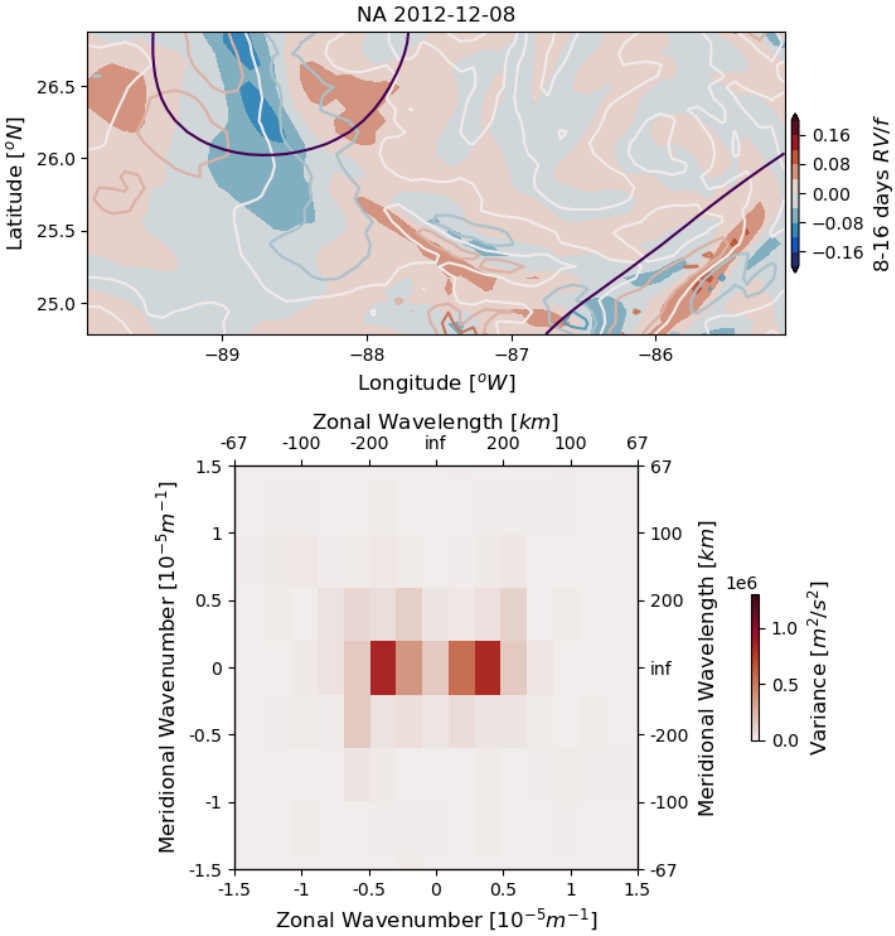

Figure 4.26: The top panel shows the normalized relative vorticity calculated from the 8-16 days band-pass filtered velocities in the selected region of NA simulation on the 27.5 kg/m^3 σ_θ layer, the shading colors indicate the relative vorticity at the selected time shown in the title (2012-12-08). The colored contours present the relative vorticity three days before the chosen time (2012-12-05), and the purple contour shows the distribution of 17 cm SSH at the chosen time (2012-12-08). The bottom panel presents the corresponding spatial FFT of $u + iv$ at the chosen time (2012-12-08).

Figure 4.27 shows the vertical structure of u, v, and $\sqrt{u^2 + v^2}$ at 89.1°W, 26.2°N from 27.1 to 27.6 kg/m^3 σ_θ layers, where is around the center of the MRG wave pathway shown in Figure 4.26. All variables indicate the bottom of the LCS (27.5 kg/m^3 σ_θ layer) become more energetic during the final separation of the LCE. The zonal velocity u present a bottom leading phase during the separation and the meridional velocity v is more related to the intensity. The total variance (speed)

is dominated by the u velocity before the separation and by the v velocity during the separation. This MRG wave is stimulated in the entire upper ~1000 m during the final separation when the deforming LC is extraordinarily energetic and unstable. Then, it dissipates from the surface to the bottom of the LCS.

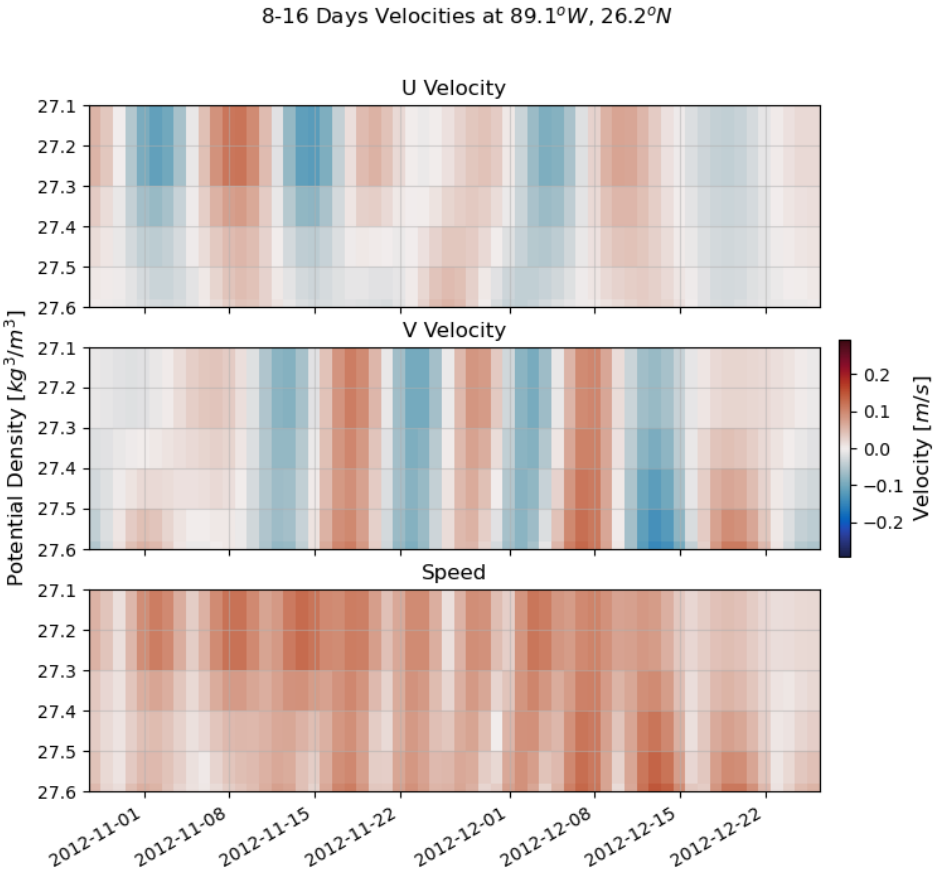

Figure 4.27: The temporal evolution of the velocity vertical profile at a chosen spot shown in the title (89.1°W, 26.2°N), the x-axis is time, and the y-axis is potential density layers. The top panel is the zonal velocity u, the middle panel is the meridional velocity v, and the bottom panel is the speed $\sqrt{u^2 + v^2}$.

In Figures 4.28 and 4.29, case 13 in the NA simulation is shown as a consequence of two

combined MRG waves from the Mississippi Fan and the Yucatan Shelf. Since there are two waves having similar amplitudes, the 2D FFT cannot extract their features as clearly as in case 6. Still, the most outstanding zonal wavelengths are around 200 km. The 2D FFT also recognizes meridional wavenumbers due to the snapshot meridional distribution of these waves and the meridional propagation along the Florida Escarpment. Comparing the three days difference between 2016-10-05 (shading colors) and 2016-10-02 (colored contours), the two waves between the shedded LCE and the LC primarily propagate to the west.

The vertical profiles at the same location of case 13 show similar features as in case 6, the amplitude is mainly controlled by the meridional velocity v, and the zonal velocity u shows a bottom leading phase. The waves in case 6 are also stimulated during the final separation of LCE and dissipate when the LC retract to the next LCE shedding event.

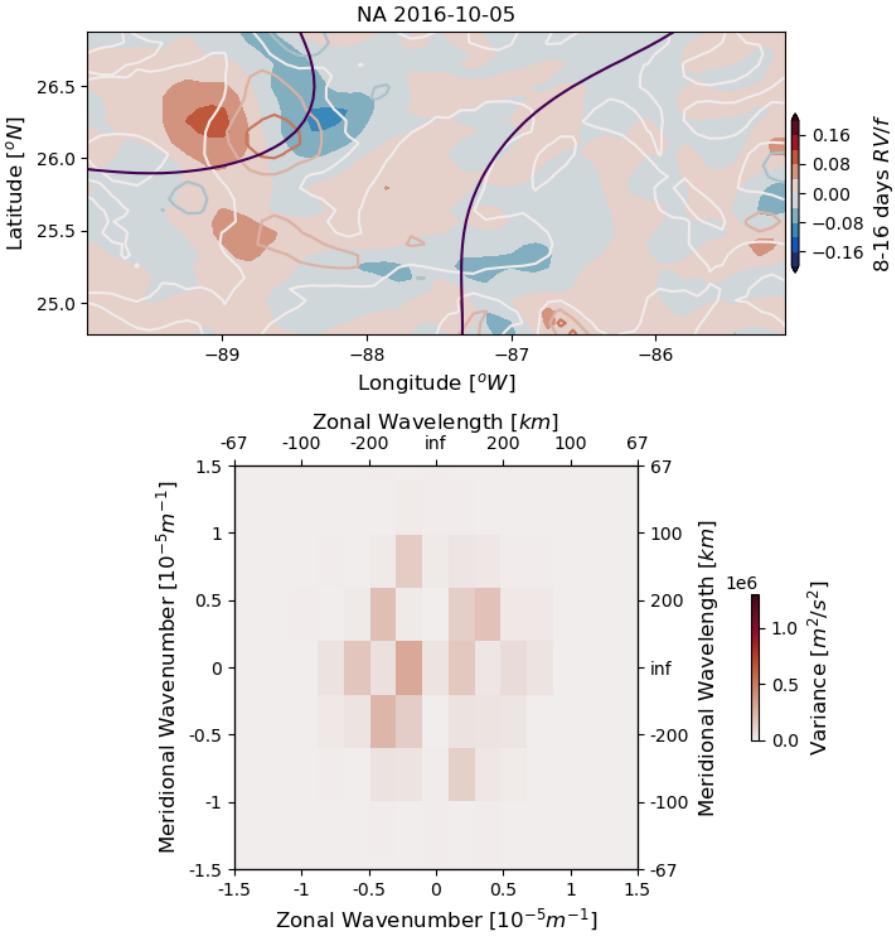

Figure 4.28: The top panel shows the normalized relative vorticity calculated from the 8-16 days band-pass filtered velocities in the selected region of NA simulation on the 27.5 kg/m^3 σ_θ layer, the shading colors indicate the relative vorticity at the selected time shown in the title (2016-10-05). The colored contours present the relative vorticity three days before the chosen time (2016-10-02), and the purple contour shows the distribution of 17 cm SSH at the chosen time (2016-10-05). The bottom panel presents the corresponding spatial FFT of $u + iv$ at the chosen time (2016-10-05).

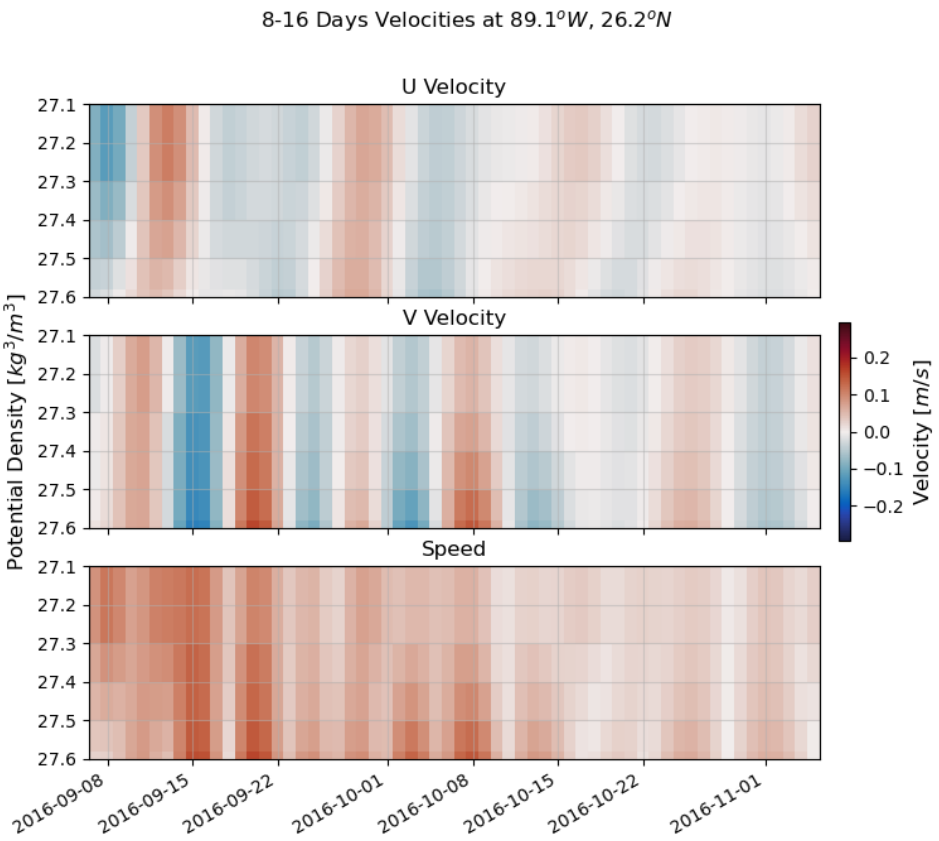

Figure 4.29: The temporal evolution of the velocity vertical profile at a chosen spot shown in the title (89.1°W, 26.2°N), the x-axis is time, and the y-axis is potential density layers. The top panel is the zonal velocity u, the middle panel is the meridional velocity v, and the bottom panel is the speed $\sqrt{u^2 + v^2}$.

The LCEs shedding events 2, 4, 7, 8, and 14 in NA simulation and events 3 and 4 in the SLAT simulation are identified as the second group of separations, which are more complex cases. This group of separations shows the combination of the stimulated MRG waves and some meridionally propagating features, which are not regular MRG waves. Case 7 in the NA simulation clearly shows the combined contribution of different regions during different periods in Figures 4.30 to 4.33.

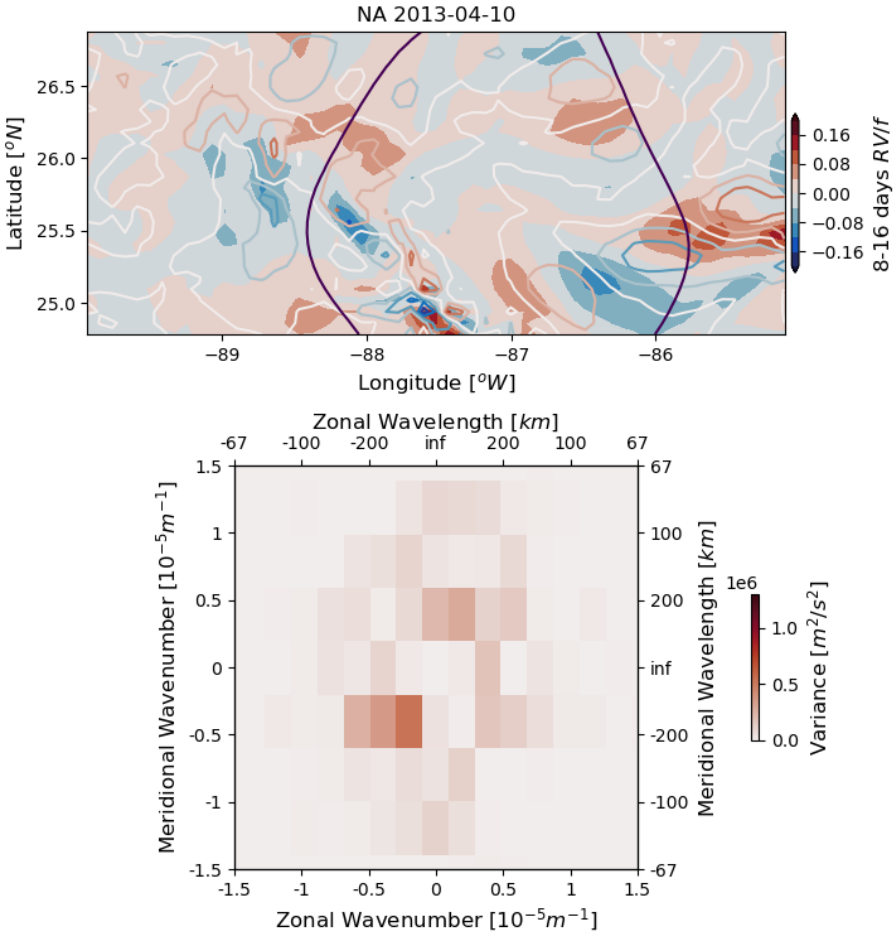

Figure 4.30: The top panel shows the normalized relative vorticity calculated from the 8-16 days band-pass filtered velocities in the selected region of NA simulation on the 27.5 kg/m^3 σ_θ layer, the shading colors indicate the relative vorticity at the selected time shown in the title (2013-04-10). The colored contours present the relative vorticity three days before the chosen time (2013-04-07), and the purple contour shows the distribution of 17 cm SSH at the chosen time (2013-04-10). The bottom panel presents the corresponding spatial FFT of $u + iv$ at the chosen time (2013-04-10).

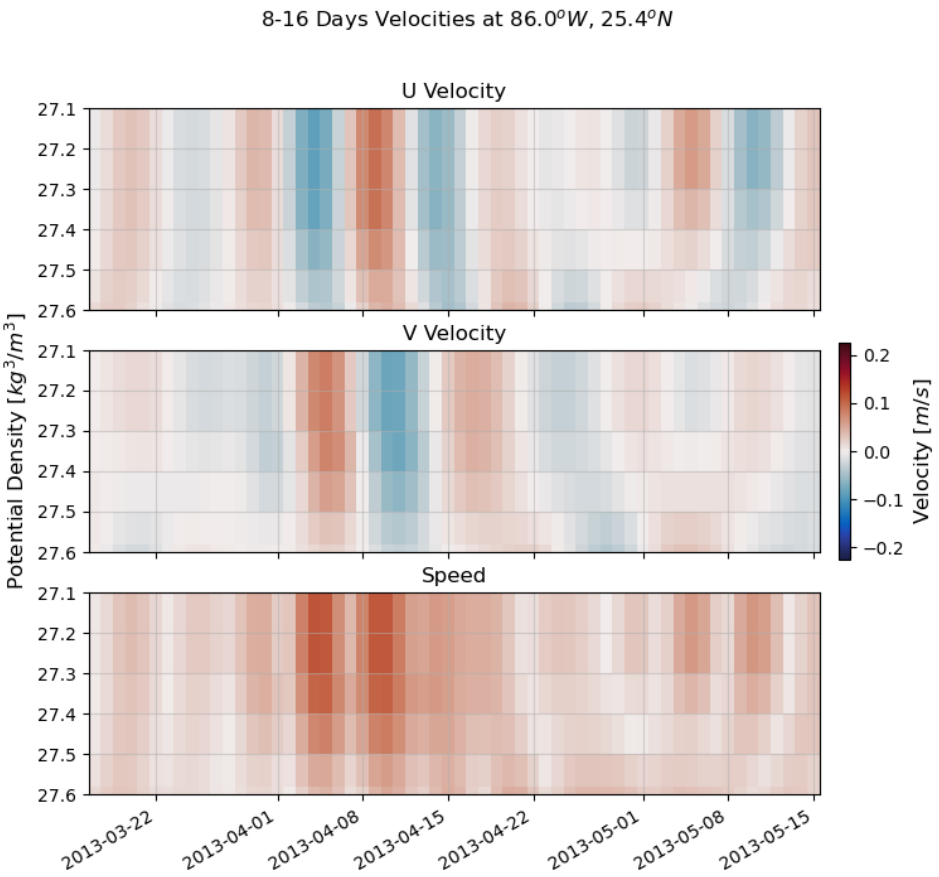

Figure 4.31: The temporal evolution of the velocity vertical profile at a chosen spot shown in the title (86°W, 25.4°N), the x-axis is time, and the y-axis is potential density layers. The top panel is the zonal velocity u, the middle panel is the meridional velocity v, and the bottom panel is the speed $\sqrt{u^2 + v^2}$.

Figures 4.30 and 4.31 present the preparation period of case 7 in the NA simulation. The MRG wave from the Florida Escarpment initializes the curve and large meander of the LC east branch. A southward feature also contributes to this initialization from the Mississippi Fan. In this case, the u and v velocities have similar contributions to the amplitude around the center point of the MRG wave from the Florida Escarpment. The vertical structure of this wave in the eastern region is not as same as in the western part. In the meandering initialization period of case 7, the bottom

of LCS shows a lagging phase after the MRG wave passes through. The final separation occurs around three months later, accompanied by the MRG wave coming from the Yucatan Shelf shown in Figures 4.32 and 4.33.

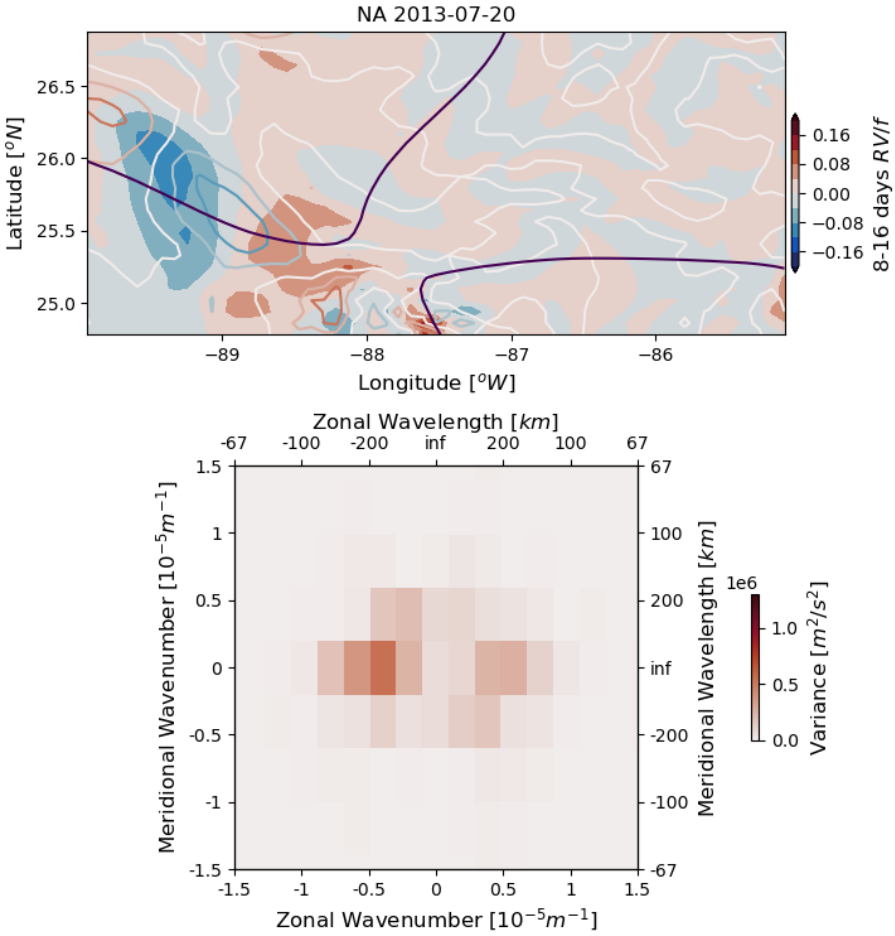

Figure 4.32: The top panel shows the normalized relative vorticity calculated from the 8-16 days band-pass filtered velocities in the selected region of NA simulation on the 27.5 kg/m^3 σ_θ layer, the shading colors indicate the relative vorticity at the selected time shown in the title (2013-07-20). The colored contours present the relative vorticity three days before the chosen time (2013-07-17), and the purple contour shows the distribution of 17 cm SSH at the chosen time (2013-07-20). The bottom panel presents the corresponding spatial FFT of $u + iv$ at the chosen time (2013-07-20).

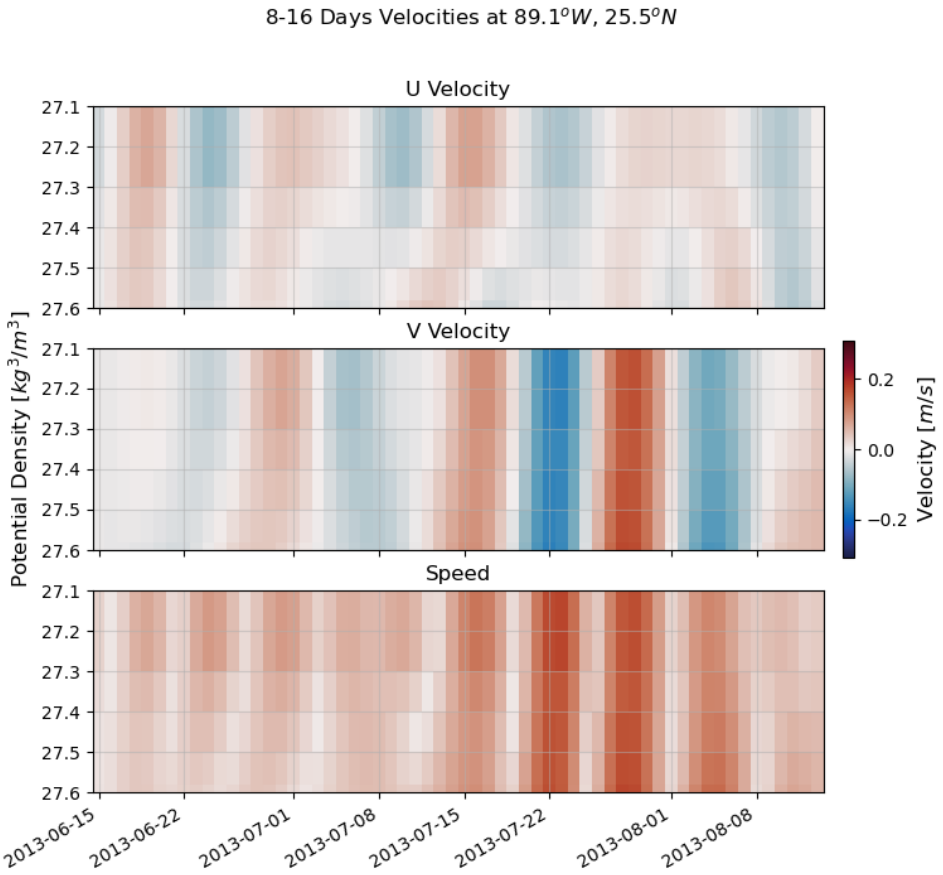

Figure 4.33: The temporal evolution of the velocity vertical profile at a chosen spot shown in the title (89.1°W, 25.5°N), the x-axis is time, and the y-axis is potential density layers. The top panel is the zonal velocity u, the middle panel is the meridional velocity v, and the bottom panel is the speed $\sqrt{u^2 + v^2}$.

During the final separation of case 7 in NA simulation, the MRG wave is stimulated from the Yucatan Shelf. Its vertical structure temporal evolution around the center point presents a bottom leading phase of the zonal velocity u right before this MRG wave is generated. Like the features of the first group, the meridional velocity v dominates its amplitude.

The features of MRG wave shown in the cases of SLAT simulation are not as straightforward as in the NA simulation due to the assimilative processes of SSH and SST. Case 2 in the SLAT

simulation also contains a few features of the second group, which refers to the observations being more complex than the NA simulation. Therefore, all the chosen cases are from the NA simulation to highlight the MRG waves. Still, the 8-16 days band MRG waves primarily contribute to the LCEs shedding events in all R-CESM simulations, and similar features are observed from most mooring stations.

4.5.2 Five Scenarios of MRG Waves

Five scenarios of MRG waves are sorted via their locations and pathways. There are two scenarios from the Yucatan Shelf, one scenario from the Florida Escarpment, one scenario from the Mississippi Fan, and one quiescent scenario. The first scenario appears during most early intrusion of the LC and LC retract after LCEs separations. The second scenario presents the further penetration of the LC. The third scenario shows the initialization of strong meandering of the LC or the LC retract, depending on the position of LCS. The fourth scenario is related to the final separation of a deep penetrated LC. The last scenario is a quiescent LCS with no significant wave trains. The five scenarios are named by the stimulated locations: 1. East Yucatan Shelf Scenario (EYSS), 2. West Yucatan Shelf Scenario (WYSS), 3. West Florida Escarpment Scenario (WFES), 4. Mississippi Fan Scenario (MFS), and 5. the Quiescent Scenario (QS). The details and other features are shown in Table 4.1.

The EYSS contributes to the interfering of LC. The feature of this scenario is the propagating wave trains from the east side of the Yucatan Shelf around the edge of the LC defined by the 17 cm SSH. This scenario occurs during the early intrusion of the LC when the LC starts extending into the GoM and interacts with the Yucatan Shelf. These MRG waves contribute to interfering the LC from further penetration. While the final separation happens, these wave trains can hold the retracting LC in the south region, prohibiting the reattachment of the LC and separated LCE. Therefore, the EYSS indicates the start and end of most LCEs shedding events. Figures 4.34 and 4.35 present the EYSS of the same LCE shedding event at the beginning and end, which is the same case shown in Figure 4.26.

In Figure 4.34, the wave train is stimulated from the east Yucatan Shelf along the LC. This wave

Table 4.1: Details of different scenarios of MRG Waves. The occurrence in the brackets is the case that leads to an LCE separation within 30 days after the dissipation of the wave trains. The percentage is the ratio between the occurrence that leads to the LCE separation and the total occurrence.

Scenario	Scenario Name	Wave Train Pathway	LC Position	Occurrence	Percentage
1	EYSS	East Yucatan Shelf ↓ around the LC	Early Intrusion or Retracted	28(8)	28.6%
2	WYSS	West Yucatan Shelf ↓ to the West	West Penetrating	25(16)	64%
3	WFES	West Florida Escarpment ↓ to the West	East Extended or Retracted	31(5)	16.1%
4	MFS	Mississippi Fan ↓ to the West	West Penetrated	25(18)	72%
5	QS	None	Between Intrusion and Extension	N/A	N/A

train slows the further extension of the LC for a few weeks. After the dissipation of the wave train from EYSS, the LC rapidly penetrates into the western region, accompanied by the wave trains from WYSS, as shown in Figure 4.35. The EYSS at the end of this LCE shedding event is shown in Figure 4.36. The wave train in the east is stimulated from the east Yucatan Shelf, propagating along the LC and holding the retracted LC in the south region. The occurrence of the EYSS at the end of LCEs shedding events can prohibit the LCS from reattachments.

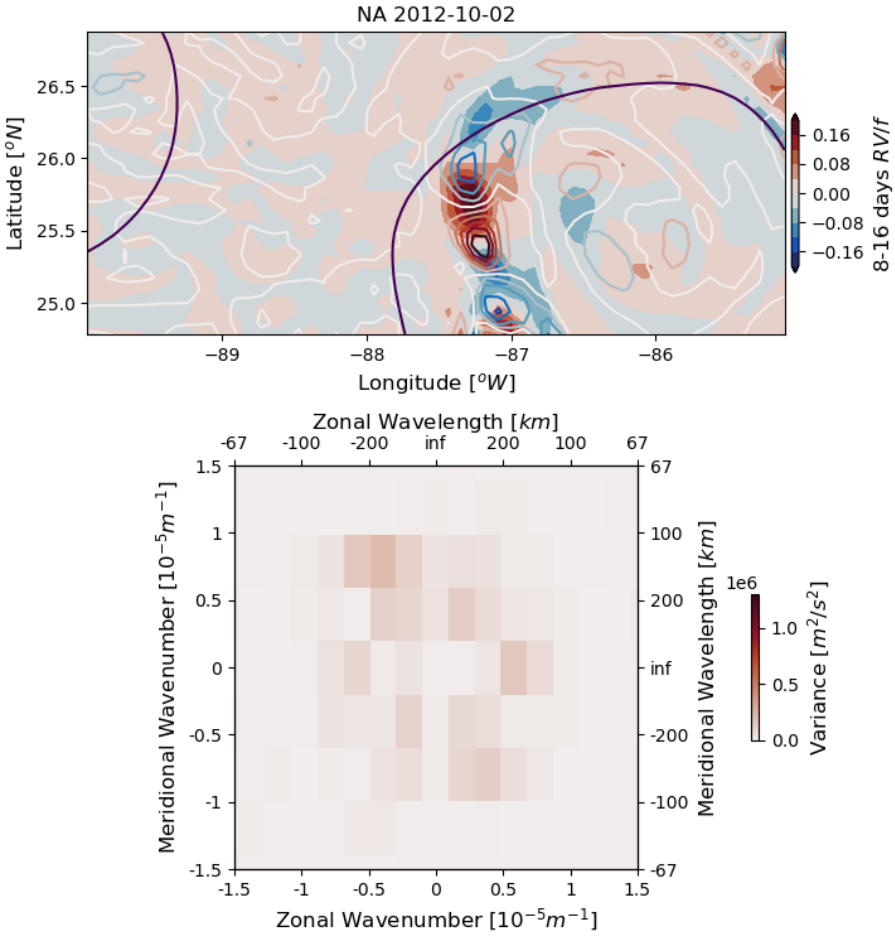

Figure 4.34: The top panel shows the normalized relative vorticity calculated from the 8-16 days band-pass filtered velocities in the selected region of NA simulation on the 27.5 kg/m^3 σ_θ layer, the shading colors indicate the relative vorticity at the selected time shown in the title (2012-10-02). The colored contours present the relative vorticity three days before the chosen time (2012-09-29), and the purple contour shows the distribution of 17 cm SSH at the chosen time (2012-10-02). The bottom panel presents the corresponding spatial FFT of $u + iv$ at the chosen time (2012-10-02).

After extending into the GoM, the LC can further penetrate to the northwest or northeast, leading to the WYSS or WFES, respectively. When the LC extends to the northwest, the stimulated MRG waves from the west Yucatan Shelf accompanies the extending LC into the western region, as shown in Figure 4.35. Then, if the WYSS meets the MFS under the extended LC, the final separation (Figures 4.26 and 4.36) would occur by the contributions of the westward wave trains

from the Mississippi Fan and the west Yucatan Shelf. Figure 4.28 shows the consequence of this joint situation from another LCE shedding event.

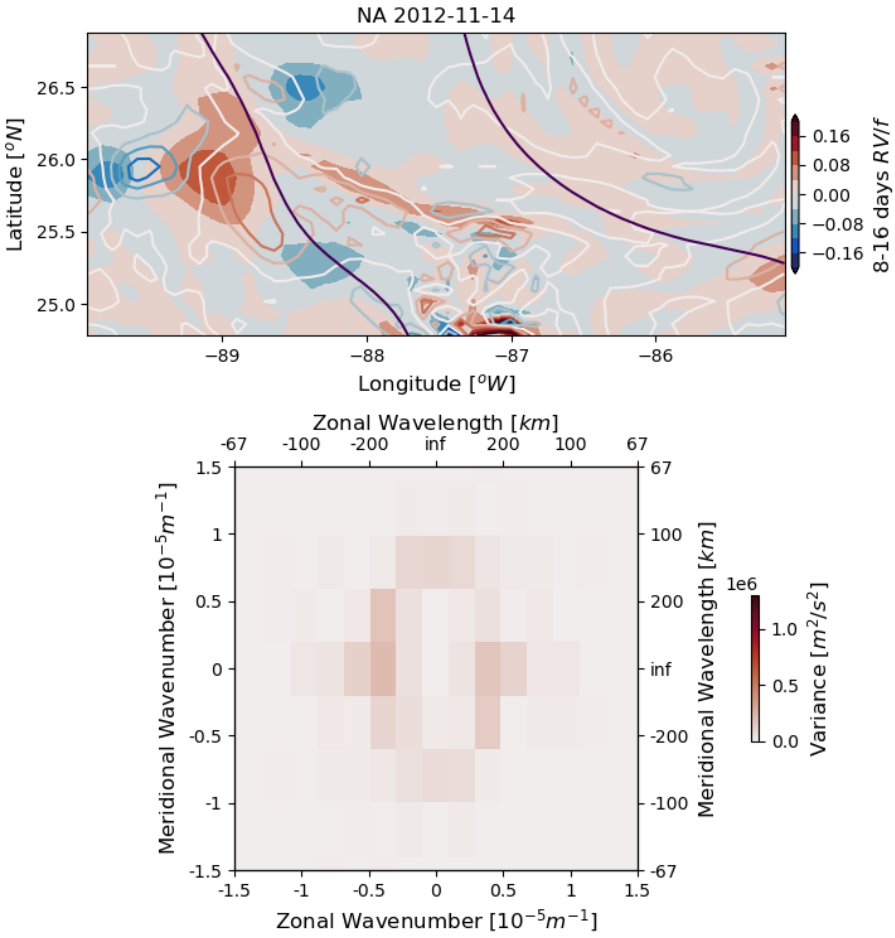

Figure 4.35: The top panel shows the normalized relative vorticity calculated from the 8-16 days band-pass filtered velocities in the selected region of NA simulation on the 27.5 kg/m^3 σ_θ layer, the shading colors indicate the relative vorticity at the selected time shown in the title (2012-12-02). The colored contours present the relative vorticity three days before the chosen time (2012-11-29), and the purple contour shows the distribution of 17 cm SSH at the chosen time (2012-12-02). The bottom panel presents the corresponding spatial FFT of $u + iv$ at the chosen time (2012-12-02).

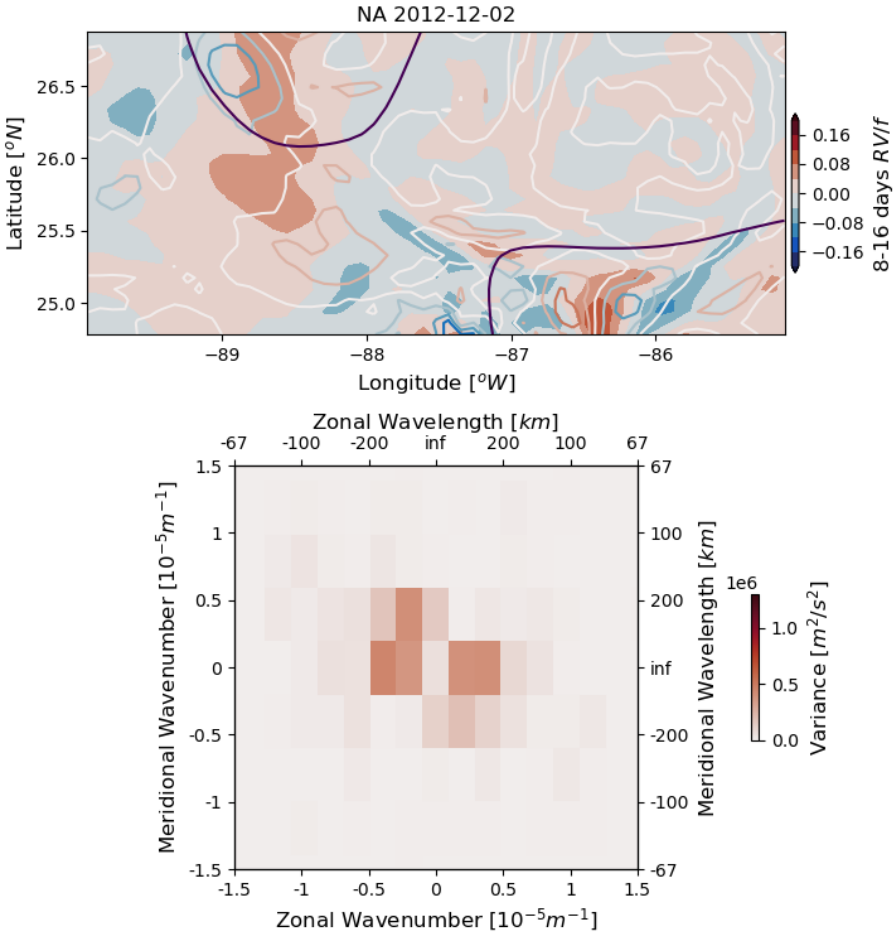

Figure 4.36: The top panel shows the normalized relative vorticity calculated from the 8-16 days band-pass filtered velocities in the selected region of NA simulation on the 27.5 kg/m^3 σ_θ layer, the shading colors indicate the relative vorticity at the selected time shown in the title (2012-11-14). The colored contours present the relative vorticity three days before the chosen time (2012-11-11), and the purple contour shows the distribution of 17 cm SSH at the chosen time (2012-11-14). The bottom panel presents the corresponding spatial FFT of $u + iv$ at the chosen time (2012-11-14).

The northwest extended LC will lead to the WFES, shown in Figure 4.30. Generally, the wave trains from WFES can squeeze the east branch of the LC and intensify its meandering, which contributes to the LC eastward penetration and separation. The wave trains of WFES can also contribute to the LCEs final separation by interfering the retracted LC in the south around ~25°N, shown in Figure 4.37. The WFES is similar to the necking-down process, which is trying to pass

through the LC and pinch the LCE from the LC.

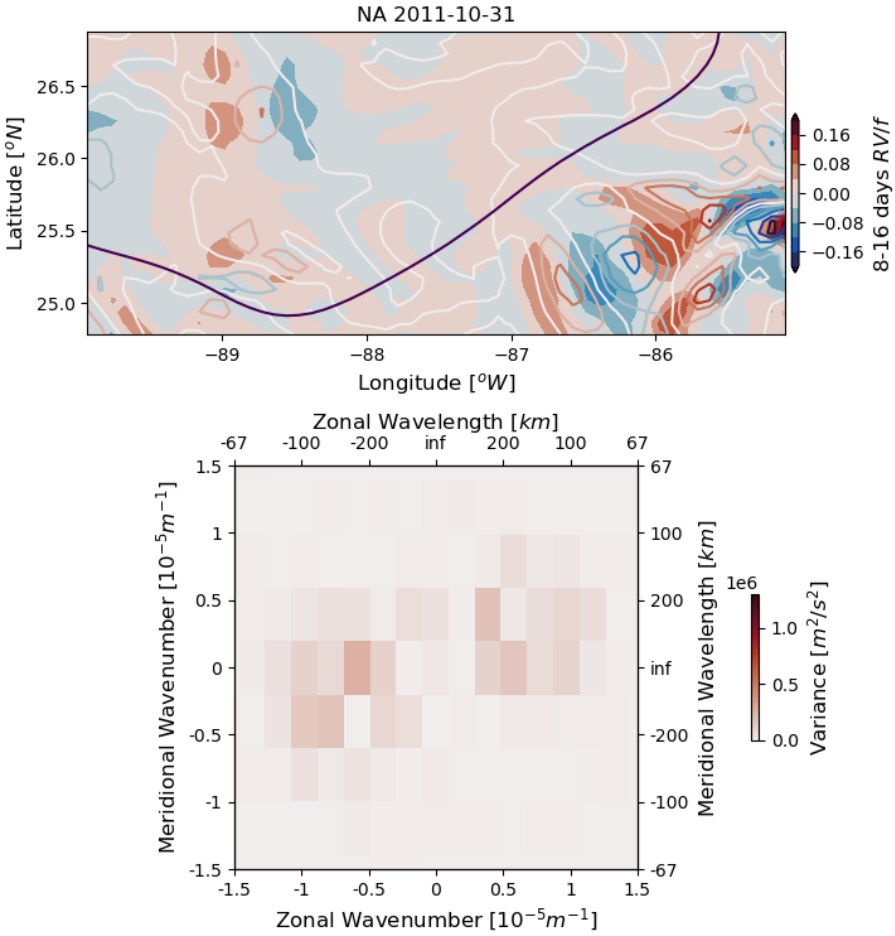

Figure 4.37: The top panel shows the normalized relative vorticity calculated from the 8-16 days band-pass filtered velocities in the selected region of NA simulation on the 27.5 kg/m^3 σ_θ layer, the shading colors indicate the relative vorticity at the selected time shown in the title (2011-10-31). The colored contours present the relative vorticity three days before the chosen time (2011-10-28), and the purple contour shows the distribution of 17 cm SSH at the chosen time (2011-10-31). The bottom panel presents the corresponding spatial FFT of $u + iv$ at the chosen time (2011-10-31).

Figures 4.34 to 4.36 and 4.26 show the same LCE shedding event from intrusion to the extension and final separation, which includes the WYSS, the EYSS, and the MFS. The WFES is shown in Figures 4.30 and 4.37, presenting the squeezing and interfering scenarios in the necking-down

region. The QS is a transition scenario between different LCEs shedding events and different LC states. The MFS is always after the WYSS, but their wave trains are not merged together every time, as in case 6. The MFS shows the most contribution to the LCEs final separations, and the WYSS can make the MFS more effective. The EYSS is more likely at the early intrusion of the LC. When the EYSS occurs after separations, it can contribute to the final LCEs separations by interfering the retracted LC from reattachments. The WFES seems like the necking-down process, but it primarily contributes to the initialization of the LC strong meandering, not separations. Therefore, the joint area of WYSS and MFS is the critical region for the LCEs separations.

A temporally trained six-neuron SOM model also identifies the impacts of WYSS, MFS, and WFES. Patterns 5 and 6 in Figure 4.38 present the different scenarios. The combination of WYSS and MFS is extracted by pattern 5, and pattern 6 captures wave trains in the eastern part related to the EYSS and WFES. Patterns 5 and 6 have larger amplitude and shorter lasting periods compared to the other four patterns, and they occur around the LCEs shedding events defined by the traditional 17 cm SSH. The first four patterns are more like the high-frequency variations under the LCS as the QS scenario. In this scenario, the primary signals are not the wave trains stimulated by the interaction between the LCS and sharp topography. Therefore, the SOM cannot capture enough outstanding features most of the time, the BMU changes among patterns 1 to 4 as one group in Figure 4.38.

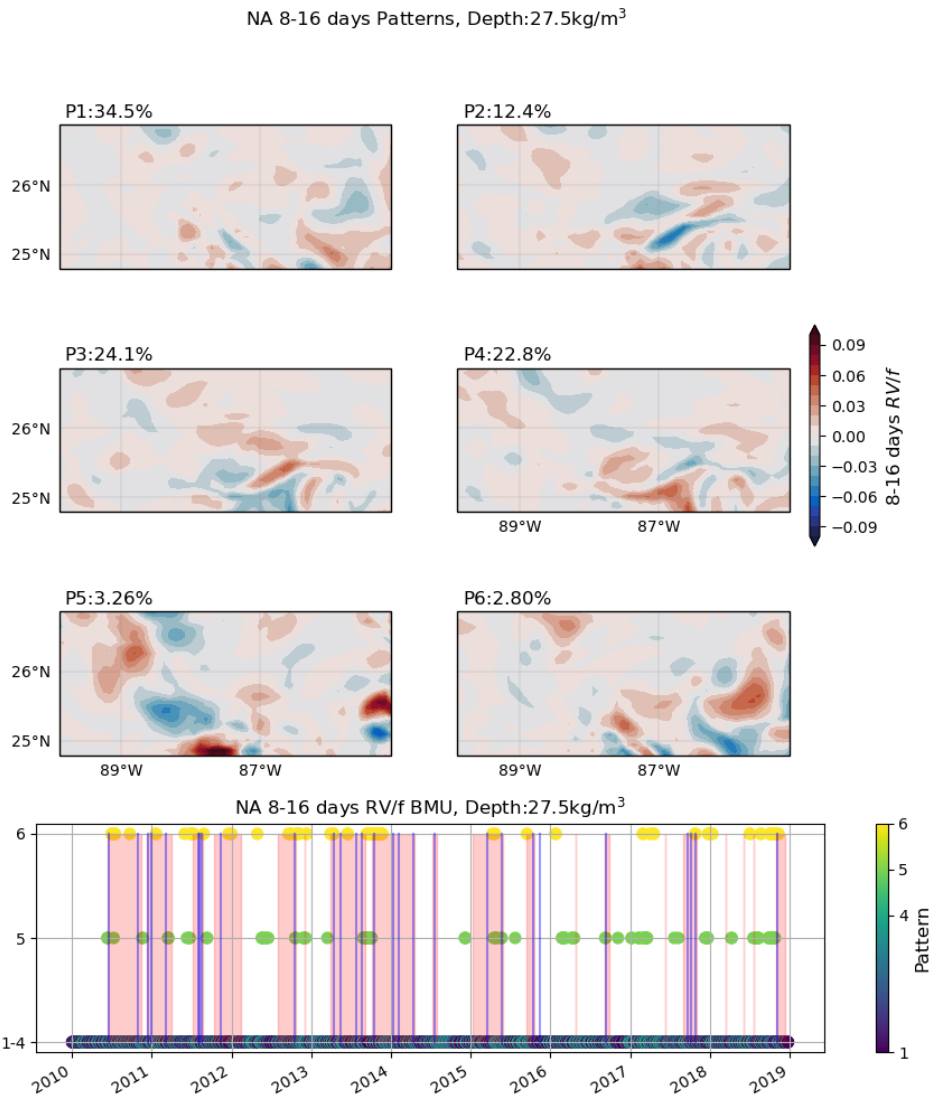

Figure 4.38: The top six panels present the SOM-captured primary spatial patterns of the 8-16 days band-pass filtered normalized relative vorticity in the free-run simulation. The frequency of occurrence is shown as the subtitles of each pattern. The shading color indicates the 8-16 days band-pass filtered normalized relative vorticity reconstructed from the SOM weighted vectors. In the bottom panel, the colored dots show the BMU of the 8-16 days band-pass filtered normalized relative vorticity in the NA simulation. The shading areas indicate all the LCEs shedding events from their first separation to their final separation, and the vertical blue lines present the reattachment occurring during each LCEs shedding event.

4.5.3 West Necking-down Region

The traditional necking-down region mainly indicates the break up of the 17 cm SSH rather than the potential propagation of LCEs. Since the 8-16 days variances contribute to the LCEs shedding events, the integrated 8-16 days band kinetic energy at 27.5 kg/m^3 σ_θ layer is calculated via the 40-hour low-pass filtered daily subsampled free-run simulation and shown in Figure 4.39. The regions with higher 8-16 days band kinetic energy are consistent with the previous three areas: the Mississippi Fan, the Yucatan Shelf, and the West Florida Escarpment. The higher 8-16 days band kinetic energy region connects the Mississippi Fan to the Yucatan Shelf, which seems like a necking-down region for the LCEs final separations in the west area. Based on the WYSS and MFS scenarios, the extended LC is about to separate when the higher 8-16 days band kinetic energy region is stimulated by the wave trains.

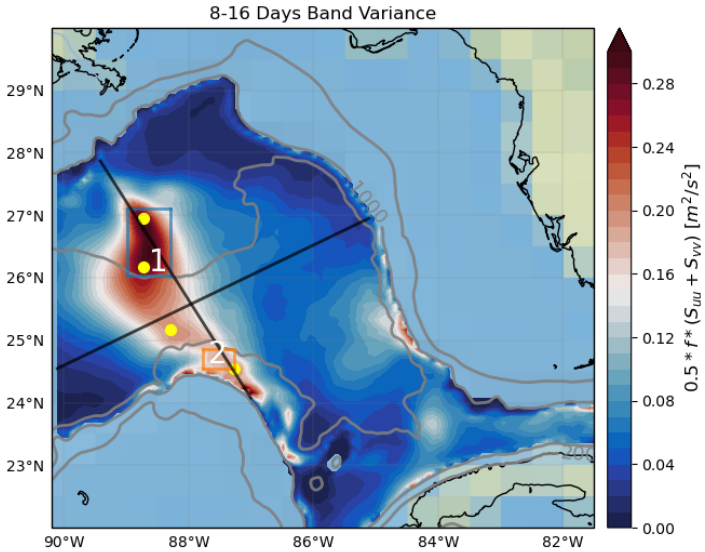

Figure 4.39: The 8-16 days band kinetic energy at 27.5 kg/m^3 σ_θ layer, shown by the 8-16 cpd integrated variance-preserving spectra. The shading color indicates the $0.5 \times f \times (S_{uu} + S_{vv})$, f is the Coriolis parameter, and S_{uu}, S_{vv} are the PSD of u and v velocity. The gray contours present the 200 m, 1000 m, and 3000 m isobath. The black lines show the two profiles in Figure 4.40. The four yellow dots are the locations of the four spectra in Figure 4.41. The blue box is the Mississippi Fan wavelet region and the orange box is the Yucatan Shelf wavelet region for Figure 4.42.

The vertical structure of the 8-16 days band kinetic energy is shown in Figure 4.40. In the Mississippi Fan area, the lower-layer 8-16 days band kinetic energy is dramatically higher than in other regions. The lower layer of the Yucatan Shelf also presents a relatively higher 8-16 days band kinetic energy than the deep GoM region. Therefore, these wave trains propagate from the lower layer, being stimulated by the interaction between the LC and the sharp topography.

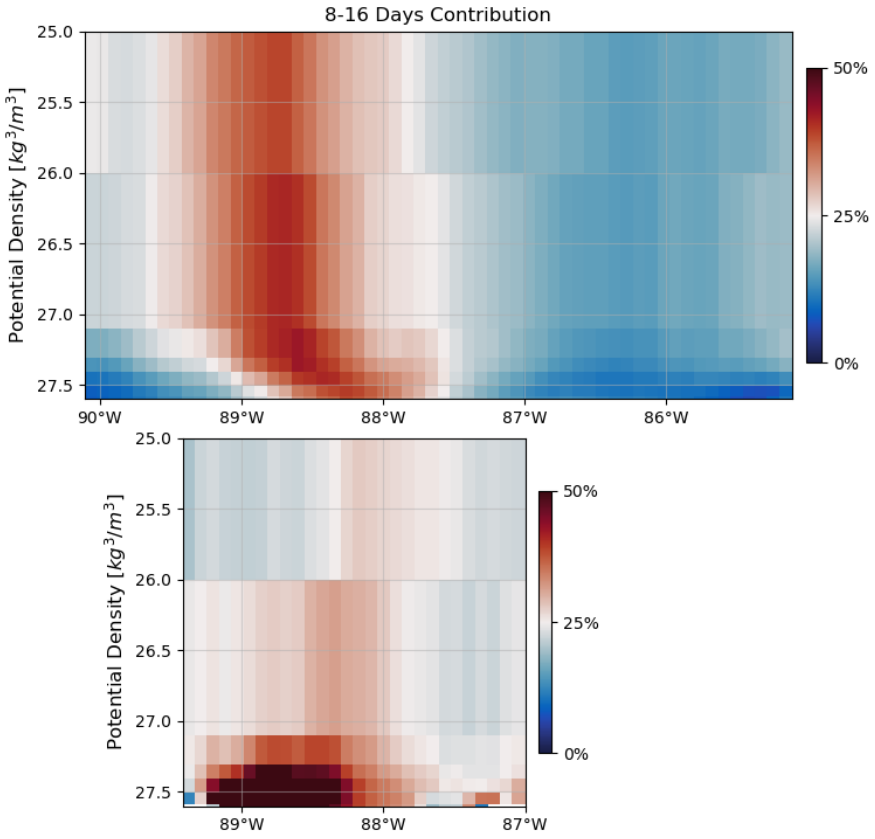

Figure 4.40: The vertical structure of the contribution of 8-16 days band kinetic energy to the total kinetic energy at full frequencies along the two sections in Figure 4.39. The top panel is the zonal section, and the bottom panel is the meridional section. The shading colors display the percentage of the 8-16 days band kinetic energy to the total kinetic energy.

From north to south at 27.5 kg/m^3 σ_θ layer, the percentage of 8-16 days band kinetic energy decreases from the Mississippi Fan to the deep area and increases approaching the Yucatan Shelf.

The Mississippi Fan area is dominated by the 8-16 days band variance, and the deep GoM regions have a relatively higher lower-frequency variance.

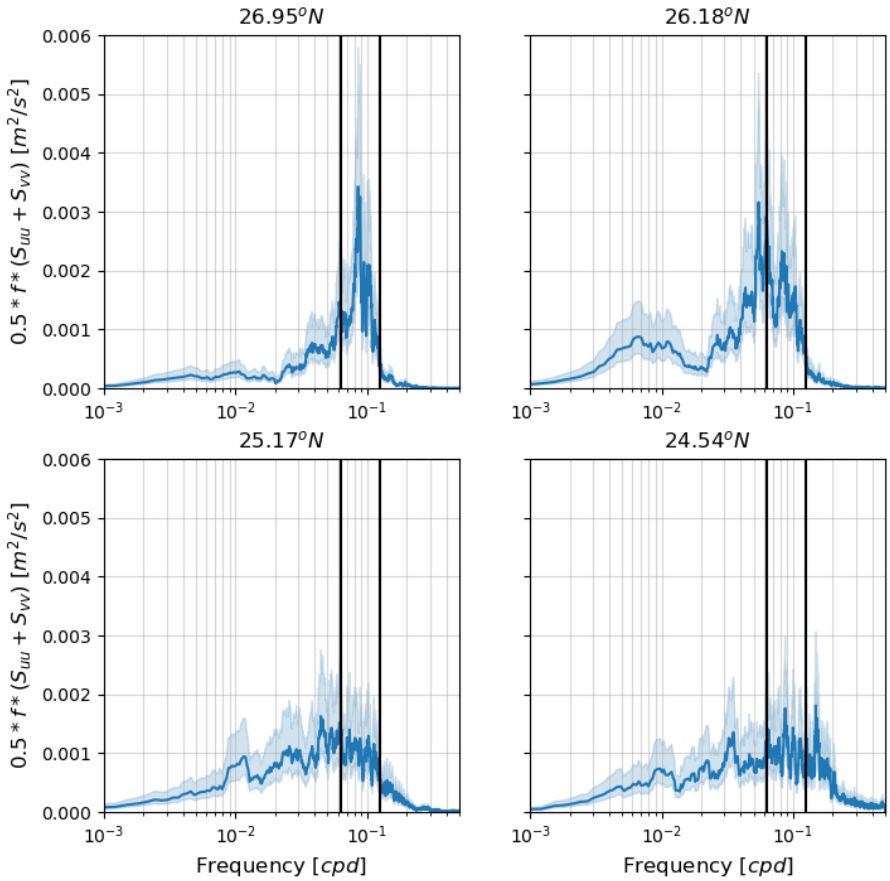

Figure 4.41: The variance-preserving spectra of kinetic energy at the four spots in Figure 4.39, their locations are indicated by their latitudes on each title. The spectra are calculated as $0.5 \times f \times (S_{uu} + S_{vv})$, f is the Coriolis parameter, and S_{uu}, S_{vv} are the PSD of u and v velocity. The shading color is the 95% confidence intervals. The two vertical lines presents the interval between 8-16 days band.

The occurrence of WYSS and MFS identified by the wavelets of regional averaged $u + v$ in Figure 4.42 is similar to the occurrence counted in Table 4.1. The 8-16 days scale-averaged variance can partially indicate the LCEs shedding events. When the 8-16 days scale-averaged

variance time series of two regions reach their peaks, the LCS is around the separations. Rapid separations in the middle of 2014, 2016, 2017, and 2018 are around the 8-16 days scale-averaged variance peaks of both regions as well.

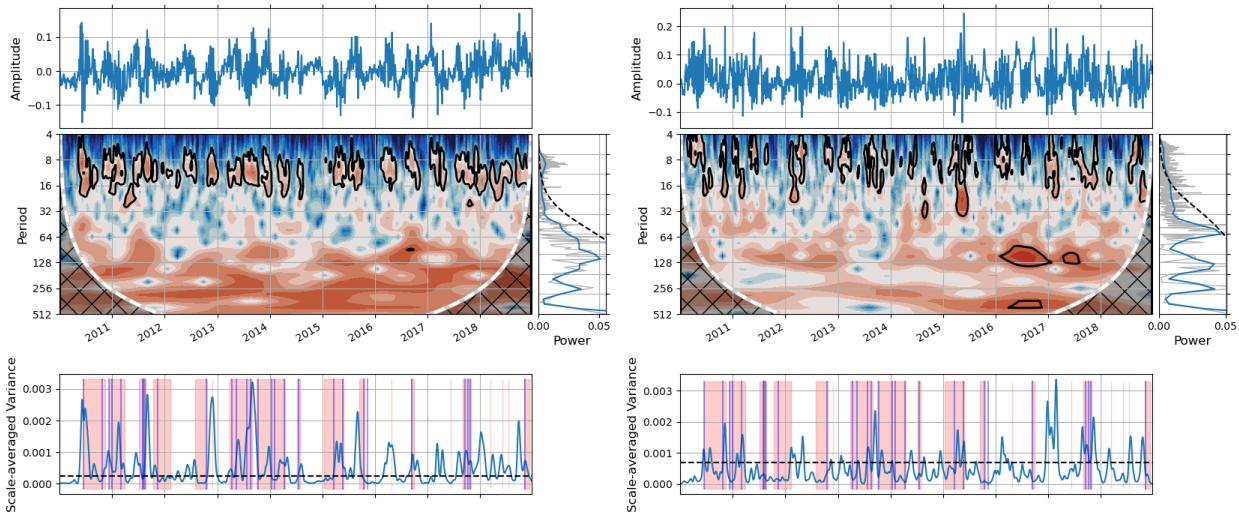

Figure 4.42: The wavelet analysis of regional averaged $u + v$ from NA simulation at 27.5 kg/m^3 σ_θ layer of region 1 (left) and region 2 (right) in Figure 4.39. The left part is the Mississippi Fan region, and the right part is the Yucatan Shelf region. The top panel shows the original input time series, the right panel in the middle is the wavelet transform, the left panel in the middle present the time-averaged power at different period in the unit of days, and the bottom panel is the temporal evolution of 8-16 days scale-averaged variance. The shadow region in the wavelet transform indicates the values below the 95% significant level. The dashed line in the bottom and right middle panels is the 95% significant level. The gray line in the right middle panel is the power via the fast Fourier transform. The shading red colors in the bottom panels are the LCEs shedding events defined by the 17 cm SSH.

Like the indicator metric from the five regions, these two 8-16 days scale-averaged variance time series do not fully follow the LCEs separations defined by the 17 cm SSH. These scenarios of MRG waves still need other information to predict the likelihood of LCEs separations. Even so, the west necking-down region is a critical area for the LCEs separations. The intensity of 8-16 days band kinetic energy of this west necking-down region can help to establish a more comprehensive

prediction of the LCEs shedding events. When the extended LC is about to shed the LCE into the western GoM, the MRG waves from the Mississippi Fan and west Yucatan Shelf occupy the west necking-down region from the bottom of the LCS. This LCE-separation-accompanied dynamical phenomenon in the west necking-down region indicates the end of the LCEs shedding events.

4.6 Discussion

The wavelet analysis demonstrates the capability to represent the LCEs shedding events around the 32-128 days band. Some higher frequency bands are stimulated around the LCEs shedding events. The highlighted 8-16 days band variance is selected to indicate the dynamical processes related to the LCEs separations rather than the separation process itself.

The temporal evolution of the 8-16 days scale-averaged variance shows narrow local peaks that may be akin to triggering processes, not culminating EKE during the LCEs shedding events. The dynamical processes of the 8-16 days scale-averaged variance are the MRG waves, and many different processes are checked and compared with it. It does not show any clear relationship with the energy conversion terms calculated via temperature or relative height, and the horizontal velocity shear is not correlated with it as well.

The major features we get are from the 8-16 days band-pass filtered flow field, and there are MRG waves along the large 8-16 days scale-averaged variance areas. These MRG waves perform like a trigger of the LCEs separation, and they keep propagating along the same pathway and increasing the 8-16 days scale-averaged variance of that area. If the LC necking region is above this pathway, the LCEs will like to be cut and pushed by these MRG waves at the bottom. As relatively high-frequency signals, the pathway of the MRG waves can vary between different selected regions. The most common LC cutting paths are from region 4 to north (Figure 4.18) and regions 2 and 3 to west. There are also 8-16 days propagating features can travel around the LC from region 4 through region 2 to region 3. The large 8-16 days scale-averaged variance presents the interface between relatively stationary eddies as well. Hence, combing the wavelet scale-averaged time series in each region with the position of upper-layer LC may be a better indicator of the LCEs shedding events than the combined indicator metric.

The fundamental idea of the MRG waves that contribute to the LCEs separations is shown in Figure 4.43 as a schematic diagram. The three arrows indicate the approximate pathway of the MRG waves from three scenarios: MFS, WYSS, and WFES. The first group of LCEs shedding events are accompanied by the MRG waves shown as arrows a and b, which are from the Mississippi Fan and the Yucatan Shelf. Arrow c shows the MRG waves coming from the Florida Escarpment, contributing to the initialization of the LC meandering. The second group of LCEs shedding events is dominated by the combined consequences of the MRG waves from different regions and some other meridional propagating features, which are more complex events.

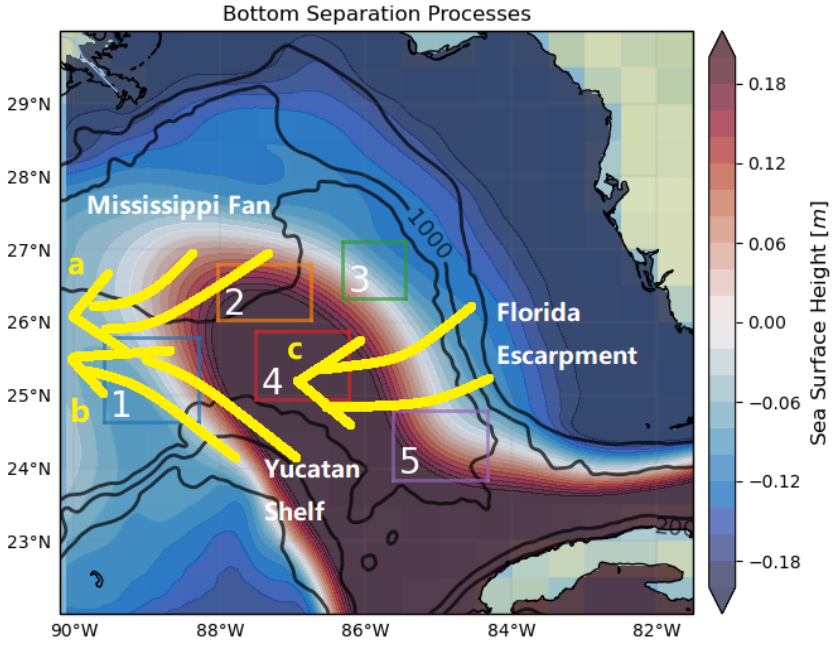

Figure 4.43: Schematic diagram of the approximate pathway of MRG waves coming from three regions, arrow a is from the Mississippi Fan, arrow b is from the Yucatan Shelf, and arrow c is from Florida Escarpment. The black contours are the 200 m, 1000 m, and 3000 m isobaths, and the shading colors present the 9-year averaged SSH from the free-run simulation. The five chosen index regions are shown in the same color as Figure 4.8.

Combing the deep observations from the five regions and the west necking-down region with

the SSH on the surface showing the location of LC, a more comprehensive prediction of the LCEs shedding events can be archived. The wave trains from the Mississippi Fan and west Yucatan Shelf can indicate the separation of LCEs via their peaks of the wavelets 8-16 days scale-averaged variance in the west necking-down region. This newly developed LCE-separation indicator changes based on different LCEs shedding events, which is not a constant artificial threshold for all cases. The description of deep structure can help improve the understanding of LCS dynamics. The more detailed dynamical processes related to this phenomenon still need to be addressed in future works.

5. CONCLUSIONS AND FUTURE WORK

5.1 Conclusions

The free-run R-CESM simulation presents the capability to reconstruct the mean state of the LCS, whose structure is similar to the observations. An SSHA index is defined by the temporal evolution of the regional averaged SSHA in the maximum SSH standard deviation region to indicate the occurrence of the LCEs shedding events. Comparing the SSHA index between the free-run R-CESM simulation and the multiple satellites SSHA data, the frequency of LCEs shedding events is about two times higher in the R-CESM model. This higher LCEs shedding occurrences is the consequence of the more energetic upper layer in the R-CESM simulation. Although the upper layer is more energetic, the lower layer in the R-CESM simulation is more stable than the mooring observations. The TS structure of the R-CESM is close to the mooring observations from LC Dynamics Experiments 2009-2011, with a slightly warmer top layer and cooler bottom layer. Except for the higher separation frequency in the free-run simulation, some numerical instabilities occur from the sharp topography across the entire model domain, causing other biases. Therefore, data assimilation of satellite products is applied to constrain the model dynamics closer to the observations. Comparing the SLAT and SLA assimilative simulations, the assimilation of SST data can revise the TS structure via model dynamics. The primary improvement from SSH data assimilation is the temporal and spatial evolution of the LCS. After SSH data assimilation, both simulations offer the four LCEs shedding events similar to the observations, as the assimilated SSH constrains the variance on the surface. Hence, the two assimilative simulations are used for the following characteristic analysis.

In the characteristics extraction, the EOF and SOM methods are applied to the stream function at several targeted depths. The EOF analysis presents the highest LCEs shedding events correlated mode at each depth by comparing the PC time series with the SSHA index time series. Both SLAT and SLA simulations show an anticyclonic eddy under the LC surrounded by cyclonic eddies at

1000 m and 1500 m depths. This feature is consistent with the SOM precursor patterns trained by the free-run stream function at 27.5 kg/m^3 σ_θ layer. Two assimilative runs show similar temporal evolution identified the temporally trained SOM of SSH and stream function from NA simulation. The SSH SOM spatial patterns are sorted as intrusion patterns, growing patterns, detached patterns, and transit patterns. These SSH SOM patterns are ideal for describing the detailed stages on the surface, and its BMU can show the temporal processes of the LCEs shedding events. The stream function at the bottom of the LCS presents some precursor features of the LCEs separations, which is identified by the SOM model temporally trained by the free-run stream function at 27.5 kg/m^3 σ_θ layer. Most features of the LCS from the upper layer can be seen via the distribution of the deep anticyclonic eddy and deep cyclonic eddies. As the precursor patterns lead to the LCEs shedding events more apparent than the SSH patterns, five regions are selected to cover most features of the precursor patterns. In the LCS, a wide range of frequency is highlighted during LCEs shedding events shown by the wavelet analysis. The major frequency of the LCEs separations is around 32-64 days, and higher frequency bands are stimulated by the LC at a wider time range. Therefore, the 8-16 days scale-averaged variance of $u+v$ is selected to initiate the indicator metric. This 8-16 days frequency band can be seen in both in-situ observations and regionally averaged simulations of the five regions.

Because the peaks of 8-16 days scale-averaged variance of $u + v$ perform as MRG waves, the relative position of its pathway to the LC necking region is critical for separation prediction. The indicator metric established in this research is a necessary condition for most LCEs separations, and the situation in the upper layer is still needed to make a comprehensive prediction. Three sources of the MRG waves are found: the Mississippi Fan, the Yucatan Shelf, and the Florida Escarpment. For most LCEs shedding events, these MRG waves are stimulated by the energetic deforming LC via the interactions with the sharp topography before the final separation of the LCEs. The MRG wave is also stimulated during the initialization of the strong LC meandering for some cases. Five scenarios are identified based on the locations and pathways of the wave trains. The west necking-down region is dominated by the wave trains of WYSS and MFS scenarios, which is directly

related to the LCEs separations. The EYSS is during the early intrusion of the LC and at the end of some LCEs shedding events. The WFES contribute to the LCEs shedding events by intensifying the LC meandering and interfering the retracted LC. The QS is the converting scenario between different LCEs shedding events and different LC states. Based on the contribution of 8-16 days band kinetic energy, there is a new critical region being identified as the west necking-down region at the 27.5 kg/m^3 σ_θ layer. The MRG waves passing through this west necking-down region from the Mississippi Fan and west Yucatan Shelf can indicate the separation of LCEs via their peaks of the wavelets 8-16 days scale-averaged variance. This newly developed LCE-separation indicator varies based on the dynamical scenarios of different LCEs shedding events, which is not a constant artificial threshold for all cases like the traditional 17 cm SSH.

Supported by numerical simulations of R-CESM and data assimilation, a new metric is developed to describe the LCEs separations. This new metric is defined by the temporal evolution of 8-16 days scale-averaged variance in the newly defined west necking-down region at the 27.5 kg/m^3 σ_θ layer. The description of deep structure can help improve the understanding of LCS dynamics. The mechanisms behind the interaction between the MRG wave and the LCS are still not well understood. Therefore, there are more works to do to understand the detailed physics of these high-frequency variances below the LCS and related to the LCEs shedding events.

5.2 Future Work

In future works, the first priority is to derive the physics behind these high-frequency variances shown as MRG waves and show the dynamical evidence to sort this mysterious wave into the MRG wave catalogue. A more comprehensive indicator metric will be established to show the different stages of the LCEs shedding events below the LCS without the traditional 17 cm SSH. The longer data sets will be applied to address this problem.

REFERENCES

Athié, G., Candela, J., Ochoa, J., and Sheinbaum, J. (2012). Impact of caribbean cyclones on the detachment of loop current anticyclones. *Journal of Geophysical Research: Oceans*, 117(C3).

Athié, G., Sheinbaum, J., Candela, J., Ochoa, J., Pérez-Brunius, P., and Romero-Arteaga, A. (2020). Seasonal variability of the transport through the yucatan channel from observations. *Journal of Physical Oceanography*, 50(2):343–360.

Baringer, M. O. and Larsen, J. C. (2001). Sixteen years of florida current transport at 27 n. *Geophysical Research Letters*, 28(16):3179–3182.

Batchelor, G. (1967). 1967, an introduction to fluid dynamics. cambridge: Cambridge university press.

Beal, L. M. and Bryden, H. L. (1999). The velocity and vorticity structure of the agulhas current at 32 s. *Journal of Geophysical Research: Oceans*, 104(C3):5151–5176.

Behringer, D. W., Molinari, R. L., and Festa, J. F. (1977). The variability of anticyclonic current patterns in the gulf of mexico. *Journal of Geophysical Research*, 82(34):5469–5476.

Brooks, D. A. (1983). The wake of hurricane allen in the western gulf of mexico. *Journal of Physical Oceanography*, 13(1):117–129.

Bunge, L., Ochoa, J., Badan, A., Candela, J., and Sheinbaum, J. (2002). Deep flows in the yucatan channel and their relation to changes in the loop current extension. *Journal of Geophysical Research: Oceans*, 107(C12):26–1.

Candela, J., Sheinbaum, J., Ochoa, J., Badan, A., and Leben, R. (2002). The potential vorticity flux through the yucatan channel and the loop current in the gulf of mexico. *Geophysical Research Letters*, 29(22):16–1.

Chang, Y.-L. and Oey, L.-Y. (2011). Loop current cycle: Coupled response of the loop current with deep flows. *Journal of Physical Oceanography*, 41(3):458–471.

Chang, Y.-L. and Oey, L.-Y. (2012). Why does the loop current tend to shed more eddies in summer and winter? *Geophysical Research Letters*, 39(5).

Chang, Y.-L. and Oey, L.-Y. (2013). Loop current growth and eddy shedding using models and observations: Numerical process experiments and satellite altimetry data. *Journal of Physical Oceanography*, 43(3):669–689.

Chassignet, E. P., Hurlburt, H. E., Smedstad, O. M., Halliwell, G. R., Wallcraft, A. J., Metzger, E. J., Blanton, B. O., Lozano, C., Rao, D. B., and Hogan, P. J. (2006). Generalized vertical coordinates for eddy-resolving global and coastal ocean forecasts. Technical report, NAVAL RESEARCH LAB STENNIS SPACE CENTER MS OCEANOGRAPHY DIV.

Chelton, D. B. (1983). Effects of sampling errors in statistical estimation. *Deep Sea Research Part A. Oceanographic Research Papers*, 30(10):1083–1103.

Chelton, D. B., DeSzoeke, R. A., Schlax, M. G., El Naggar, K., and Siwertz, N. (1998). Geographical variability of the first baroclinic rossby radius of deformation. *Journal of Physical Oceanography*, 28(3):433–460.

Cho, K., Reid, R. O., and Nowlin Jr, W. D. (1998). Objectively mapped stream function fields on the texas-louisiana shelf based on 32 months of moored current meter data. *Journal of Geophysical Research: Oceans*, 103(C5):10377–10390.

Clarke, A. J. (1983). The reflection of equatorial waves from oceanic boundaries. *Journal of Physical Oceanography*, 13(7):1193–1207.

Crosby, D., Breaker, L., and Gemmill, W. H. (1990). A definition for vector correlation and its application to marine surface winds.

Cushman-Roisin, B., Tang, B., and Chassignet, E. P. (1990). Westward motion of mesoscale eddies. *Journal of Physical Oceanography*, 20(5):758–768.

Danabasoglu, G., Lamarque, J.-F., Bacmeister, J., Bailey, D., DuVivier, A., Edwards, J., Emmons, L., Fasullo, J., Garcia, R., Gettelman, A., et al. (2020). The community earth system model version 2 (cesm2). *Journal of Advances in Modeling Earth Systems*, 12(2):e2019MS001916.

Dickinson, M. and Molinari, J. (2002). Mixed rossby–gravity waves and western pacific tropical cyclogenesis. part i: Synoptic evolution. *Journal of the atmospheric sciences*, 59(14):2183–2196.

DiMarco, S. F., Nowlin, W. D., and Reid, R. (2005). A statistical description of the velocity fields from upper ocean drifters in the gulf of mexico. *Geophysical Monograph-American Geophysical Union*, 161:101.

Donohue, K., Hamilton, P., Leaman, K., Leban, R., Prater, M., Waddell, E., and Watts, R. (2006). Exploratory study of deepwater currents in the gulf of mexico, volume 2: Technical report. Technical report, United States. Minerals Management Service. Gulf of Mexico OCS Region.

Donohue, K., Watts, D., Hamilton, P., Leben, R., Kennelly, M., and Lugo-Fernández, A. (2016a). Gulf of mexico loop current path variability. *Dynamics of Atmospheres and Oceans*, 76:174–194.

Donohue, K. A., Watts, D., Hamilton, P., Leben, R., and Kennelly, M. (2016b). Loop current eddy formation and baroclinic instability. *Dynamics of Atmospheres and Oceans*, 76:195–216.

Duchon, C. E. (1979). Lanczos filtering in one and two dimensions. *Journal of Applied Meteorology and Climatology*, 18(8):1016–1022.

Fu, D., Small, J., Kurian, J., Liu, Y., Kauffman, B., Gopal, A., Ramachandran, S., Shang, Z., Chang, P., Danabasoglu, G., et al. (2021). Introducing the new regional community earth system model, r-cesm. *Bulletin of the American Meteorological Society*, 102(9):E1821–E1843.

Furey, H., Bower, A., Perez-Brunius, P., Hamilton, P., and Leben, R. (2018). Deep eddies in the gulf of mexico observed with floats. *Journal of Physical Oceanography*, 48(11):2703–2719.

Gill, A. E. and Adrian, E. (1982). *Atmosphere-ocean dynamics*, volume 30. Academic press.

Guerrero, L., Sheinbaum, J., Mariño-Tapia, I., González-Rejón, J. J., and Pérez-Brunius, P. (2020). Influence of mesoscale eddies on cross-shelf exchange in the western gulf of mexico. *Continental Shelf Research*, 209:104243.

Hall, C. A. and Leben, R. R. (2016). Observational evidence of seasonality in the timing of loop current eddy separation. *Dynamics of Atmospheres and Oceans*, 76:240–267.

Hamilton, P. (1990). Deep currents in the gulf of mexico. *Journal of Physical Oceanography*, 20(7):1087–1104.

Hamilton, P. (2007). Deep-current variability near the sigsbee escarpment in the gulf of mexico.

Journal of Physical Oceanography, 37(3):708–726.

Hamilton, P. (2009). Topographic rossby waves in the gulf of mexico. *Progress in Oceanography*, 82(1):1–31.

Hamilton, P., Bower, A., Furey, H., Leben, R., and Pérez-Brunius, P. (2019). The loop current: Observations of deep eddies and topographic waves. *Journal of Physical Oceanography*, 49(6):1463–1483.

Hamilton, P., Donohue, K., Hall, C., Leben, R., Quian, H., Sheinbaum, J., and Watts, R. (2015). Observations and dynamics of the loop current.

Hamilton, P., Leben, R., Bower, A., Furey, H., and Pérez-Brunius, P. (2018). Hydrography of the gulf of mexico using autonomous floats. *Journal of Physical Oceanography*, 48(4):773–794.

Hamilton, P. and Lugo-Fernandez, A. (2001). Observations of high speed deep currents in the northern gulf of mexico. *Geophysical Research Letters*, 28(14):2867–2870.

Hamilton, P., Lugo-Fernández, A., and Sheinbaum, J. (2016). A loop current experiment: Field and remote measurements. *Dynamics of Atmospheres and Oceans*, 76:156–173.

Harris, C. R., Millman, K. J., Van Der Walt, S. J., Gommers, R., Virtanen, P., Cournapeau, D., Wieser, E., Taylor, J., Berg, S., Smith, N. J., et al. (2020). Array programming with numpy. *Nature*, 585(7825):357–362.

Harris, F. J. (1978). On the use of windows for harmonic analysis with the discrete fourier transform. *Proceedings of the IEEE*, 66(1):51–83.

Howard, M. K. and DiMarco, S. F. (1998). Latex shelf data report.

Hurrell, J. W., Holland, M. M., Gent, P. R., Ghan, S., Kay, J. E., Kushner, P. J., Lamarque, J.-F., Large, W. G., Lawrence, D., Lindsay, K., et al. (2013). The community earth system model: a framework for collaborative research. *Bulletin of the American Meteorological Society*, 94(9):1339–1360.

Inoue, M., Welsh, S. E., Rouse Jr, L. J., and Weeks, E. (2008). Deepwater currents in the eastern gulf of mexico: Observations at 25.5 n and 87 w.

Jaimes, B., Shay, L. K., and Brewster, J. K. (2016). Observed air-sea interactions in tropical

cyclone isaac over loop current mesoscale eddy features. *Dynamics of Atmospheres and Oceans*, 76:306–324.

Jochens, A. E. and DiMarco, S. F. (2008). Physical oceanographic conditions in the deepwater gulf of mexico in summer 2000–2002. *Deep Sea Research Part II: Topical Studies in Oceanography*, 55(24-26):2541–2554.

Kantha, L. H. and Clayson, C. A. (2000). *Numerical models of oceans and oceanic processes*. Elsevier.

Karspeck, A. R., Danabasoglu, G., Anderson, J., Karol, S., Collins, N., Vertenstein, M., Raeder, K., Hoar, T., Neale, R., Edwards, J., et al. (2018). A global coupled ensemble data assimilation system using the community earth system model and the data assimilation research testbed. *Quarterly Journal of the Royal Meteorological Society*, 144(717):2404–2430.

Kolodziejczyk, N., Ochoa, J., Candela, J., and Sheinbaum, J. (2011). Deep currents in the bay of campeche. *Journal of physical oceanography*, 41(10):1902–1920.

Lamb, H. (1932). Hydrodynamics, cambridge univ. *Press,*, pages 134–139.

Leben, R. R. (2005). Altimeter-derived loop current metrics. *Geophysical Monograph-American Geophysical Union*, 161:181.

Liu, Y., Weisberg, R. H., and Mooers, C. N. (2006). Performance evaluation of the self-organizing map for feature extraction. *Journal of Geophysical Research: Oceans*, 111(C5).

Liu, Y., Weisberg, R. H., Vignudelli, S., and Mitchum, G. T. (2016). Patterns of the loop current system and regions of sea surface height variability in the eastern gulf of mexico revealed by the self-organizing maps. *Journal of Geophysical Research: Oceans*, 121(4):2347–2366.

Lugo-Fernández, A. (2016). The loop current dynamics experiment (2009-2011) in the gulf of mexico. *Dynamics of Atmospheres and Oceans*, 76:155–155.

Lugo-Fernández, A., Leben, R. R., and Hall, C. A. (2016). Kinematic metrics of the loop current in the gulf of mexico from satellite altimetry. *Dynamics of Atmospheres and Oceans*, 76:268–282.

Mauli, G. A. (1977). The annual cycle of the gulf loop current: Part 1: Observations during a one-year time series. *Collected Reprints*, 1(1):398.

Meunier, T., Pallás-Sanz, E., Tenreiro, M., Portela, E., Ochoa, J., Ruiz-Angulo, A., and Cusí, S. (2018). The vertical structure of a loop current eddy. *Journal of Geophysical Research: Oceans*, 123(9):6070–6090.

Meunier, T., Sheinbaum, J., Pallàs-Sanz, E., Tenreiro, M., Ochoa, J., Ruiz-Angulo, A., Carton, X., and de Marez, C. (2020). Heat content anomaly and decay of warm-core rings: The case of the gulf of mexico. *Geophysical Research Letters*, 47(3):e2019GL085600.

Morey, S. L., Gopalakrishnan, G., Sanz, E. P., Azevedo Correia De Souza, J. M., Donohue, K., Pérez-Brunius, P., Dukhovskoy, D., Chassignet, E., Cornuelle, B., Bower, A., et al. (2020). Assessment of numerical simulations of deep circulation and variability in the gulf of mexico using recent observations. *Journal of Physical Oceanography*, 50(4):1045–1064.

National Academies of Sciences, E., Medicine, et al. (2018). *Understanding and predicting the gulf of mexico loop current: Critical gaps and recommendations*. National Academies Press.

Nickerson, A. K., Weisberg, R. H., and Liu, Y. (2022). On the evolution of the gulf of mexico loop current through its penetrative, ring shedding and retracted states. *Advances in Space Research*, 69(11):4058–4077.

Nof, D. (2005). The momentum imbalance paradox revisited. *Journal of physical oceanography*, 35(10):1928–1939.

Nowlin, W. D., Jochens, A. E., DiMarco, S. F., Reid, R. O., and Howard, M. K. (2005). Low-frequency circulation over the texas-louisiana continental shelf. *Geophysical Monograph-American Geophysical Union*, 161:219.

Oey, L. (2008). Loop current and deep eddies. *Journal of physical oceanography*, 38(7):1426–1449.

Oey, L. and Lee, H. (2002). Deep eddy energy and topographic rossby waves in the gulf of mexico. *Journal of physical Oceanography*, 32(12):3499–3527.

Pallàs-Sanz, E., Candela, J., Sheinbaum, J., and Ochoa, J. (2016). Mooring observations of the near-inertial wave wake of hurricane ida (2009). *Dynamics of Atmospheres and Oceans*, 76:325–344.

Pedlosky, J. et al. (1987). *Geophysical fluid dynamics*, volume 710. Springer.

Pérez-Brunius, P., Furey, H., Bower, A., Hamilton, P., Candela, J., García-Carrillo, P., and Leben, R. (2018). Dominant circulation patterns of the deep gulf of mexico. *Journal of Physical Oceanography*, 48(3):511–529.

Pérez-Brunius, P., García-Carrillo, P., Dubranna, J., Sheinbaum, J., and Candela, J. (2013). Direct observations of the upper layer circulation in the southern gulf of mexico. *Deep Sea Research Part II: Topical Studies in Oceanography*, 85:182–194.

Portela, E., Tenreiro, M., Pallàs-Sanz, E., Meunier, T., Ruiz-Angulo, A., Sosa-Gutiérrez, R., and Cusí, S. (2018). Hydrography of the central and western gulf of mexico. *Journal of Geophysical Research: Oceans*, 123(8):5134–5149.

Pujiana, K. and McPhaden, M. J. (2021). Biweekly mixed rossby-gravity waves in the equatorial indian ocean. *Journal of Geophysical Research: Oceans*, 126(5):e2020JC016840.

Rosburg, K. C., Donohue, K. A., and Chassignet, E. P. (2016). Three-dimensional model-observation comparison in the loop current region. *Dynamics of Atmospheres and Oceans*, 76:283–305.

Rudnick, D. L., Gopalakrishnan, G., and Cornuelle, B. D. (2015). Cyclonic eddies in the gulf of mexico: Observations by underwater gliders and simulations by numerical model. *Journal of Physical Oceanography*, 45(1):313–326.

Schaudt, K., Forristall, G., Kantha, L., Leben, R., Choi, J., Black, P., Uhlhorn, E., Guinasso, N., Walpert, J., Kelly, F., et al. (2001). A look at currents in the gulf of mexico in 1999-2000. In *Offshore Technology Conference*. OnePetro.

Schmitz Jr, W. J. and McCartney, M. S. (1993). On the north atlantic circulation. *Reviews of Geophysics*, 31(1):29–49.

Shchepetkin, A. F. and McWilliams, J. C. (2005). The regional oceanic modeling system (roms): a split-explicit, free-surface, topography-following-coordinate oceanic model. *Ocean modelling*, 9(4):347–404.

Sheinbaum, J., Athié, G., Candela, J., Ochoa, J., and Romero-Arteaga, A. (2016). Structure and

variability of the yucatan and loop currents along the slope and shelf break of the yucatan channel and campeche bank. *Dynamics of Atmospheres and Oceans*, 76:217–239.

Skamarock, W. C. (2008). A description of theadvanced research wrf version 3. pages 1–96.

Small, R. J., Bacmeister, J., Bailey, D., Baker, A., Bishop, S., Bryan, F., Caron, J., Dennis, J., Gent, P., Hsu, H.-m., et al. (2014). A new synoptic scale resolving global climate simulation using the community earth system model. *Journal of Advances in Modeling Earth Systems*, 6(4):1065–1094.

Sosa-Gutiérrez, R., Pallàs-Sanz, E., Jouanno, J., Chaigneau, A., Candela, J., and Tenreiro, M. (2020). Erosion of the subsurface salinity maximum of the loop current eddies from glider observations and a numerical model. *Journal of Geophysical Research: Oceans*, 125(7):e2019JC015397.

Spencer, L. J., DiMarco, S. F., Wang, Z., Kuehl, J. J., and Brooks, D. A. (2016). Asymmetric oceanic response to a hurricane: Deep water observations during hurricane isaac. *Journal of Geophysical Research: Oceans*, 121(10):7619–7649.

Sturges, W. and Leben, R. (2000). Frequency of ring separations from the loop current in the gulf of mexico: A revised estimate. *Journal of Physical Oceanography*, 30(7):1814–1819.

Sturges, W. and Lugo-Fernández, A. (2005). Circulation in the gulf of mexico: observations and models. *Washington DC American Geophysical Union Geophysical Monograph Series*, 161.

Sutyrin, G., Rowe, G., Rothstein, L., and Ginis, I. (2003). Baroclinic eddy interactions with continental slopes and shelves. *Journal of physical Oceanography*, 33(1):283–291.

Tenreiro, M., Candela, J., Sanz, E. P., Sheinbaum, J., and Ochoa, J. (2018). Near-surface and deep circulation coupling in the western gulf of mexico. *Journal of Physical Oceanography*, 48(1):145–161.

Thomson, R. E. and Emery, W. J. (2014). *Data analysis methods in physical oceanography*. Newnes.

Vettigli, G. (2018). Minisom: minimalistic and numpy-based implementation of the self organizing map.

Vidal, V. M., Vidal, F. V., and Pérez-Molero, J. M. (1992). Collision of a loop current anticyclonic ring against the continental shelf slope of the western gulf of mexico. *Journal of Geophysical Research: Oceans*, 97(C2):2155–2172.

Volkov, D. L., Domingues, R., Meinen, C. S., Garcia, R., Baringer, M., Goni, G., and Smith, R. H. (2020). Inferring florida current volume transport from satellite altimetry. *Journal of Geophysical Research: Oceans*, 125(12):e2020JC016763.

Vukovich, F. M. and Maul, G. A. (1985). Cyclonic eddies in the eastern gulf of mexico. *Journal of physical Oceanography*, 15(1):105–117.

Walker, N., Leben, R., Anderson, S., Haag, A., and Pilley, C. (2009). High frequency satellite surveillance of gulf of mexico loop current frontal eddy cyclones. In *OCEANS 2009*, pages 1–9. IEEE.

Welsh, S. E. and Inoue, M. (2000). Loop current rings and the deep circulation in the gulf of mexico. *Journal of Geophysical Research: Oceans*, 105(C7):16951–16959.

APPENDIX A

MOORING DETAILS OF LOOP CURRENT DYNAMICS EXPERIMENTS 2009-2011

Table A.1: The detailed information of all moorings in Figure 2. The lower ADCP is downward when there are two ADCPs at a similar depth. All the other ADCPs are upward. The CICESE moorings also have temperature recorders at those depths. Notes: ADCP_75/300 is 75/300 kHz Acoustic Doppler Current Profiler, NCM is Nortek Aquadopp Current Meter, NR is Not Recovered, RCM-# is Recording (Doppler) Current Meter, TEMP is Temperature Recorders, T/S/P is Conductivity and Temperature Recorders, SCM is SeaGuard (Doppler type) Current Meter, S4 is InterOcean S4 Electromagnetic Current Meter. Adapted from Hamilton et al. (2015).

Mooring	**Location**	**Water Depth (m)**	**Instrument Depth (m)**	**Instrument Type**	**Deployment Period (UTC)**
A1	25°57.666'N 88°03.159'W	3036	75 150 250 350 450 525 600 750 900 1100 1300 1500 2000 2930	TEMP T/S/P TEMP TEMP ADCP_75 TEMP S4 T/S/P RCM-7 TEMP RCM-8 TEMP RCM-11 RCM-11	05/05/2009 to 07/19/2010 07/20/2010 to 11/13/2011

Mooring	Location	Water Depth (m)	Instrument Depth (m)	Instrument Type	Deployment Period (UTC)
A2	25°49.012'N 87°33.126'W	3208	75 150 250 350 450 525 600 750 900 1100 1300 1500 2000 3108	TEMP T/S/P TEMP TEMP ADCP_75 TEMP S4 T/S/P RCM-7 TEMP RCM-8 TEMP RCM-11 RCM-11	05/04/2009 to 07/17/2010 07/18/2010 to 11/13/2011
A3	25°40.531'N 87°02.891'W	3302	75 150 250 350 450 525 600 750 900 1100 1300 1500 2000 3202	TEMP T/S/P TEMP TEMP ADCP_75 TEMP S4 T/S/P RCM-7 TEMP RCM-8 TEMP RCM-11 RCM-11	04/30/2009 to 07/10/2010 07/11/2010 to 11/08/2011
A4	25°29.164'N 86°33.565'W	3270	75 150 250 350 450 525 600 750 900 1100 1300 1500 2000 3170	TEMP T/S/P TEMP TEMP ADCP_75 TEMP S4 T/S/P RCM-7 TEMP RCM-8 TEMP RCM-11 RCM-11	04/30/2009 to 07/08/2010 07/09/2010 to 11/03/2011

Mooring	Location	Water Depth (m)	Instrument Depth (m)	Instrument Type	Deployment Period (UTC)
B1	26°15.245'N 87°18.998'W	3049	75 90 [2] 150 250 350 450 525 599 [2] 600 750 900 1100 1300 1500 1990 2949	TEMP ADCP_300 T/S/P TEMP TEMP ADCP_75 TEMP RCM-8 S4 T/S/P RCM-7/8 TEMP RCM-7/8 TEMP RCM-11 RCM-11	05/14/2009 to 11/09/2010 11/10/2010 to 11/01/2011
B2	26°06.701'N 86°50.359'W	3138	75 90 [2] 91 [2] 150 250 350 450 525 600 750 900 1100 1300 1500 2000 3038	TEMP S4 RCM-11 T/S/P TEMP TEMP ADCP_75 TEMP S4 T/S/P RCM-7 TEMP RCM-8 TEMP RCM-11 RCM-11	05/11/2009 to 11/11/2010 11/12/2010 to 11/08/2011

Mooring	Location	Water Depth (m)	Instrument Depth (m)	Instrument Type	Deployment Period (UTC)
B3	25°55.617'N 86°21.301'W	3160	75 150 250 350 450 525 600 750 900 1100 1300 1500 2000 3060	TEMP T/S/P TEMP TEMP ADCP_75 TEMP S4 T/S/P RCM-7 TEMP RCM-8/7 TEMP RCM-11 RCM-11	05/10/2009 to 07/02/2010 07/03/2010 to 11/09/2011
C1	26°22.536'N 86°08.597'W	3190	75 150 250 350 450 525 600 750 900 1100 1300 1500 1995 3090	TEMP T/S/P TEMP TEMP ADCP_75 TEMP S4 T/S/P RCM-7 TEMP RCM-7 TEMP RCM-11 RCM-11	04/20/2009 to 07/12/2010 07/15/2010 to 10/28/2011
C2	26°10.737'N 85°38.921'W	3257	75 150 250 350 450 525 600 750 900 1100 1300 1500 1990 3157	TEMP T/S/P TEMP TEMP ADCP_75 TEMP S4 T/S/P RCM-7 TEMP RCM-7/8 TEMP RCM-11 RCM-11	04/22/2009 to 07/04/2010 07/07/2010 to 10/27/2011

Mooring	Location	Water Depth (m)	Instrument Depth (m)	Instrument Type	Deployment Period (UTC)
D1	26°24.986'N 87°51.007'W	2827	2727	RCM-8	05/15/2009 to 07/19/2010 07/20/2010 to NR
D2	26°41.751'N 87°07.587'W	2885	2785	RCM-8	05/06/2009 to 07/16/2010 07/16/2010 to 11/14/2011
D3	26°32.949'N 86°37.301'W	3098	2998	RCM-8	05/09/2009 to 07/12/2010 07/12/2010 to NR
D4	25°17.993'N 86°04.783'W	3259	3159	RCM-8	04/27/2009 to 07/01/2010 07/02/2010 to 01/14/2012
D5	25°44.336'N 85°51.744'W	3234	3134	RCM-8	04/27/2009 to 06/30/2010 07/01/2010 to 11/02/2011
D7	25°33.042'N 85°22.986'W	3311	3211	RCM-8	04/21/2009 to 07/26/2010 07/26/2010 to 11/02/2011

Mooring	Location	Water Depth (m)	Instrument Depth (m)	Instrument Type	Deployment Period (UTC)
D8	25°59.946'N 85°09.216'W	3309	3209	RCM-8	04/21/2009 to 07/26/2010 07/26/2010 to 10/27/2011
P51	26°42.845'N 87°59.480'W	2733	PIES	P/τ	04/23/2009 to 11/01/2011
P52	26°16.459'N 88°11.953'W	2823	PIES	P/τ	04/26/2009 to 11/05/2011
P53	25°50.150'N 88°24.455'W	3114	PIES	P/τ	05/01/2009 to 11/05/2011
P54	27°00.635'N 87°16.318'W	2882	PIES	P/τ	04/19/2009 to 10/26/2011
P55	26°34.062'N 87°28.821'W	2833	PIES	P/τ	04/23/2009 to 11/01/2011
P56	26°07.733'N 87°41.468'W	3029	PIES	P/τ	04/26/2009 to 11/01/2011
P57	25°41.472'N 87°53.975'W	3209	PIES	P/τ	05/01/2009 to 11/05/2011
P58	26°51.826'N 86°45.471'W	3065	PIES	P/τ	04/19/2009 to 10/26/2011
P59	26°25.386'N 86°58.320'W	3023	PIES	P/τ	04/23/2009 to 10/29/2011
P60	25°59.034'N 87°11.058'W	3184	PIES	P/τ	04/26/2009 to 11/02/2011
P61	25°32.876'N 87°23.817'W	3332	PIES	P/τ	05/01/2009 to 11/04/2011

Mooring	Location	Water Depth (m)	Instrument Depth (m)	Instrument Type	Deployment Period (UTC)
P62	26°43.025'N 86°14.809'W	3169	PIES	P/τ	04/19/2009 to 10/27/2011
P63	26°16.683'N 86°27.902'W	3108	PIES	P/τ	04/23/2009 to 10/29/2011
P64	25°50.267'N 86°40.210'W	3247	PIES	P/τ	04/26/2009 to 11/02/2011
P65	25°24.073'N 86°53.477'W	3326	PIES	P/τ	04/30/2009 to 11/04/2011
P66	26°31.902'N 85°45.658'W	3226	PIES	P/τ	04/19/2009 to 10/27/2011
P67	26°05.497'N 85°58.772'W	3240	PIES	P/τ	04/21/2009 to 10/28/2011
P68	25°39.161'N 86°11.594'W	3213	PIES	P/τ	04/27/2009 to 11/02/2011
P69	25°12.893'N 86°24.497'W	3293	PIES	P/τ	04/30/2009 to 11/04/2011
P70	26°18.275'N 85°17.950'W	3298	PIES	P/τ	04/20/2009 to 10/27/2011
P71	25°51.902'N 85°31.001'W	3278	PIES	P/τ	04/21/2009 to 10/28/2011
P72	25°25.562'N 85°43.943'W	3286	PIES	P/τ	04/27/2009 to 11/03/2011
P73	24°59.229'N 85°56.835'W	3325	PIES	P/τ	04/29/2009 to 11/04/2011
P74	25°38.033'N 85°03.289'W	3336	PIES	P/τ	04/21/2009 to 10/28/2011
P75	25°11.899'N 85°16.260'W	3341	PIES	P/τ	04/28/2009 to 11/03/2011

Mooring	Location	Water Depth (m)	Instrument Depth (m)	Instrument Type	Deployment Period (UTC)
N1	23°45.70'N 87°55.11'W	130	118 124	ADCP_300 RCM-11	05/31/2009 to 05/07/2011
N2	24°11.80'N 87°34.01'W	500	490	ADCP_75	05/31/2009 to 05/07/2011
N3	24°23.90'N 87°24.68'W	1205	508 1020 1195	ADCP_75 NCM NCM/SCM	05/31/2009 to 05/07/2011
N4	24°57.47'N 87°04.95'W	3352	535 1038 1250 1490 1780 2295 2830 3334	ADCP_75 ADCP_75 NCM NCM/RCM-11 NCM NCM/SCM NCM/RCM-11 NCM	06/01/2009 to 05/06/2011
E1	22°23.01'N 87°00.43'W	127	118	ADCP_300	06/02/2009 to 05/09/2011
E2	22°49.81'N 86°38.36'W	501	490	ADCP_75	06/02/2009 to 05/09/2011
E3	23°03.37'N 86°25.98'W	998	487 589 794 989	ADCP_75 NCM/RCM-11 NCM/RCM-11 NCM/RCM-11	06/02/2009 to 05/08/2011
E4	23°14.48'N 86°17.58'W	1994	472 987 1252 1480 1983	ADCP_75 ADCP_75 NCM/RCM-11 NCM/RCM-11 NCM/RCM-11	06/02/2009 to 05/08/2011

Mooring	Location	Water Depth (m)	Instrument Depth (m)	Instrument Type	Deployment Period (UTC)
E5	23°36.17'N 86°01.37'W	3354	548 1051 1263 1514 1806 2315 2853 3342	ADCP_75 ADCP_75 NCM/RCM-11 NCM/RCM-11 NCM/RCM-11 NCM NCM/RCM-11 NCM	06/01/2009 to 05/08/2011
EN	23°04.09'N 86°47.01'W	500	496	ADCP_75	06/02/2009 to 04/26/2010
Y1	21°32.42'N 86°42.00'W	23	21	NCM	04/24/2010 to 04/18/2011
Y2	21°32.44'N 86°29.74'W	68	58	ADCP_300	06/05/2009 to 05/11/2011
Y3	21°33.46'N 86°27.00'W	124	112	ADCP_300	06/04/2009 to 05/11/2011
Y4	21°33.96'N 86°21.30'W	526	526	ADCP_75	06/04/2009 to 04/18/2010
Y5	21°35.55'N 86°13.64'W	1206	526 594 715 972 1074 1189	ADCP_75 RCM-11/NCM RCM-11/NCM RCM-11/NCM RCM-11/NCM RCM-11/NCM	06/12/2009 to 05/11/2011

Mooring	Location	Water Depth (m)	Instrument Depth (m)	Instrument Type	Deployment Period (UTC)
Y6	21°38.81'N 85°59.16'W	1880	488 489 740 741 848 1050 1257 1870	ADCP_75 ADCP_300 ADCP_300 RCM-11/SCM RCM-11/NCM RCM-11/SCM RCM-11/NCM RCM-11/SCM	06/04/2009 to 05/11/2011
Y7	21°38.37'N 85°42.97'W	2030	504 505 704 961 1155 1520 1903 2018	ADCP_75 ADCP_300 RCM-11/SCM RCM-11/NCM RCM-11 RCM-11/NCM RCM-11/SCM RCM-11/NCM	06/03/2009 to 05/10/2011
YN	21°41.65'N 86°20.50'W	495	485	ADCP_75	06/03/2009 to 08/29/2009